A MEASUREMENT OF THE INCLUSIVE DIFFERENTIAL DRELL-YAN CROSS SECTION WITH DIMUONS AT $\sqrt{S} = 1.8$ TEV

BY

VICTOR EMANUEL SCARPINE

B.E., Youngstown State University, 1979
M.S., University of Illinois, 1986

THESIS

Submitted in the partial fulfillment of the requirements
for the degree of the Doctor of Philosophy in Physics
in the Graduate College of the
University of Illinois at Urbana-Champaign, 1992

Urbana, Illinois

A MEASUREMENT OF THE INCLUSIVE DIFFERENTIAL DRELL-YAN CROSS SECTION WITH DIMUONS AT $\sqrt{S} = 1.8$ TEV

Victor Emanuel Scarpine, Ph.D.
Department of Physics
University of Illinois at Urbana-Champaign, 1992
Professor L. E. Holloway, advisor

The inclusive differential Drell-Yan cross section is measured from the analysis of $\bar{p}p \rightarrow \gamma \rightarrow \mu^+\mu^- X$ events at a center-of-mass energy of $\sqrt{s} = 1.8$ TeV at the Fermilab Tevatron collider. The dimuon events are accepted in the central pseudorapidity region of $-0.6 < \eta < 0.6$ of the CDF detector. The differential cross section $d\sigma/dMdY|_{Y=0}$ is measured for dimuon invariant masses between 11 GeV/c^2 and 40 GeV/c^2 and is compared to next-to-leading order theoretical predictions. The $\sigma(Z^\circ \rightarrow \mu^+\mu^-)$ cross section is also measured.

Acknowledgments

I first want to thank my parents, my mother who is still with me and my father who has passed on. They sacrificed everything so their children could have a good life. I also want to thank my sisters, Lucille and Clara, who were always interested in my research and once in awhile would slip me a little spending cash. Thanks also to Carl, Mark, Steve, and Beth Ann for there support over the years. Thanks to my Aunt Rita and Uncle Rocky, who always used to listen to me dream when I was younger, and thanks to all the rest of my relatives, wherever they may be.

I would like to thank my advisor, Lee Holloway, who kept me going through all the muck and grime and finally convinced me to quit trying to squeeze blood from a stone and write this up. I would like to thank the rest of the University of Illinois CDF group, both past and present. Steve, Tony, Alain, Tom W., Dave S., Hovhannes, Bob Sard, Vitias and all the rest. Thanks goes out to all of the High Energy department secretaries over the years. Thanks to Tom Shaw for keeping the cash flow straight. Thanks to Randy Keup and Andrew Martin for being great jamming partners to remind me that there is more to life than physics. Special thanks to Phil Schlabach and Peter Hurst. Phil, for getting me to run again, and Peter, for listening to me ramble on incoherently about things over dinner and still willing to go to dinner again.

I would like to thank all the people I met along the way at the University of Illinois. Thanks to Tom and Fred and life at the friendly house. It was my introduction into hell. Also, thanks to John and Gary for life at the big house. An experience not soon to be forgotten. A special thanks to Marianne. She showed me that one can kill as many brain cells as possible and still hit a dart board. Someday I'll beat her! Thanks also to Elaine, for taking me out to Krannert once in awhile to see how other people live; Sharon, for showing me how live life to the fullest; and Dan, for his great home brew. How can I thank Pat, Marty, Johnny, and Anita? A finer group of friends one could

I can not forget all of my fellow CDF friends who made life in the suburbs of Chicago more than just work - Brian, Les, Paul T., Paul D., Steve & Dee, Leigh, Karen, Eric, Jodi, Chris W., Tiny, the Chucker, JJ, Fumi, and Theresa. Thanks for everyone who helped on the analysis and any other work along the way - Milciades, Ken B., Fritz, Tim R., Henry, Carla, Richard, A warm jamming thanks to the rest of the Nerve Ends Rubbed Raw - Larry, John H., John S., Alessandra, Marco, Mike & Merry. If we can't do physics, we can always play.

Last but not least, I would like to thank Claudia for all of her support and help over the years. She is definitely one in a million and the truest friend I have ever known.

This thesis was supported in part by the U.S. Department of Energy under contract DE-AC02-76ERO1195.

CDF Collaboration for the 1988-1989 Run

F. Abe,[8] D. Amidei,[4] G. Apollinari,[11] M. Atac,[4] P. Auchincloss,[14] A. R. Baden,[6] A. Bamberger,[4,a] A. Barbaro-Galtieri,[9] V. E. Barnes,[12] F. Bedeschi,[11] S. Behrends,[12] S. Belforte,[11] G. Bellettini,[11] J. Bellinger,[18] J. Bensinger,[2] A. Beretvas,[4] J. P. Berge,[4] S. Bertolucci,[5] S. Bhadra,[7] M. Binkley,[4] R. Blair,[1] C. Blocker,[2] A. W. Booth,[4] G. Brandenburg,[6] D. Brown,[6] E. Buckley,[14] A. Byon,[12] K. L. Byrum,[18] C. Campagnari,[3] M. Campbell,[3] R. Carey,[6] W. Carithers,[9] D. Carlsmith,[18] J. T. Carroll,[4] R. Cashmore,[4,a] F. Cervelli,[11] K. Chadwick,[4] G. Chiarelli,[5] W. Chinowsky,[9] S. Cihangir,[4] A. G. Clark,[4] D. Connor,[10] M. Contreras,[2] J. Cooper,[4] M. Cordelli,[5] D. Crane,[4] M. Curatolo,[5] C. Day,[4] S. Dell'Agnello,[11] M. Dell'Orso,[11] L. DeMortier,[2] P. F. Derwent,[3] T. Devlin,[14] D. DiBitonto,[15] R. B. Drucker,[9] J. E. Elias,[4] R. Ely,[9] S. Errede,[7] B. Esposito,[5] B. Flaugher,[14] G. W. Foster,[4] M. Franklin,[6] J. Freeman,[4] H. Frisch,[3] Y. Fukui,[8] Y. Funayama,[16] A. F. Garfinkel,[12] A. Gauthier,[7] S. Geer,[6] P. Giannetti,[11] N. Giokaris,[13] P. Giromini,[5] L. Gladney,[10] M. Gold,[9] K. Goulianos,[13] H. Grassmann,[11] C. Grosso-Pilcher,[3] C. Haber,[9] S. R. Hahn,[4] R. Handler,[18] K. Hara,[16] R. M. Harris,[9] J. Hauser,[3] T. Hessing,[15] R. Hollebeek,[10] L. Holloway,[7] P. Hu,[14] B. Hubbard,[9] B. T. Huffman,[12] R. Hughes,[10] P. Hurst,[7] J. Huth,[4] M. Incagli,[11] T. Ino,[16] H. Iso,[16] H. Jensen,[4] C. P. Jessop,[6] R. P. Johnson,[4] U. Joshi,[4] R. W. Kadel,[4] T. Kamon,[15] S. Kanda,[16] D. A. Kardelis,[7] I. Karliner,[7] E. Kearns,[6] R. Kephart,[4] P. Kesten,[2] R. M. Keup,[7] H. Keutelian,[7] S. Kim,[16] L. Kirsch,[2] K. Kondo,[16] S. E. Kuhlmann,[1] E. Kuns,[14] A. T. Laasanen,[12] J. I. Lamoureux,[18] W. Li,[1] T. M. Liss,[7] N. Lockyer,[10] C. B. Luchini,[7] P. Maas,[4] M. Mangano,[11] J. P. Marriner,[4] R. Markeloff,[18] L. A. Markosky,[18] R. Mattingly,[2] P. McIntyre,[15] A. Menzione,[11] T. Meyer,[15] S. Mikamo,[8] M. Miller,[3] T. Mimashi,[16] S. Miscetti,[5] M. Mishina,[8] S. Miyashita,[16] Y. Morita,[16] S. Moulding,[2] A. Mukherjee,[4] Y. Muraki,[16] L. Nakae,[2] I. Nakano,[16] C. Nelson,[4] C. Newman-Holmes,[4] J. S. T. Ng,[6] M. Ninomiya,[16] L. Nodulman,[1] S. Ogawa,[16] R. Paoletti,[11] A. Para,[4] E. Pare,[6] J. Patrick,[4] T. J. Phillips,[6] R. Plunkett,[4] L. Pondrom,[18] J. Proudfoot,[1] G. Punzi,[11] D. Quarrie,[4] K. Ragan,[10] G. Redlinger,[3] J. Rhoades,[18] F. Rimondi,[4,a] L. Ristori,[11] T. Rohaly,[10] A. Roodman,[3] A. Sansoni,[5] R. D. Sard,[7] A. Savoy-Navarro,[4,a] V. Scarpine,[7] P. Schlabach,[7] E. E. Schmidt,[4] M. H. Schub,[12] R. Schwitters,[6] A. Scribano,[11] S. Segler,[4] Y. Seiya,[16] M. Sekiguchi,[16] P. Sestini,[11] M. Shapiro,[6] M. Sheaff,[18] M. Shochet,[3] J. Siegrist,[9] P. Sinervo,[10] J. Skarha,[18] K. Sliwa,[17] D. A. Smith,[11] F. D. Snider,[3] R. St. Denis,[6] A. Stefanini,[11] R. L. Swartz, Jr.,[7] M. Takano,[16] K. Takikawa,[16] S. Tarem,[2] D. Theriot,[4] M. Timko,[15] P. Tipton,[9] S. Tkaczyk,[4] A. Tollestrup,[4] G. Tonelli,[11] J. Tonnison,[12] W. Trischuk,[6] Y. Tsay,[3] F. Ukegawa,[16] D. Underwood,[1] R. Vidal,[4] R. G. Wagner,[1] R. L. Wagner,[4] J. Walsh,[10] T. Watts,[14] R. Webb,[15] C. Wendt,[18] W. C. Wester, III,[9] T. Westhusing,[11] S. White,[13] A. Wicklund,[1] H. H. Williams,[10] B. Winer,[9] A. Yagil,[4] A. Yamashita,[16] K. Yasuoka,[16] G. P. Yeh,[4] J. Yoh,[4] M. Yokoyama,[16] J. C. Yun,[4] and F. Zetti[11]

[1] *Argonne National Laboratory, Argonne, Illinois 60439*
[2] *Brandeis University, Waltham, Massachusetts 02254*
[3] *University of Chicago, Chicago, Illinois 60637*
[4] *Fermi National Accelerator Laboratory, Batavia, Illinois 60510*
[5] *Laboratori Nazionali di Frascati, Istituto Nazionale di Fisica Nucleare, Frascati, Italy*
[6] *Harvard University, Cambridge, Massachusetts 02138*
[7] *University of Illinois, Urbana, Illinois 61801*
[8] *National Laboratory for High Energy Physics (KEK), Tsukuba-gun, Ibaraki-ken 305, Japan*
[9] *Lawrence Berkeley Laboratory, Berkeley, California 94720*
[10] *University of Pennsylvania, Philadelphia, Pennsylvania 19104*
[11] *Istituto Nazionale di Fisica Nucleare, University and Scuola Normale Superiore of Pisa, I-56100 Pisa, Italy*
[12] *Purdue University, West Lafayette, Indiana 47907*
[13] *Rockefeller University, New York, New York 10021*
[14] *Rutgers University, Piscataway, New Jersey 08854*
[15] *Texas A&B University, College Station, Texas 77843*
[16] *University of Tsukuba, Ibaraki 305, Japan*
[17] *Tufts University, Medford, Massachusetts 02155*
[18] *University of Wisconsin, Madison, Wisconsin 53706*

Contents

1 Introduction and Theory of Drell-Yan Physics 1

1.1 Fundamental Particles and the Standard Model 1

1.2 The Parton Model 4

1.2.1 Parton Distribution Functions 5

1.3 Drell-Yan Physics 6

1.3.1 Higher-Order QCD Corrections to the Drell-Yan Cross section and the Anomalous K-factor 11

1.4 Other Experimental Measurements 15

1.5 The Goal of this Thesis 18

2 The Fermilab Tevatron and CDF Detector 19

2.1 The Tevatron Collider 19

2.2 The CDF Detector 21

2.2.1 The CDF Calorimetry System 21

2.2.2 The CDF Tracking System 23

2.2.3 The CDF Muon Detection System 27

2.3 Data Acquisition Path 29

2.4 CDF Trigger System and the Central Dimuon Trigger 31

2.4.1 Level 1 Central Muon Trigger 32

2.4.2 Level 2 Central Dimuon Trigger 33

3 Dimuon Data Selection 36
3.1 Offline Data Reconstruction 36
3.2 Extraction of an Inclusive Isolated Dimuon Data Set 38
3.2.1 Sources of Fake Muons 40
3.2.2 Drell-Yan Dimuon Selection Cuts 41
3.2.3 Description of Selection Cuts 42
3.2.4 Efficiency of Selection Cuts 48

4 Drell-Yan Monte Carlo Data in the CDF Environment 52
4.1 Generaton and Simulation of Monte Carlo Data 52
4.1.1 Vertex Smearing and CDF Detector Simulation 53
4.1.2 The Level 2 DIMUON_CENTRAL_3 Trigger Simulation 54
4.1.3 Central Muon Detector Fiducial Regions 54
4.2 Comparison of ISAJET Monte Carlo to Real Drell-Yan 56
4.3 Drell-Yan Acceptance and Trigger Efficiency Versus Mass 56
4.3.1 Systematic Errors to the Acceptance and Trigger Efficiency 59

5 Backgrounds in the Drell-Yan Data Sample 61
5.1 Cosmic Ray Background 61
5.1.1 Impact Parameter Cut Efficiency 62
5.1.2 Back-to-Back $\Delta\phi_{3D}$ Cut Description 63
5.1.3 Remaining Cosmic Ray Background 65
5.2 τ Background 69
5.3 QCD Background 72
5.3.1 Symmetric QCD Background 72
5.3.2 Non-Symmetric QCD Background 74
5.4 Total Remaining Background 76

6 Calculation of Drell-Yan Differential Cross Sections and Conclusion . 78
6.1 Differential Cross Section Calculation 78

6.2 Drell-Yan Analysis for Future Collider Runs 82
6.3 Conclusion 83

A J/ψ's and Υ's: Dimuons in the CDF Environment 86

B Determination of the Isolation Cut 98

Biliography 103

Vita 107

List of Tables

1.1 Table of quarks and leptons. 3

1.2 Table of fundamental forces and their carriers. 3

1.3 Partial list of Parton Distribution Functions with references to experimental data used. Parentheses indicate the corresponding data are only partially used. 6

1.4 Partial list of measured K-factors. 16

2.1 Summary of central calorimeter properties. 24

2.2 Summary of endplug and forward gas calorimeter properties. 25

2.3 Summary of central tracking chamber properties. 26

3.1 Table of selection cut efficiencies. 48

4.1 Table of Acceptance$\otimes$Trigger efficiency versus Mass for $d^2\sigma/dMdY|_{Y=0}$. 59

5.1 Fraction of $B-\bar{B}$ lepton pair decays passing all selection cuts. 75

5.2 Remaining background from cosmic rays and symmetric QCD heavy quark decays for each mass bin of interest. 77

6.1 Table of number of opposite-signed dimuon minus same-signed dimuons for each mass bin. 79

6.2 Table of number of events, acceptance*trigger efficiency, ΔM, and Drell-Yan weighted average mass used to calculate the differential cross section. 80

6.3 Differential cross sections $d^2\sigma/dMdY|_{Y=0}$ and $M^3d^2\sigma/dMdY|_{Y=0}$ from dimuon events. 82

B.1 Number of Z° dimuon candidates and efficiency (ϵ) of isolation cut for various types of isolation cuts and different cut values. All selection cuts in have been made and there are 22 possible dimuon Z° candidates. . . . 100

B.2 Number of opposite-signed (OS) and same-signed (SS) dimuons present in dimuon sample for various types of isolation cuts and different cut values. All selection cuts in chapter 3 have been made. 101

B.3 Fraction (f) of $B - \bar{B}$ events passing dimuon selection cuts. 102

List of Figures

1.1 Up valence quark density for several PDF's as a function of x. 7

1.2 Gluon density for several PDF's as a function of x. 8

1.3 Lowest-order Drell-Yan Feynman diagram. 9

1.4 Experimental measurement of $M^3 d^2\sigma/dMdY|_{Y=0}$. This shows the scaling effect predicted by Drell-Yan theory. 12

1.5 Comparision of the lowest-order predicted Drell-Yan cross section to that measured by experiment E288. 13

1.6 Higher-order Drell-Yan Feynman diagrams. 14

1.7 Measured K-factor versus mass for experiment NA3. 17

2.1 Fermilab National Accelerator (FNAL). 20

2.2 Distribution of Z positions for CDF event vertices with superimposed gaussian of a mean of 0.0 cm and a σ of 30.0 cm. 21

2.3 CDF detector. 22

2.4 Calorimeter map of one of eight identical $\eta - \phi$ octants. Division of hadronic detector components are labeled. 24

2.5 View of two of the VTPC modules. 27

2.6 Endplate of CTC showing alternating superlayers. 28

2.7 Endview of a portion of the CDT system. 28

2.8 Layout of a set of three CMU chambers on one central wedge. 30

2.9 End view of one CMU chamber showing position of sense wires. 30

2.10 CDF data acquisition pipeline. 31

2.11 CMU Level 1 trigger efficiency. 33
2.12 CFT Bin 0 trigger efficiency versus track P_t. 34

3.1 V5.1 Production data flowchart. 38
3.2 Integrated luminosity delivered by the Tevatron and the amount written to tape, for the CDF detector, versus time, for the 1988-89 Fermilab collider run. The dashed line indicates when the Level 2 DIMUON_CENTRAL_3 trigger was installed. 39
3.3 Distribution of dimuon event vertex without primary vertex cut. Cosmic rays have been removed. 43
3.4 Larger muon p_T versus smaller muon p_T passing all dimuon selection cuts except muon p_T cut. Cosmic rays have also been removed. 44
3.5 Distribution of muon tower electromagnetic energy without electromagnetic energy cut. Cosmic rays have been removed. 44
3.6 Distribution of muon tower hadronic energy without hadronic energy cut. Cosmic rays have been removed. 45
3.7 Distribution of muon ΔX track matching without ΔX matching cut. Cosmic rays have been removed. 45
3.8 Distribution of opposite-signed dimuon isolation without isolation matching cut and having an invariant mass between 11 and 40 GeV/c^2. Cosmic rays have been removed. 47
3.9 Plot of Track Isolation efficiency versus method. 50
3.10 Dimuon invariant mass plot for all events passing dimuon selection cuts. Cosmic ray events have not been removed. 51

4.1 Trigger efficiency of one leg of the Level 2 DIMUON_CENTRAL_3 trigger. Curves are upper and lower uncertainty used in monte carlo trigger model. 55
4.2 Comparison of ISAJET Drell-Yan monte carlo virtual photon transverse momentum distribution normalized to isolated dimuon data. 57

4.3 Comparison of ISAJET Drell-Yan monte carlo virtual photon rapidity distribution normalized to isolated dimuon data. 57
4.4 Comparison of ISAJET Drell-Yan monte carlo muon transverse momentum distribution normalized to isolated dimuon data. 58
4.5 Comparison of ISAJET Drell-Yan monte carlo muon track η distribution normalized to isolated dimuon data. 58

5.1 Three dimensional opening angle ($\Delta\phi_{3D}$) between opposite-signed dimuons. 62
5.2 $\Delta\phi_{3D}$ versus MAX$|D0|$ for opposite-signed dimuons. 63
5.3 Three dimensional opening angle ($\Delta\phi_{3D}$) between opposite-signed dimuons after MAX$|D0|$ cut of 0.15 cm. 64
5.4 Three dimensional opening angle ($\Delta\phi_{3D}$) between opposite-signed dimuons. for monte carlo generated Drell-Yan and Z° events. 65
5.5 Comparison of monte carlo and real data $\Delta\phi_{3D}$ opening angle after impact paramter cut of 0.15 cm. 66
5.6 Maximum Impact parameter (MAX$|D0|$) for dimuons with $\Delta\phi_{3D} > 175°$. 66
5.7 Dimuon invariant mass spectrum of real cosmic ray events taken from the MUO04 data stream. 68
5.8 Dimuon invariant mass with cosmic rays removed. 68
5.9 Di-τ invariant mass spectrum from 42.0 pb^{-1} of ISAJET monte carlo. . . 70
5.10 Dimuon invariant mass spectrum from τ decays. 70
5.11 Muon p_T spectrum from τ dimuons. 71
5.12 Dimuon invariant mass spectrum from τ decays passing fiducial and trigger requirements. 71
5.13 Dimuon track isolation for events passing all selection cuts, except track isolation, and also cosmic ray removal cuts. 73
5.14 Dimuon invariant mass spectrum with same-signed mass spectrum subtracted. 73

5.15 Opposite-signed dimuon isolation spectrum minus same-signed dimuon isolation spectrum. 76
5.16 Opposite-signed minus same-signed dimuon invariant mass spectrum for non-isolated events. 77

6.1 Calculated values of $M^3 d^2\sigma/dMdY|_{Y=0}$ compared to next-to-leading order predicted values. 81
6.2 Calculated values of $M^3 d^2\sigma/dMdY|_{Y=0}$ compared to largest and smallest next-to-leading order predicted values. 85

A.1 Dimuon invariant mass of CMUO-CMUO events at the J/ψ mass. The solid line represent opposite-signed events while the dashed line represent same-signed events. 87
A.2 Dimuon invariant mass of CMUO-CMUO events at the Υ mass. The solid line represent opposite-signed events while the dashed line represent same-signed events. 87
A.3 J/ψ parent p_T spectrum. 88
A.4 J/ψ muon p_T spectrum. 89
A.5 Three dimensional opening angle between muons from J/ψ. 89
A.6 Maximum track isolation of J/ψ muons. 90
A.7 Υ parent p_T spectrum. 90
A.8 Υ muon p_T spectrum. 91
A.9 Three dimensional opening angle between muons from Υ. 91
A.10 Maximum track isolation of Υ muons. 92
A.11 Distribution of muons from J/ψ and Υ events versus CDF ϕ. The bins are in units of 15° equivalent to one central wedge per ϕ bin. 92
A.12 Electromagnetic calorimetry tower energy for isolated J/ψ muons. 93
A.13 Hadronic calorimetry tower energy for isolated J/ψ muons. 94
A.14 ΔX track matching for isolated J/ψ muons. 94

A.15 ΔX track matching times track p_T for isolated J/ψ muons. 95
A.16 Maximum track impact parameter ($MAX|D0|$) for isolated J/ψ muons. . 95
A.17 Maximum track impact parameter ($MAX|D0|$) for isolated Υ muons. . . 96
A.18 CMU track stub ϕ position for all isolated J/ψ muons. Dashed lines indicate good CMU chamber fiducial region. 96
A.19 CMU track stub η position for all isolated J/ψ muons. Dashed lines indicate good CMU chamber fiducial region. 97

Chapter 1

Introduction and Theory of Drell-Yan Physics

1.1 Fundamental Particles and the Standard Model

The challenge to understand the fundamental nature of the universe has been a quest of mankind since the beginning of civilization. The question of how nature works and what it is made of has lead to the modern age of high-energy particle physics.

The ancient greek philosophers first began the concept of the smallest indivisible component of matter, which they called the atom. Chemists of the 19th century refined the early greek ideas and developed the periodic table of the elements and the rules governing chemical reactions. The large number of so called fundamental atoms and their regular order in the periodic table lead speculation that atoms were actually composed of other more fundamental particles. The early atomic scattering experiments of the 20th century showed that the atom was not fundamental but composed of a positively charged heavy nucleus surrounding by a cloud of negative electrons. This experimental information along with the development of quantum mechanics lead to an excellent understanding of the atomic nature of matter. Soon after, it was determined that the nucleus of atoms was composed of protons and neutrons. Physicists theorized that the

proton and neutron were held together by a strong force that acted only over the size of the nucleus. In 1935, the Japanese theorist Yukawa [1], postulated that this strong force was carried by a subatomic particle that traveled between the proton and neutron. During the 1940's, this subatomic particle was found in cosmic ray experiments and the age of particle physics was born.

Experiments in the 1950's and 1960's lead to the discovery of a large number of subatomic particles. Physicists built particle accelerators to generate larger energy beams to create more massive subatomic particles. Like the case of the periodic table of elements, scientists felt that these subatomic particles must be made up of still more fundamental particles. In the mid-1960's, a theory was developed that these subatomic particles are composed of more fundamental particles called quarks. The theory, called the quark model, required three different quarks that had fractional electric charge and carried a new type type of charge, which was called color. The quark model theory was not immediately accepted until scattering of very high-energy beams of electrons onto protons showed that the protons were indeed composed of more fundamental particles. The discovery of the J/ψ meson [2] [3] in 1974 provided the last needed evidence for the acceptance of quarks as the fundamental particles of protons and neutrons. These quarks along with leptons are presently accepted as the fundamental building blocks of matter. Table 1.1 gives the present list of quarks and leptons and their electrical charge [4]. The top quark has not yet been discovered but theoretical and experimental evidence supports its existence. The clearest, although indirect evidence comes from the measurement of the forward-backward asymmetry of bottom jet production in e^+e^- collisions. Experimental measurements match theoretical predictions from the standard model only if the top quark exists and is in a doublet with the bottom quark [5].

Along with the quarks and leptons, the particles that carry the forces of nature are required to complete the list of fundamental particles. Table 1.2 gives the list of fundamental forces and their respective carriers [4].

The present list of quarks, leptons, and force carriers are accepted as the fundamental

Charge	1st generation	2nd generation	3rd generation
Quarks			
+2/3	up	charm	(top)
-1/3	down	strange	bottom
Leptons			
-1	electron	muon	tau
0	electron neutrino	muon neutrino	tau neutrino

Table 1.1: Table of quarks and leptons.

Force	acts on	Force carrier	Spin
gravity	all massive particles	gravitron	2
electromagnetic	all electrically charged particles	photon	1
weak	quarks, leptons electroweak gauge bosons	$W^{\pm}, Z^{\circ}$	1
strong	quarks, gluons	eight gluons	1

Table 1.2: Table of fundamental forces and their carriers.

building blocks of nature. The interaction of these particles is described by the Standard Model of particle physics. The Standard Model consists of the unified electroweak theory, which describes the electromagnetic and weak interaction of particles, and Quantum Chromodynamics (QCD), which describes the strong interactions of particles. As of present, all experimental results can be fit within the framework of the Standard Model.

1.2 The Parton Model

Theoretical calculations using the standard model works well for individual quarks and gluons but not for composite particles, such as hadrons. Since hadrons themselves are not fundamental particles but are collections of quarks and gluons, accurate calculations of cross-sections become difficult because of the large number of initial constituent particles. Also, the strength of the strong force does not allow perturbative methods to be used for QCD calculations. The parton model [6] allows one to calculate cross-sections by making the assumption that high-energy collisions with hadrons can be modeled as collisions of individual quarks and qluons (collectively called partons) and all of the rest of the hadron can be ignored. At sufficiently high energies and momentum transfers, i.e. when Q^2 exceeds a few GeV^2, this approximation holds true [7]. At these higher momentum transfers, the quarks and gluons act as independent point-like particles and perturbative methods can be used for calculations.

The parton model allows many electroweak and QCD processes to be calculated for collision between hadrons. Using the parton model, one can calculate hadron-hadron collision cross sections as [8]

$$\sigma \sim \sum_{ij} \int dx_1 dx_2 f_i(x_1, Q^2) \hat{\sigma}_{ij} f_j(x_2, Q^2) \tag{1.1}$$

where $\hat{\sigma}_{ij}$ is the subprocess cross section, f's are the parton distribution functions (PDF's) of each hadron, and the summation runs over all types of partons that contribute to the subprocess. Each parton distribution is a function of x and Q^2 where x is the fraction of longitudinal momentum carried by the parton of the total hadron momentum and

Q^2 is the four momentum transferred in the subprocess reaction. The subprocess cross section, $\hat{\sigma}$, is evaluated at the subprocess center of momentum energy $\sqrt{\hat{s}}$.

1.2.1 Parton Distribution Functions

In order to determine cross sections using equation 1.1, one must have a set of parton distribution functions (PDF's). Several sets of PDF's have been generated from various sources of experimental data. At present, most of the information for PDF's comes from deep inelastic scattering fixed-target experiments at various values of x and Q^2. Deep inelastic experiments, e.g. $e + p \rightarrow e' +$ (anything), have the advantage that they can directly measure different quark and anti-quark distributions by using lepton (e, μ, and ν) probes on various targets and also accumulate large numbers of events. One disadvantage of deep inelastic scattering experiments is that since they are fixed-target experiments, they do not extend down into the region of small x, i.e. $x < 0.01$ for experimentally measurable regions of Q^2. The range of x probed by a given physics process can be found from $x_1 x_2 = M^2/s$ where M is the mass of the propagator particle and s is the square of the center-of-mass energy. The Tevatron, with a center of mass energy of 1.8 TeV, will allow the limit of x to be pushed much smaller. Production of Z° and $W^\pm$ events, in the region of central rapidity, probe a region of $x \sim 0.05$. Drell-Yan events with a mass of 10 GeV/c^2 will probe a lower limit of $x \sim 0.005$, in the region of central rapidity. Values of parton distributions measured in deep inelastic experiments can be evolved from their x and Q^2 to values used for Drell-Yan events at the Tevatron by use of the Altarelli-Parisi equations [9]. The measurement of the Drell-Yan, $W^\pm$, and Z° cross-sections will help directly determine these PDF's at small x.

Table 1.3 [10] gives a partial list of PDF's and the experimental data sets used to generate them. The PDF's by Duke and Owens (D-O) [11] and Eichten, Hinchliffe, Lane, and Quigg (EHLQ) [12] are distribution functions generated using data from experiments before about 1983. More accurate experiments and more refined global analysis carried out to next-to-leading order have since superceded these distributions. These consist

	D-O [11]	EHLQ [12]	(H)MRS [13]	DFLM [14]	M-T [15]
ν-DIS	CDHS	CDHS	CDHSW (CCFRR)	CHARM	CDHSW
μ-DIS	EMC	—	EMC,BCDMS	—	EMC, BCDMS
D-Y	E288,ISR	—	(E288),(E605)	—	E288,E605
Dir-γ	—	—	WA70	—	—

Table 1.3: Partial list of Parton Distribution Functions with references to experimental data used. Parentheses indicate the corresponding data are only partially used.

of (Harriman), Martin, Roberts, and Stirling ((H)MRS), [13] Diemoz, Ferroni, Longo, and Martinelli (DFLM) [14], and Morfin and Tung (M-T) [15] At the present time, the (H)MRS and M-T PDF's are most favored.

Figure 1.1 shows the up valence quark density in a proton for different sets of MRS and M-T PDF's at a $Q^2 = 400$ GeV^2 while figure 1.2 shows the gluon distribution for the same Q^2 [16]. These figure shows the relative uncertainty between the most favored parton distribution functions and therefore the uncertainty in calculating absolute cross sections for a given process. The arrow labeled fnal shows the value of x for a Drell-Yan event with an invariant mass of 20 GeV/c^2 measured in the central region of the CDF detector at Fermilab.

1.3 Drell-Yan Physics

One important probe of PDF's is the process known as the Drell-Yan process. The Drell-Yan process is the annihilation of a quark and antiquark, from a pair of interacting hadrons, into a virtual photon or Z° which decays into a lepton pair. This is the explanation given by Sidney Drell and Tung-Mow Yan [17] to describe the observation of muon pairs in high-energy hadron collisions by Christenson *et al* [18]. Several

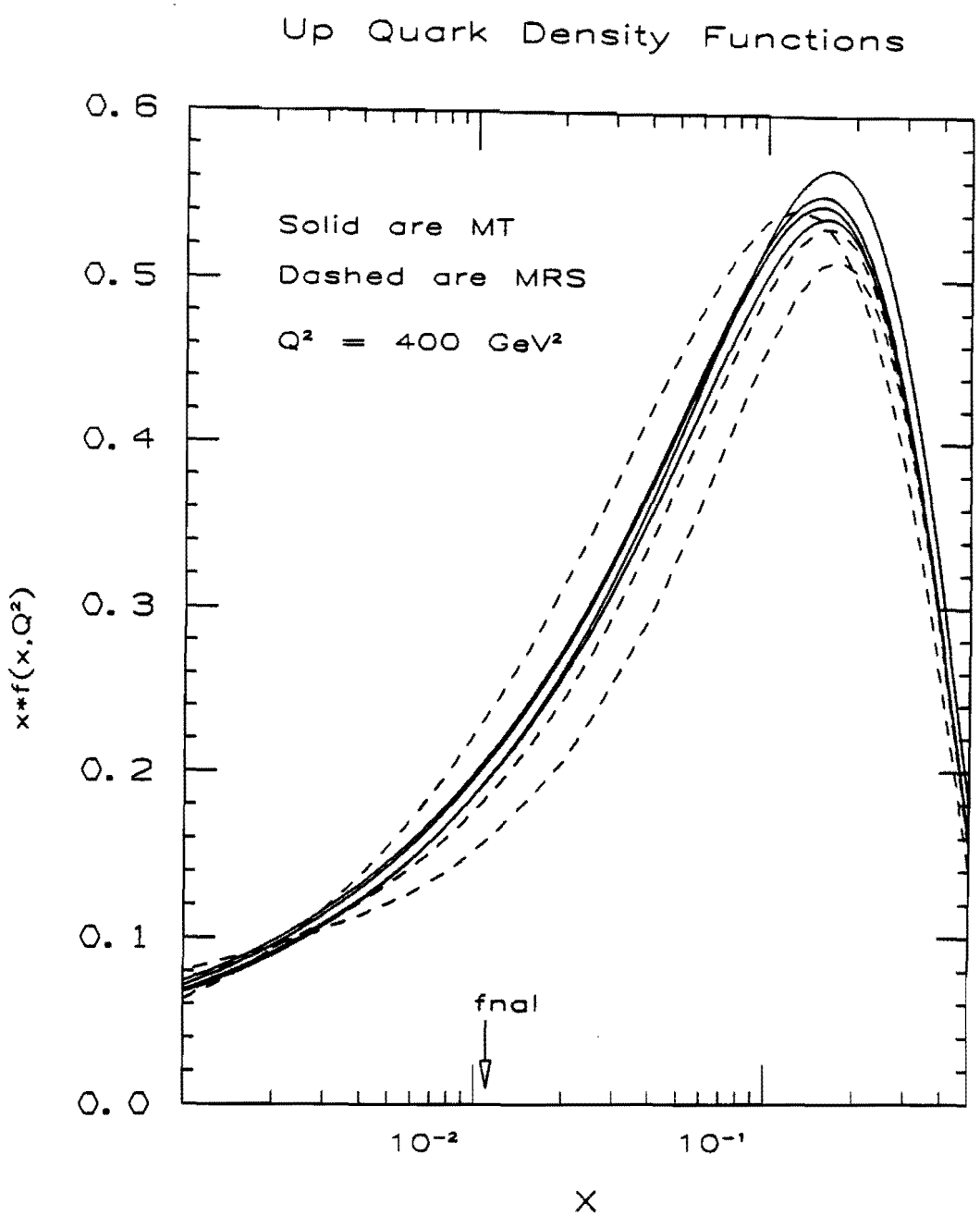

Figure 1.1: Up valence quark density for several PDF's as a function of x.

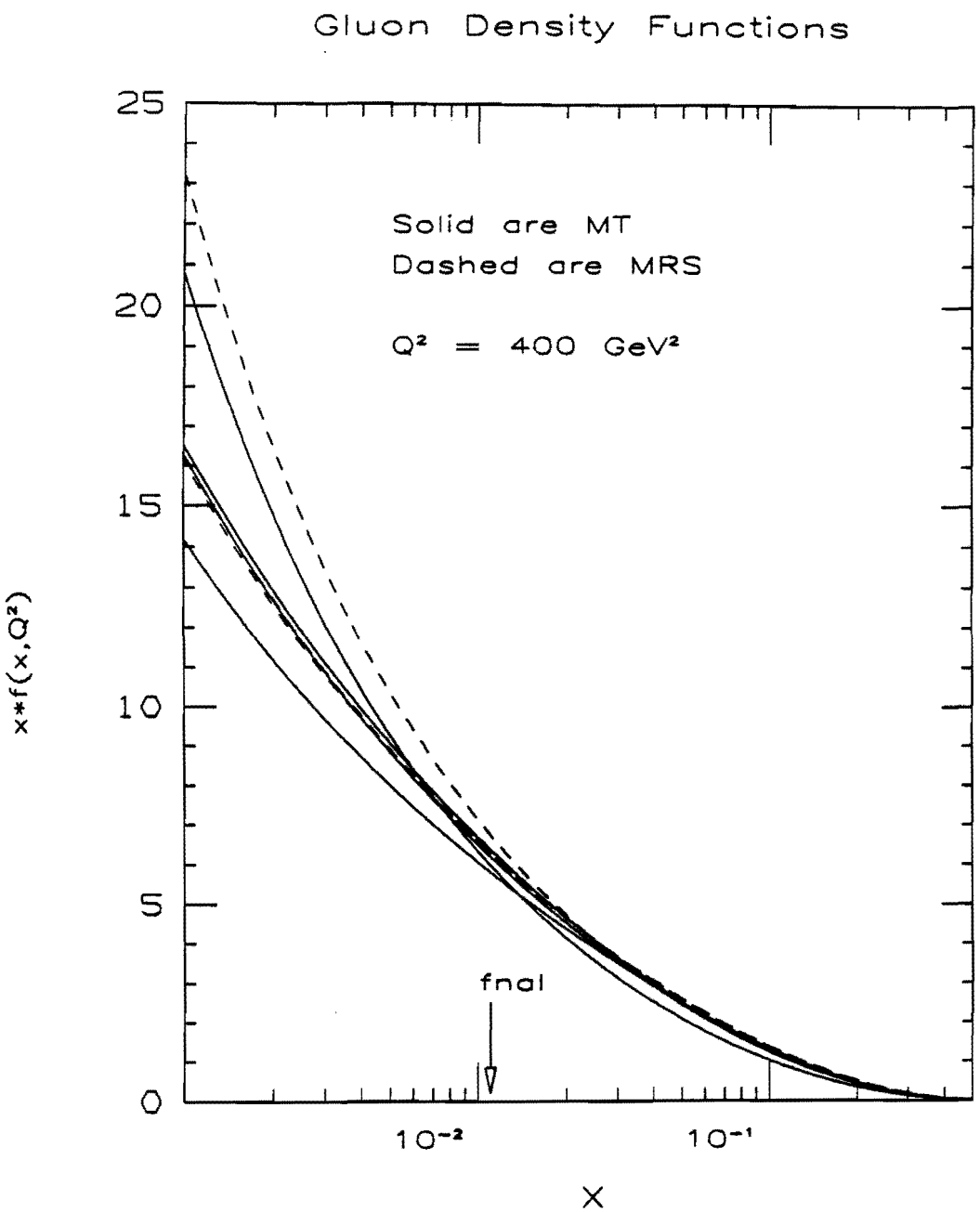

Figure 1.2: Gluon density for several PDF's as a function of x.

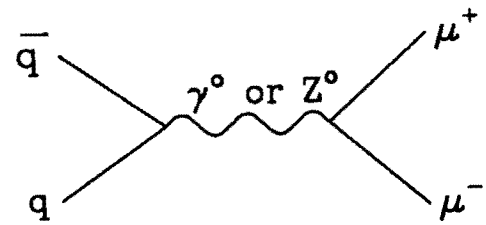

Figure 1.3: Lowest-order Drell-Yan Feynman diagram.

experiments have observed the excess of opposite-signed dileptons as a steeply falling continuum with increasing dilepton mass. Drell and Yan proposed that the continuum is produced by the process shown in figure 1.3. This process is purely electromagnetic and exactly calculable. Review articles on Drell-Yan physics have been written by Kenyon [19], Grosso-Pilcher and Shochet [20], and Rutherfoord [21] among others. This brief Drell-Yan derivation follows from these reviews.

Applying the parton model to figure 1.3, by using equation 1.1, one gets the Drell-Yan differential cross section to be [19]

$$\frac{d^2\sigma}{dx_1 dx_2} = \frac{4\pi\alpha^2}{9M^2}\sum_i {e_i}^2[q_{p_i}(x_1,Q^2)\bar{q}_{\bar{p}_i}(x_2,Q^2) + \bar{q}_{p_i}(x_1,Q^2)q_{\bar{p}_i}(x_2,Q^2)] \qquad (1.2)$$

where x_1 and x_2 are the momentum fraction of the quark or antiquark in the proton or antiproton, α is the electromagnetic coupling constant, e_i is the charge of the ith quark, and q_{p_i}, $\bar{q}_{p_i}$, $q_{\bar{p}_i}$, and $\bar{q}_{\bar{p}_i}$ are the quark/antiquark parton distribution functions for the proton/antiproton. The sum is over all flavors of quarks contained in the proton and antiproton that contribute to the Drell-Yan process. Equation 1.2 shows that the

Drell-Yan process is directly proportional to the quark and anti-quark distributions in the proton.

The kinematic constraints of the process yield the following relations. The energy of the virtual photon or Z° is

$$E_{\gamma,Z^\circ} = (x_1 + x_2)\sqrt{s}/2 \tag{1.3}$$

and has a virtual mass of

$$M_{\gamma,Z^\circ} = \sqrt{s x_1 x_2} = M_{l^+l^-} = M \tag{1.4}$$

where $\sqrt{s}$ is the proton-antiproton center of mass energy, which for the Tevatron is 1.8 TeV.

The Drell-Yan differential cross section can also be written in terms of the rapidity of the virtual photon or Z°, Y_{γ,Z°, so that equation 1.2 becomes

$$\frac{d^2\sigma}{dMdY_\gamma} = \frac{8\pi\alpha^2}{9Ms}\sum_i {e_i}^2[q_{p_i}(x_1,Q^2)\bar{q}_{\bar{p}_i}(x_2,Q^2) + \bar{q}_{p_i}(x_1,Q^2)q_{\bar{p}_i}(x_2,Q^2)] \tag{1.5}$$

where the virtual photon rapidity is defined as

$$Y_\gamma = \frac{1}{2}\ln[(E_\gamma + P_{l\gamma})/(E_\gamma - P_{l\gamma})] \tag{1.6}$$

and $P_{l\gamma}$ is the longitudinal momentum of the virtual photon. When the resulting virtual photon has zero longitudinal momentum, the differential cross section simplifies to

$$\left.\frac{d^2\sigma}{dMdY_\gamma}\right|_{Y_\gamma=0} = \frac{8\pi\alpha^2}{9Ms}\sum_i {e_i}^2[q_{p_i}(\sqrt{\tau})\bar{q}_{\bar{p}_i}(\sqrt{\tau}) + \bar{q}_{p_i}(\sqrt{\tau})q_{\bar{p}_i}(\sqrt{\tau})] \tag{1.7}$$

where

$$\tau = M^2/s = x_1 x_2 \tag{1.8}$$

and for $Y_\gamma = 0$

$$x_1 = x_2 = \sqrt{\tau} \tag{1.9}$$

One can rewrite equation 1.7 as;

$$M^3\left.\frac{d^2\sigma}{dMdY_\gamma}\right|_{Y_\gamma=0} = \frac{8\pi\alpha^2\tau}{9}\sum_i {e_i}^2[q_{p_i}(\sqrt{\tau})\bar{q}_{\bar{p}_i}(\sqrt{\tau}) + \bar{q}_{p_i}(\sqrt{\tau})q_{\bar{p}_i}(\sqrt{\tau})] = F(\sqrt{\tau}) \tag{1.10}$$

This shows that the differential cross section should scale as $\sqrt{\tau}$ and not independently on Q^2 and x. This is the property of scaling. Figure 1.4 [22] is a plot $M^3 d^2\sigma/dMdY|_{Y=0}$ as a function of $\sqrt{\tau}$ for various experiments at different beam energies.

1.3.1 Higher-Order QCD Corrections to the Drell-Yan Cross section and the Anomalous K-factor

The above Drell-Yan differential cross sections are derived in the simple parton model for only the lowest-order process. Early experiments observing the Drell-Yan process showed that the cross section was actually larger than predicted and that the perpendicular momentum (p_T) of the observed dileptons was also larger [19]. Figure 1.5 shows the experimentally measured values of the Drell-Yan differential cross section compared to the lowest-order predicted cross section from experiment E288 [23]. These differences between the lowest-order theory and experimental measurements were attributed to the neglect of higher-order QCD corrections. This results in the inclusion of the anomalous K-factor in the differential cross section.

$$\left.\frac{d^2\sigma}{dMdy}\right|_{y=0} = \frac{K8\pi\alpha^2}{9Ms}\sum_i {e_i}^2[q_{p_i}(\sqrt{\tau})\bar{q}_{\bar{p}_i}(\sqrt{\tau}) + \bar{q}_{p_i}(\sqrt{\tau})q_{\bar{p}_i}(\sqrt{\tau})] \tag{1.11}$$

The K-factor is defined to be the experimental measured cross section divided by the lowest-order predicted cross section.

The K-factor can be calculated within QCD by accounting for higher-order Drell-Yan processes, such as shown in Figure 1.6. The K-factor is calculated, for next-to-leading order corrections to the Drell-Yan cross section, to be [24]

$$K = 1 + \frac{\alpha_s}{2\pi}\frac{4}{3}\left(1 + \frac{4}{3}\pi^2\right) \tag{1.12}$$

where α_s is the strong coupling constant and is a function of Q^2.

$$\alpha_s(Q^2) = \frac{12\pi}{(33-2f)\ln(Q^2/\Lambda^2)} \tag{1.13}$$

for $Q^2 \gg \Lambda^2$, for which α_s is small. This shows that α_s is a function of the logarithm of Q^2 and also f, which is the number of quark flavors participating for the range of Q^2 of

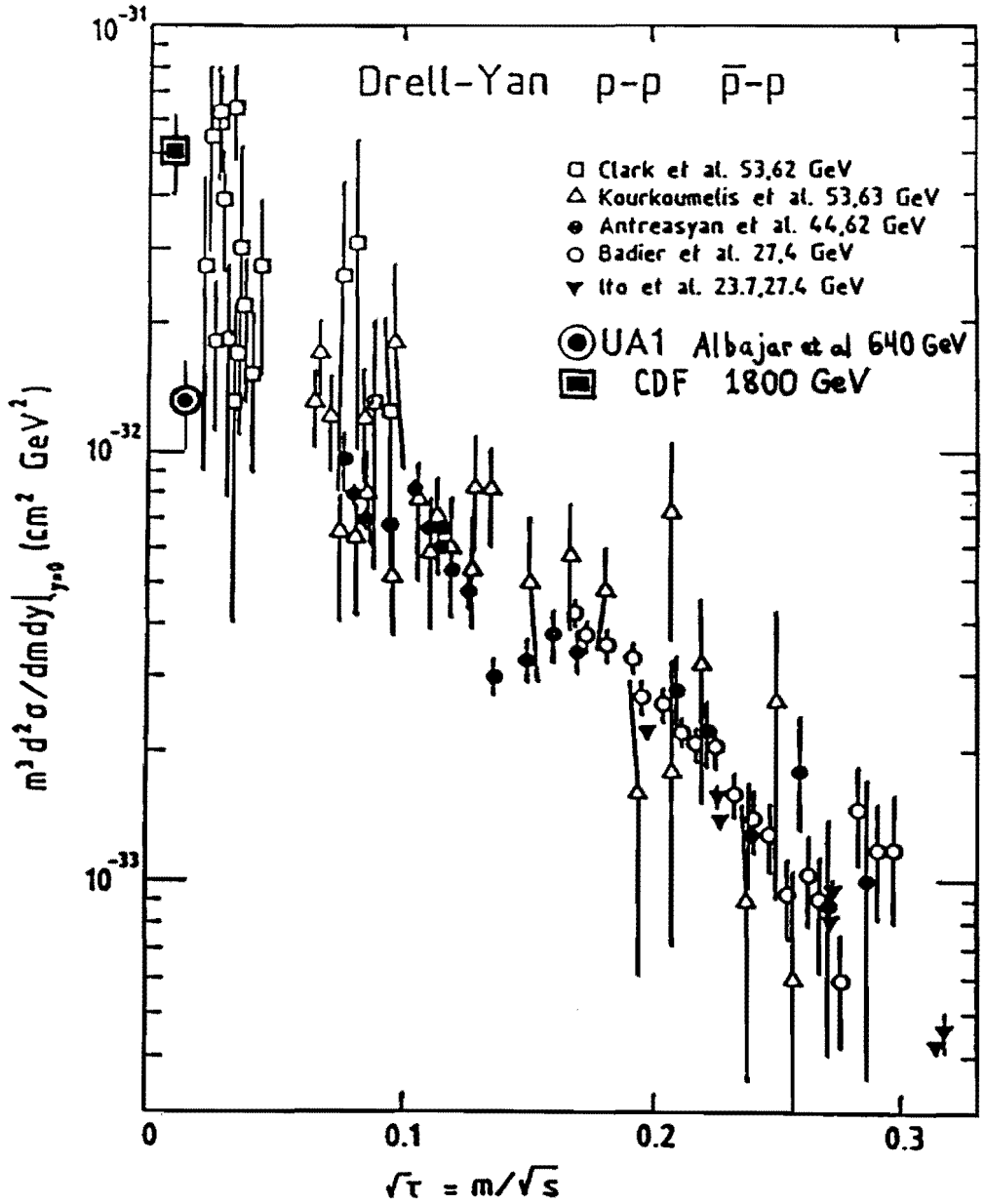

Figure 1.4: Experimental measurement of $M^3 d^2\sigma/dMdY|_{Y=0}$. This shows the scaling effect predicted by Drell-Yan theory.

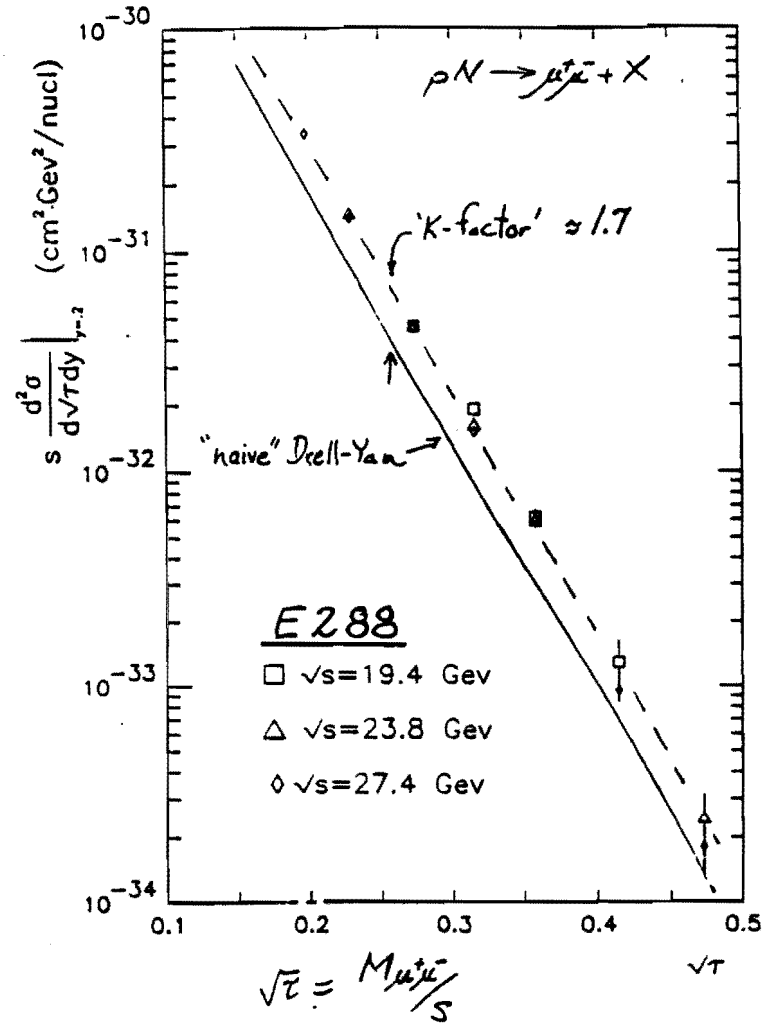

Figure 1.5: Comparision of the lowest-order predicted Drell-Yan cross section to that measured by experiment E288.

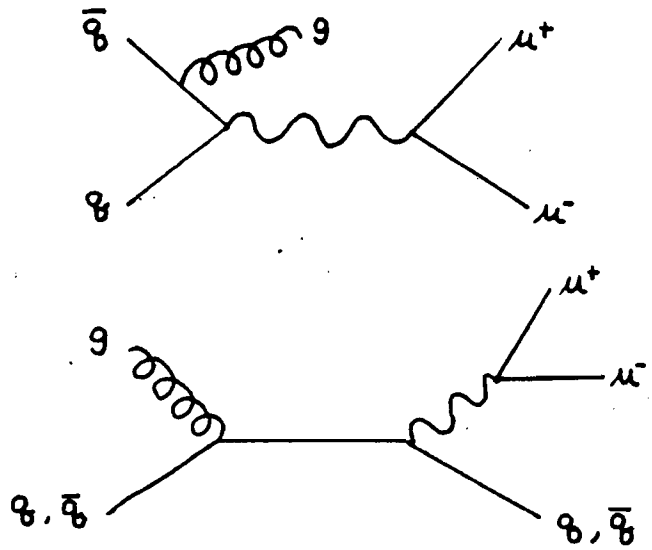

Figure 1.6: Higher-order Drell-Yan Feynman diagrams.

interest. Λ sets the scale of the QCD calculation and is normally between 100 and 400 MeV.

For sufficiently massive dileptons, higher order initial state corrections to the Drell-Yan process will not affect the quark momentum distributions. But, for smaller values of $\sqrt{\tau}$, the PDF's become distorted due to these higher order corrections. In general, higher order corrections should have a small effect on the Drell-Yan process, but because of the large numbers of gluons present at small $\sqrt{\tau}$ and the increase in cross sections due to color factors, higher order processes have a large effect on the Drell-Yan cross section. This implies that beyond next-to-leading order calculations of the Drell-Yan cross section may be necessary in order to compare to experimentally measured cross sections. It is hoped that further higher-order corrections to the cross section along with measurements of the Drell-Yan cross section at smaller $\sqrt{\tau}$ will help determine the small x form of PDF's.

1.4 Other Experimental Measurements

Several experiments have measured the Drell-Yan differential cross section. Figure 1.4 shows the Drell-Yan differential cross section as a function of $\sqrt{\tau}$ for various experiments. The figure verifies the Drell-Yan prediction of scaling, which is a key in showing that the parton model is valid in calculating the Drell-Yan cross section. Included in the figure are the differential cross section results of UA1 and the CDF measurement presented in this thesis. Other recent measurements of Drell-Yan events have been made by experiments E288 and NA3.

Experiment E288 [23] measured the continuum of dimuons produced from proton-nucleus collisions at Fermilab. The measurements were made with incident proton energies of 200, 300, and 400 GeV onto platinum and copper nuclei. Figure 1.5 shows the comparison of the lowest-order predicted cross section to the experimental measurement of experiment E288. This figure shows the measured values of the K-factor and the prediction of scaling by the parton model. Other experimentally measured K-factors are given in Table 1.4 [20]. The range of measured K-factors goes from about 1.6 to as high as 3.1 while the prediction from the next-to-leading order corrections is approximately 1.4 to 1.9. The discrepancy between measured and theoretical K-factors is attributed to different parameterization of parton distribution functions and the difference in the assumed momentum fraction carried by the gluons [20]. For this reason, recent experiments have no longer quote a K-factor, since the absolute number is too dependent on the choice of parton distribution functions.

Experiment NA3 [29] measured dimuon production from proton-platinum collisions at CERN. The experiment consisted of 400 GeV incident protons colliding with platinum nuclei. The Drell-Yan cross section was measured for dimuon invariant mass above 4.5 GeV/c^2. Figure 1.7 shows the shows the value of the K-factor measured by NA3 versus the dimuon invariant mass. The value has a small dependence on the dimuon mass but the absolute value of the K-factor is significantly larger than the next-to-leading order prediction. NA3 states that more precise prediction of high-order effects are need in

Experiment	Beam/Target	Energy $[\sqrt{s}]$(GeV)	K-factor
NA3 [26]	($\bar{p}$-p)/Pt	150	2.3±0.4
E537 [27]	$\bar{p}$/W	125	$2.45 \pm 0.12 \pm 0.20$
E288 [23]	p/Pt	300/400	~1.7
E439 [28]	p/W	400	1.6±0.3
NA3 [29]	p/Pt	400	$3.1 \pm 0.5 \pm 0.3$
CHFMNP [30]	pp	[44,63]	1.6±0.2
A^2BCSY [31]	pp	[44,63]	~1.7
OMEGA [32]	$\pi^{\pm}$/W	39.5	~2.4
NA3 [33]	$\pi^{\pm}$/Pt	200	2.3±0.5
	π^{-}/Pt	150	2.49±0.37
	π^{-}/Pt	280	2.22±0.33
NA10 [34]	π^{-}/W	194	2.77±0.12
E326 [35]	π^{-}/W	225	$2.70 \pm 0.08 \pm 0.40$

Table 1.4: Partial list of measured K-factors.

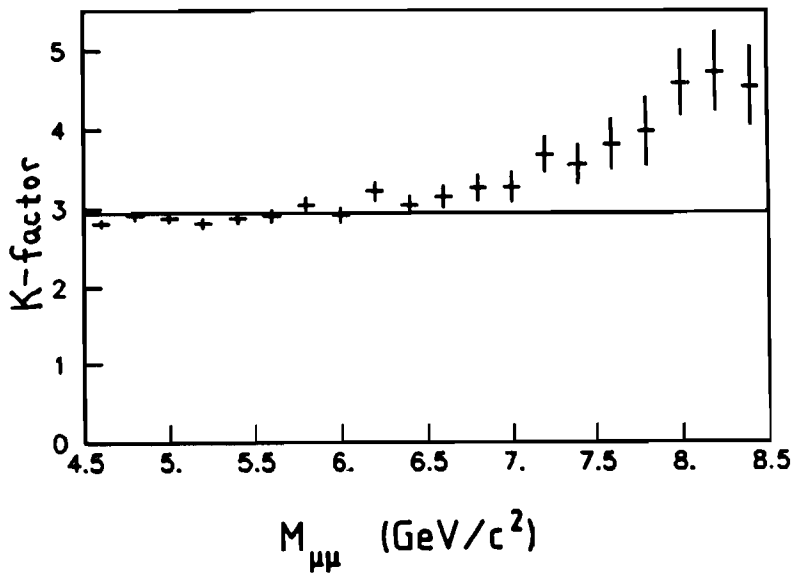

Figure 1.7: Measured K-factor versus mass for experiment NA3.

order to compare experimental measurement with theory.

The UA1 experiment at the CERN SPPS proton/anti-proton collider provides a measurement of the total and differential Drell-Yan cross section using dimuons [36]. Their values are measured at $\sqrt{s} = 640$ GeV.

$$\sigma(\mathrm{DY}, 11 < m^{\mu\mu} < 40\mathrm{GeV/c^2}) = 0.24 \pm 0.04_{stat} \pm 0.05_{sys}\mathrm{nb}$$

and

$$m^3 \frac{d^2\sigma}{dMdy}\bigg|_{y=0} (m^{\mu\mu} = 10GeV/c^2) = 15 \pm 5_{stat} \pm 3_{sys}\mathrm{nb}[\mathrm{GeV/c^2}]^2$$

These measurement by UA1 probes a smaller value of $\sqrt{\tau}$ than were previously avaliable from fixed-target experiments. The Drell-Yan cross section presented in this thesis occurs at an even smaller value of $\sqrt{\tau}$.

1.5 The Goal of this Thesis

This thesis describes the measurement of the inclusive differential Drell-Yan cross section from dimuon data taken during the 1988-1989 Fermilab collider run in $\bar{p}p$ collisions at a center-of-mass energy of $\sqrt{s} = 1.8$ TeV. The differential cross sections $d^2\sigma/dMdY|_{Y=0}$, and $M^3d^2\sigma/dMdY|_{Y=0}$, are calculated for the dimuon invariant mass range from 11 GeV/c^2 to 40 GeV/c^2 and for 70 GeV/c^2 to 110 GeV/c^2. The differential cross section $M^3d^2\sigma/dMdY|_{Y=0}$ is compared to a next-to-leading order theoretical prediction.

The goal of this thesis is threefold. First, the measurement of the cross section can test the validity of scaling by comparing to other cross sections at different values of $\sqrt{\tau}$. Second, data on low mass Drell-Yan production can be used to test current parton distribution function. Third, this analysis provides a framework for future Drell-Yan measurements at CDF using much larger data sets. The primary shortcoming of this analysis is in the low number of actual Drell-Yan dimuon events found by the CDF detector. Therefore, measurement of the differential cross section is severely limited by statistical error. Future measurements by CDF will have orders of magnitude increases in the data set.

The outline of this thesis proceeds as follows. This first chapter gives a brief overview of the Drell-Yan process in terms of the parton model. There is also a discussion of parton distributions functions and higher-order corrections to the naive Drell-Yan model. Chapter two gives a description of the Fermilab Tevatron collider and the CDF detector. Chapter three discusses the extraction of an isolated dimuon data set used for this analysis. Chapter four shows the ISAJET monte carlo data used to determine the Drell-Yan acceptance and trigger efficiency as a function of dimuon invariant mass. Chapter five determines the remaining background in the isolated dimuon sample and how to remove it or account for it. Chapter six shows the calculation of the differential cross section and comparison to theory. This chapter also has predictions for this analysis in future collider runs.

Chapter 2

The Fermilab Tevatron and CDF Detector

2.1 The Tevatron Collider

The Fermilab National Accelerator Laboratory (FNAL) located outside of Chicago. Illinois one of the United States main laboratory for high-energy physics research using protons. The laboratory is divided into two main types of operation, fixed target mode and collider mode. Fixed target mode consists of accelerating protons to their operating energy and then extracting them to the various target areas. Collider mode consists of collisions of counter-rotating beams of protons and anti-protons stored in the Tevatron ring. Figure 2.1 shows the layout of the Fermilab accelerator along with various experimental areas. Since this analysis consists of data taken in the collider mode, fixed target mode will not be discussed.

Protons used for collider mode are accelerated in several stages [36]. The first stage of acceleration consists of a Cockcroft-Walton electrostatic accelerator. Negative hydrogen ions are accelerated to 500 KeV in this stage and then feed into a linac accelerator that elevates the energy to 200 MeV. The electrons are then removed and the remaining protons are accelerated by a booster ring to 8 GeV. Six bunches of protons are then

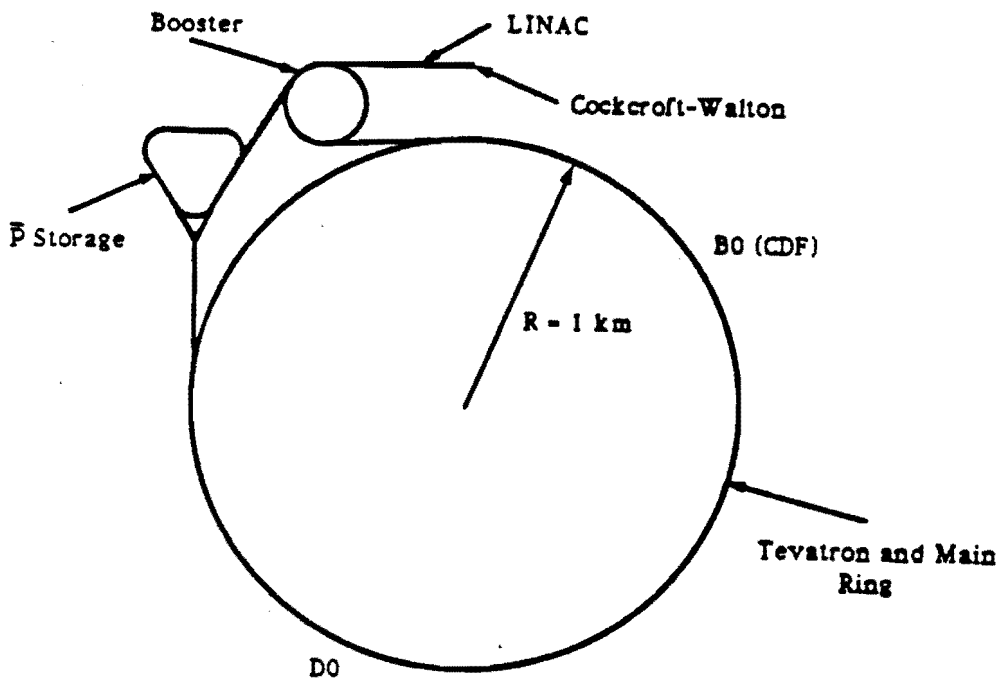

Figure 2.1: Fermilab National Accelerator (FNAL).

placed into the Main ring before further acceleration occurs. The bunches of protons are then accelerated to 150 GeV before being injected into the superconducting Tevatron ring. Once in the Tevatron, the bunches are then ramped to their operating energy of 900 GeV.

While in the collider mode, the main ring is used to create anti-protons. The anti-protons are created from collision of protons on a tungsten-rhenium target and then stored in the anti-proton accumulator. After enough anti-protons are stored they are then injected into main ring and then into Tevatron in the opposite direction of the stored protons.

The stored protons and anti-protons collide at various interaction points around the Tevatron ring. The CDF detector sits at the proton-antiproton ($\bar{p}p$) interaction point B0 on the Tevatron ring. Figure 2.2 show a longitudinal distribution of $\bar{p}p$ collision vertices centered in the CDF detector.

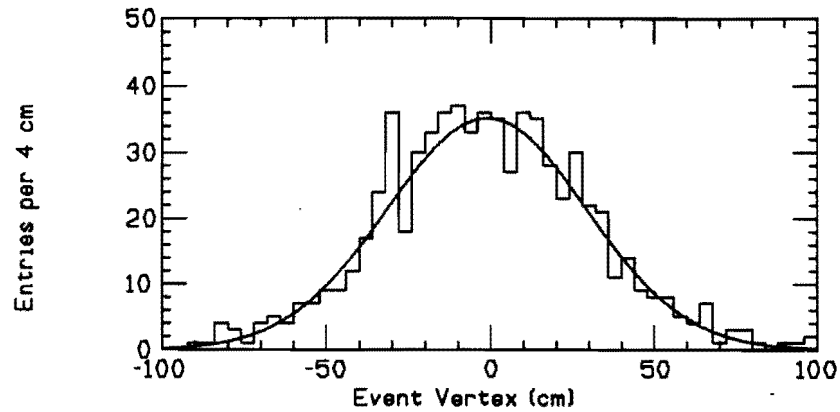

Figure 2.2: Distribution of Z positions for CDF event vertices with superimposed gaussian of a mean of 0.0 cm and a σ of 30.0 cm.

2.2 The CDF Detector

The Collider Detector at Fermilab (CDF) is a colliding beam spectrometer used to study $\bar{p}p$ interactions at a center of mass energy of $\sqrt{s} = 1.8$ TeV. Figure 2.3 shows the detector with major subsystem detectors labeled, as well as the proton and anti-proton directions and the CDF coordinate system. The main features of the CDF detector are its nearly hermetic calorimetry and its 1.5 tesla superconducting central solenoid magnet. The following section describe portions of the CDF detector that are relevant to this analysis and is taken mostly from [37].

2.2.1 The CDF Calorimetry System

The CDF calorimetry is divided into three separate regions in pseudorapidity; central ($|\eta| < 1.0$), endplug ($1.0 < |\eta| < 2.2$), and forward ($2.0 < |\eta| < 4.2$), where η is defined as;

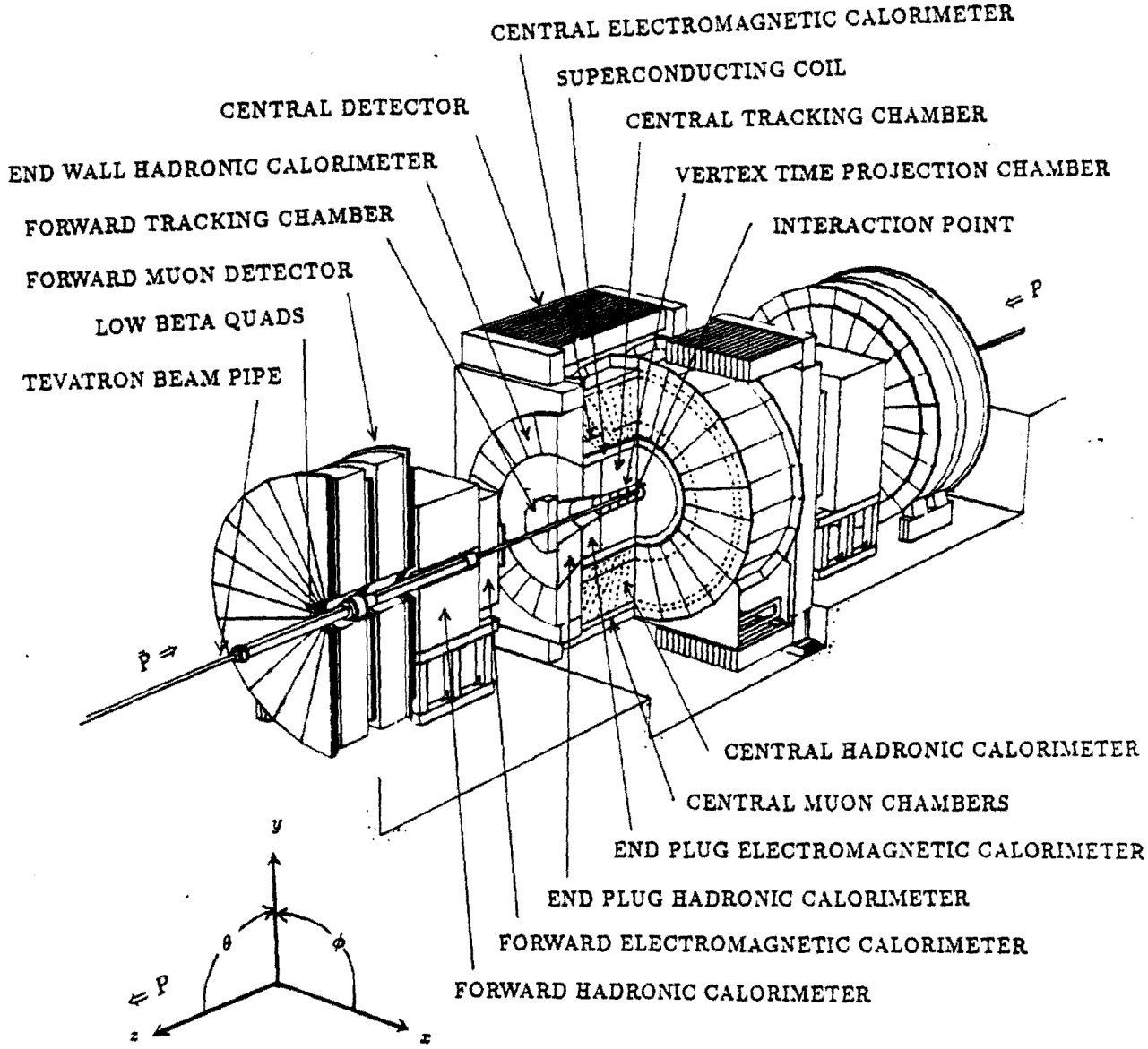

Figure 2.3: CDF detector.

$$\eta = -\ln(\tan\frac{\theta}{2})$$

The calorimetry is further divided into projective towers in $\eta - \phi$ space. These towers point to the interaction vertex at the center of the CDF detector. All of the calorimetry is also divided, along a radial line from the interaction vertex, into an electromagnetic calorimeter followed by a hadronic calorimeter. Figure 2.4 shows the calorimeter tower map in one of eight identical $\eta - \phi$ octants and also labels the hadronic detector components by their η coverage. This analysis uses only the central calorimetry system to determine the amount of energy a Drell-Yan muon candidate deposits. For completeness, the endplug and forward calorimetry systems are also discussed.

The central calorimetry is divided into units of 15° in the ϕ direction and into units of $\eta = 0.1$ in the Z direction. The central electromagnetic calorimeter is a scintillator/lead calorimeter while the central hadronic calorimeter is a scintillator/iron calorimeter. Table 2.1 gives a brief summary of some important properties of the CDF central calorimetry.

The endplug and forward calorimetry is divided into units of 5° in the ϕ direction and into units of $\eta = 0.1$ in the Z direction. The endplug and forward calorimeters differ from the central calorimeters in that they use proportional tube chambers with cathode pad readout as their active medium. Table 2.2 gives a brief summary of some important properties of the CDF endplug and forward gas calorimetry.

2.2.2 The CDF Tracking System

The CDF tracking system, for the 1988-1989 data runs, consists of three separate subsystems that are cylindrical in shape and concentric to the Tevatron beam pipe. All three of these tracking subsystem lie within the 1.5 T superconducting solenoid magnet. The combination of these three subsystems allows CDF to determine the event vertex and three dimensionally reconstruct most charge tracks that appear in the region of central η (-1.0< η <1.0). Table 2.3 gives a brief summary of some important properties

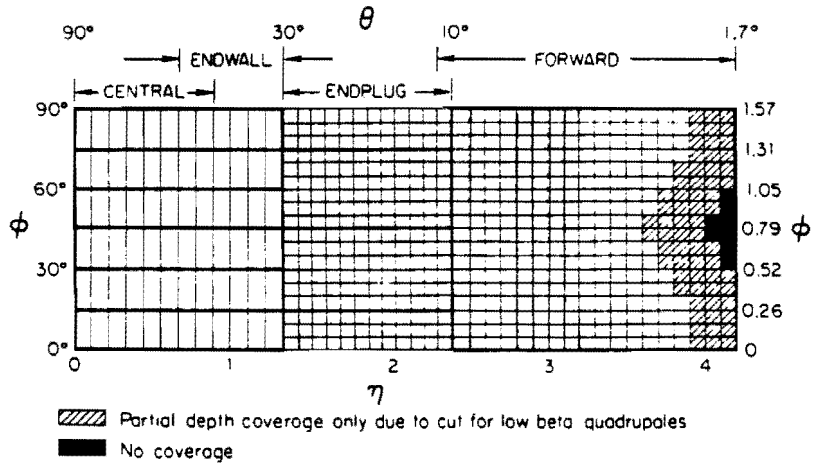

Figure 2.4: Calorimeter map of one of eight identical $\eta - \phi$ octants. Division of hadronic detector components are labeled.

	Central		Endwall
	EM	Hadron	Hadron
$\|\eta\|$ coverage	0-1.1	0-0.9	0.7-1.3
Tower size, $\Delta\eta \times \Delta\phi$	$\sim 0.1 \times 15°$	$\sim 0.1 \times 15°$	$\sim 0.1 \times 15°$
Active medium	polystyene scintillator	acrylic scintillator	acrylic scintillator
Scintillator thickness	0.5 cm	1.0 cm	1.0 cm
Number of layers	31	32	15
Absorber	Pb	Fe	Fe
Absorber thickness	0.32 cm	2.5 cm	5.1 cm
Energy resolution (σ/E) at 50 GeV [%]	2	11	14

Table 2.1: Summary of central calorimeter properties.

	Endplug		Forward	
	EM	Hadron	EM	Hadron
$\|\eta\|$ coverage	1.1-2.4	1.3-2.4	2.2-4.2	2.3-4.2
Tower size, $\Delta\eta \times \Delta\phi$	$0.09 \times 5°$	$0.09 \times 5°$	$0.1 \times 5°$	$0.1 \times 5°$
Scintillator thickness	$0.7 \times 0.7\text{cm}^2$	$1.4 \times 0.8\text{cm}^2$	$1.0 \times 0.7\text{cm}^2$	$1.5 \times 1.0\text{cm}^2$
Number of layers	34	20	30	27
Absorber	Pb	Fe	94 % Fe, 6 % Sb	Fe
Absorber thickness	0.27 cm	5.1 cm	0.48	5.1 cm
Energy resolution (σ/E) at 50 GeV [%]	4	20	4	20

Table 2.2: Summary of endplug and forward gas calorimeter properties.

of the CDF tracking systems.

The inner most tracking subsystem is the Vertex Time Projection Chamber (VTPC). The VTPC has been optimized to provide good R-Z resolution for charged tracks through the use of 8 modules mounted end-to-end along the beam axis. Figure 2.5 shows two of the eight VTPC modules. The VTPc's main purpose, for this analysis, is determine the event vertex and identify multiple vertices, for a given beam crossing.

The next layer of tracking chamber is the Central Tracking Chamber (CTC). The CTC is a long cylindrical drift chamber used to precisely measure charged tracks in the region of central η. The CTC surrounds the VTPC and provides most of the track information used to reconstruct the track into three dimensions. The CTC consists of 5 layers of axial wires alternating with 4 layers of stereos wires. These layers are given the generic name of superlayers. The axial superlayers provide good track resolution in the R-ϕ direction. The stereo superlayer wires are canted by $\pm 3°$ with respect to the beam axis. This enables the stereo superlayers to provide Z information about the tracks. Figure 2.6 is an end view of the CTC endplate which shows the alternating superlayers

	VTPC	CTC	CDT
Wire organization	8 modules 16 octants/module 24 wires/octant 24 pads/octant	9 superlayers 5 axial superlayers of 12 wires each 4 stereo superlayers of 6 wires each	3 layers of tubes
Inner layer coverage	$3.5° < \theta < 176.5°$ $-3.5 < \eta < 3.5$	$15° < \theta < 165°$ $-2.0 < \eta < 2.0$	$40° < \theta < 140°$ $-1.0 < \eta < 1.0$
Outer layer coverage	$8.7° < \theta < 171.3°$ $-2.6 < \eta < 2.6$	$40° < \theta < 140°$ $-1.0 < \eta < 1.0$	$40° < \theta < 140°$ $-1.0 < \eta < 1.0$
Number of (sense) wires	3072 wires 3072 pads	6156	2016
Spatial precision (per hit)	200-500 μm (0-15 cm drift)	<200 μm (r-ϕ) < 6 mm (Z)	< 200 μm (r-ϕ) 2.5 mm (Z)
2-track resolution	6 mm/θ (Z) 6 mm(r) 3 cm (ϕ)	3.5 mm	

Table 2.3: Summary of central tracking chamber properties.

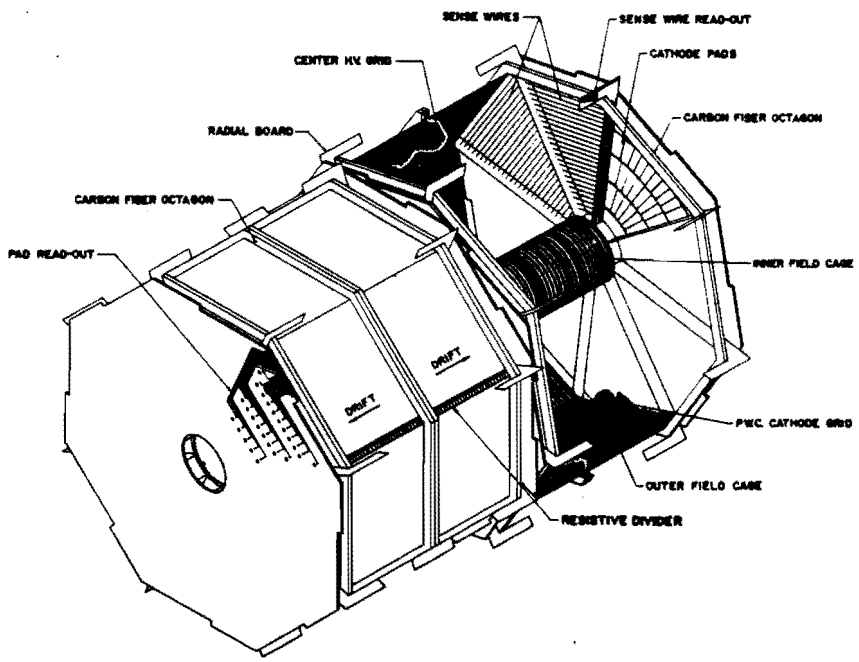

Figure 2.5: View of two of the VTPC modules.

of axial and stereo wires and also shows that in each superlayer, the rows of sense wires are tilted by 45° to a radial line from the beam axis to correct for the Lorentz angle of the electron drift in the 1.5 T magnetic field. The CTC provides a transverse momentum (p_T) resolution of $\delta p_T/p_T{}^2 \leq 0.002$ for central η tracks.

The final layer of tracking chamber are the Central Drift Tubes (CDT). The CDT is a set of three layers of proportional tubes that are 1.27 cm in diameter surrounding the CTC and running parallel to the beam axis. Figure 2.7 shows an endview of a portion of the CDT chamber. The CDT has been optimized to provide R-ϕ-Z information using charge division and drift-time.

2.2.3 The CDF Muon Detection System

The CDF muon detection consists of a central muon (CMU) system covering $|\eta| < 0.65$ and a forward muon (FMU) system covering $2.0 < |\eta| < 3.6$. Since only the CMU system is used for this analysis, the FMU system will not be discussed. The CMU detector

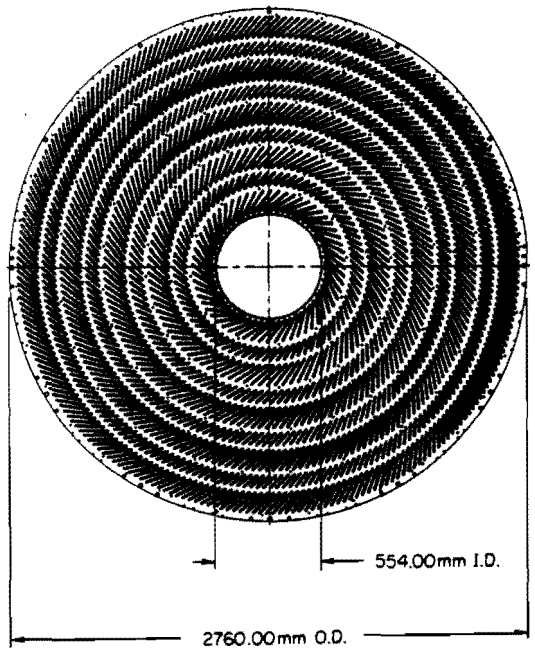

Figure 2.6: Endplate of CTC showing alternating superlayers.

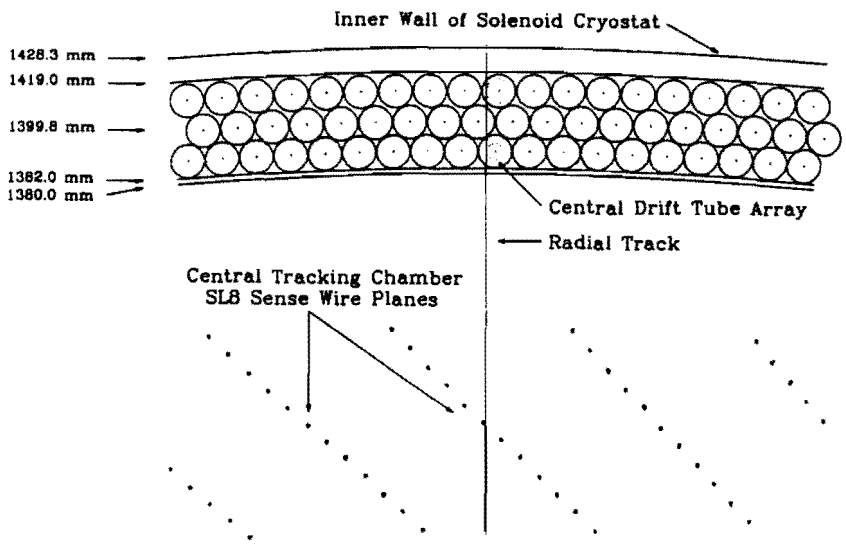

Figure 2.7: Endview of a portion of the CDT system.

system is divided in ϕ into 24 15° units called central wedges and is also divided into positive η and negative η.

The CMU system consists of four layers of proportion drift chambers located behind the CHA in each central wedge. Particle reaching the CMU chambers, from a $\bar{p}p$ collision, must penetrate $\sim$ 5 interaction lengths of material. This results in a good selection of minimum ionizing particles while allowing approximately 1 out of 150 hadrons to non-inactively reach the CMU chambers. Figure 2.8 shows the layout of the CMU chambers in one of the central wedges while figure 2.9 shows the arrangement of sense wires in four layers of a give CMU chamber. The CMU chambers use drift-time to determine R-ϕ information and charge-division to determine Z information. This allows the CMU chambers to calculate four points in R-ϕ-Z space and to create a CMU track stub.

2.3 Data Acquisition Path

The data acquisition system for the CDF detector consists of the readout electronics, which convert the actual detector analog signals into digital values, and also the trigger and event management electronics, which control when an event is selected and written to magnetic tape. Figure 2.10 shows the general block diagram of the CDF data acquisition pipeline.

The readout electronics for the CDF detector are divided into two separate systems. The RABBIT (Redundant Analog Bus-Based Information Transfer) system is used to readout all the CDF calorimetry systems and the central muon system [38]. The RABBIT system is a product of the Fermilab Particle Instrumentation Group. The FASTBUS system is a commercially based data acquisition system that is used to readout the CDF tracking systems and the CDF trigger system [39]. Most of the CDF trigger system is also located in the FASTBUS system. Management of the data taking procedure is monitored and controlled by the FASTBUS systems, including the trigger supervisor, the buffer manager, and the event builder. The FASTBUS system is directly connected

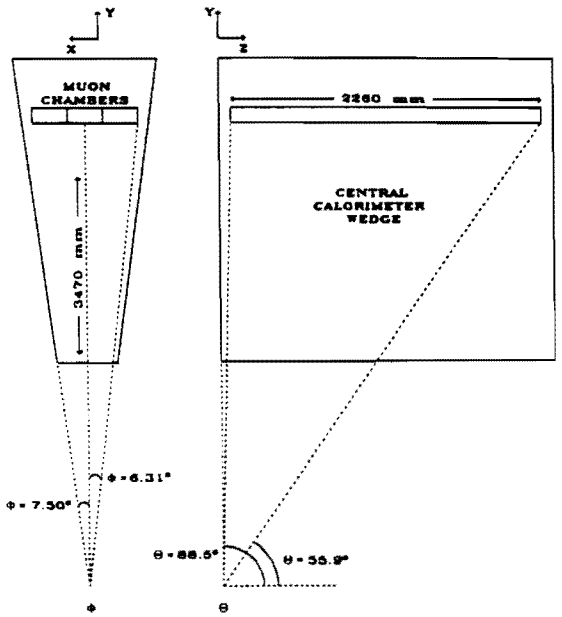

Figure 2.8: Layout of a set of three CMU chambers on one central wedge.

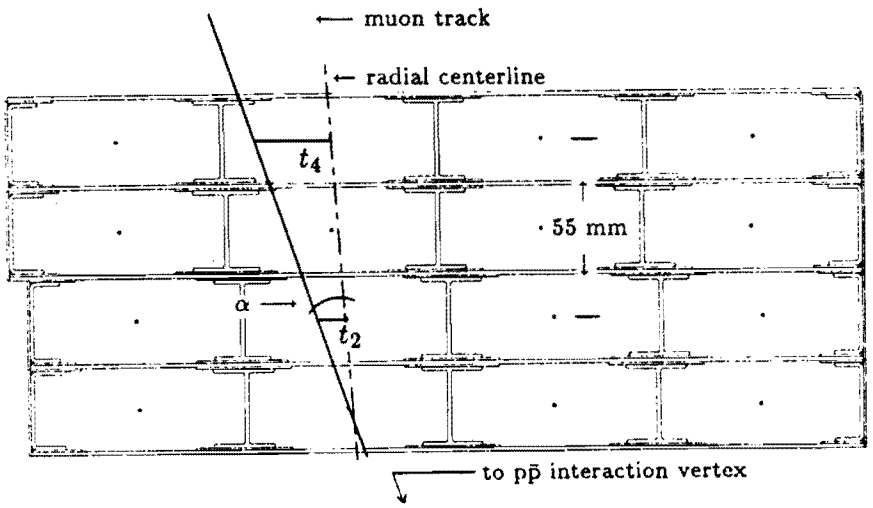

Figure 2.9: End view of one CMU chamber showing position of sense wires.

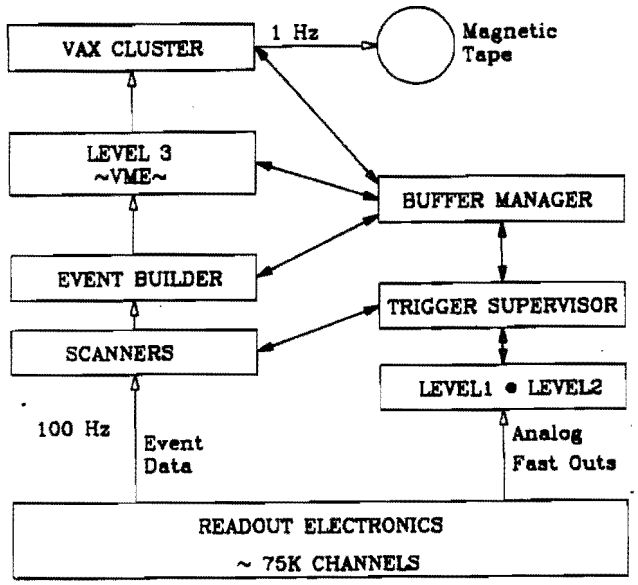

Figure 2.10: CDF data acquisition pipeline.

to the DEC VAX cluster of computers that record the event to magnetic tape.

2.4 CDF Trigger System and the Central Dimuon Trigger

The 1988-89 data collider beam run uses 6 bunches of proton and 6 bunches of counter-rotating antiprotons resulting in a 3.5 μsec time between collisions. The rate at which the protons and antiprotons collide is measured by the luminosity of the accelerator. The luminosity is given by

$$\text{Luminosity} = \frac{N_p N_{\bar{p}} C}{4\pi\sigma^2} \tag{2.1}$$

where N_p and $N_{\bar{p}}$ are the number of protons and antiprotons per bunch, C is the bunch crossing rate, and σ is the rms width of the gaussian beam profile. An average Tevatron collider luminosity of $1 \times 10^{30}\text{cm}^{-2}$ results in a collision rate of about a 42 KHz event rate. The data acquisition system has an approximate 10 Hz limit for writing to magnetic tape. This requires that the trigger select 1 event out of every 4200 collisions. This selection is accomplished with a 4 stage or level trigger system. All four levels of the trigger system

must fire for an event to be written to tape.

The Level 0 portion of the trigger is used to determine if a hard or inelastic collision has occurred at the B0 interaction point. This Level 0 trigger is accomplished by a set of scintillator counters on either side of central detector near the beam pipe. If there is a coincidence of hits in counters on the east and west side of the central detector, that occurs within 100 nsec of a beam crossing, then the Level 0 trigger is fired. The Level 0 trigger occurs in less time than the 3.5 μsec between beam crossings, so no dead time is incurred. If the Level 0 trigger fires, the trigger system freezes the data acquisition electronics on the detector, to hold the information of the event and to prevent further events from interfering with the data. The trigger system now waits for the Level 1 trigger to either pass the event or reject it.

2.4.1 Level 1 Central Muon Trigger

The Level 1 portion of the trigger system has several different possible triggers for different types of events, like electron events, missing E_T events, jet events, muon events, etc. Many of these different types of trigger overlap for a given event and all of them run in parallel, at the Level 1 stage. The Level 1 portion of the trigger system is determined within 7.0 μsec Once any of the possible level 1 triggers fire, the trigger system continues to hold the event in the detector data aquisition electronics and freezes out further events. If the level 1 trigger does not fire, the trigger system releases the detector to accept further events.

For this analysis, the Central Muon (CMU) Level 1 trigger is the only level 1 trigger of interest and the other level 1 triggers will not be discussed. The level 1 CMU trigger is determined by examining the difference in arrival times of hits in different layers of a CMU chamber. This measurement allows one to determine the slope of the track in the CMU chamber and thus the transverse momentum (p_T) of the track. The CMU Level 1 trigger is then passed if the difference in the hit arrival times is less than some set value. Figure 2.9 shows how the slope of a track passing through a CMU chamber is measured.

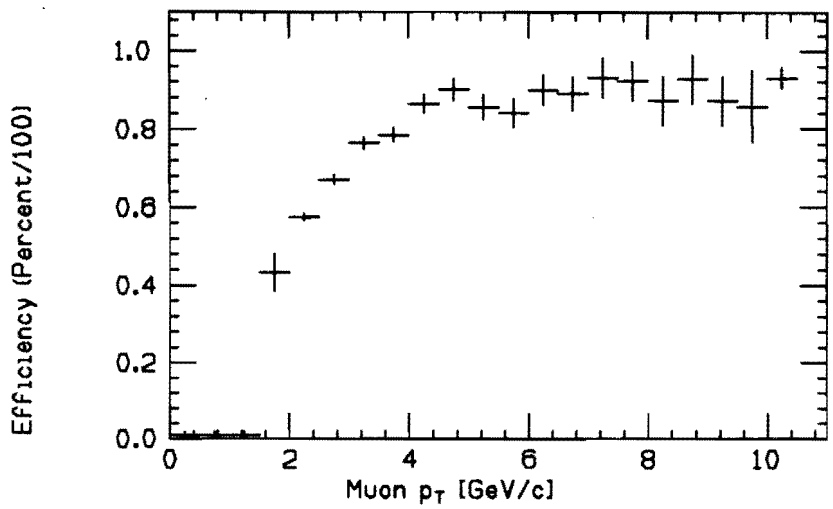

Figure 2.11: CMU Level 1 trigger efficiency.

Since tracks reaching the CMU chambers must pass through the central calorimetry system, they multiple-scatter. This multiple-scattering causes the slope of the track at the CMU chambers to differ from the actual slope of the track as it leaves the CTC tracking chamber, hence, the p_T measurement at the CMU chambers is different than the true track p_T. Figure 2.11 [40] shows the CMU Level 1 trigger efficiency as a function of the track CTC track p_T. The slow turn-on the the trigger efficiency is due to the multiple-scattering the the track.

2.4.2 Level 2 Central Dimuon Trigger

Once a Level 1 trigger fires, the data acquisition system remains frozen while the Level 2 portion of the CDF trigger determines if any of the Level 2 triggers fires. The data taken for this analysis is required to pass the Level 2 central dimuon trigger called DIMUON_CENTRAL_3. This is the name given to the Level 2 dimuon trigger that requires two 3 GeV muons.

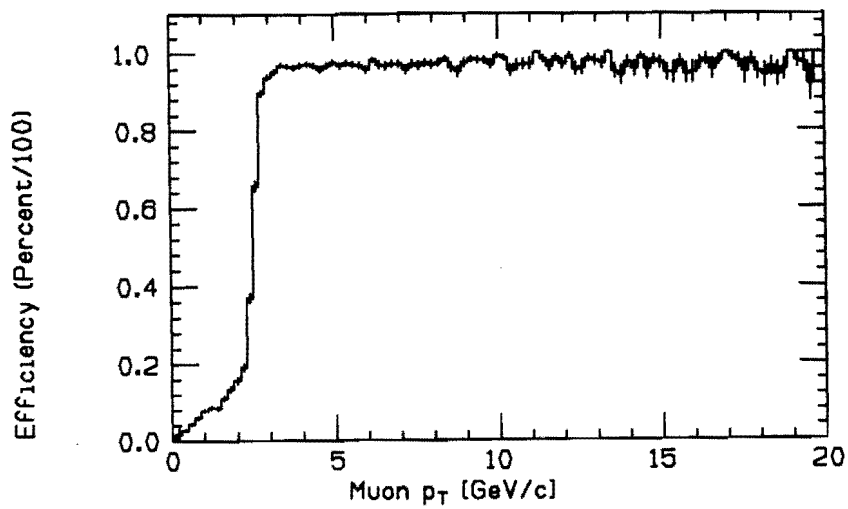

Figure 2.12: CFT Bin 0 trigger efficiency versus track P_t.

The Level 2 DIMUON_CENTRAL_3 trigger requires that two non-adjacent CMU L1 triggers match to two extrapolated Central Fast Tracker (CFT) tracks. The CFT is a fast hardware track-finder for the CDF Central Tracking Chamber (CTC) [41]. It quickly determines the p_T of charged tracks traversing the CTC. The CFT has several p_T bin levels that a track may pass. Figure 2.12 [42] shows the trigger efficiency as a function of track p_T for CFT bin level of interest. Once a track passes a given bin level, the information is sent to the Central muon matchbox trigger system.

The central muon matchbox trigger system takes Level 1 CMU trigger information and the CFT track information and determines if a match can be made. The matchbox takes the CFT track p_T and ϕ direction and propagates the track, by means of a lookup table, out to the radius of the CMU chambers. It then determines if there is a CMU Level 1 trigger within 15.0° in ϕ. The muon matchbox does not make a match requirement in the Z direction. If there are two such matches in a given event and the matches do not have Level 1 triggers in adjacent wedges, then the level 2 DIMUON_CENTRAL_3 trigger is satisfied.

There is also a Level 3 trigger system that is a software based trigger running in a VME microcomputer farm, but this level is always passed for Level 2 DIMUON_CENTRAL_3 triggers, and therefore will not be discussed.

Chapter 3

Dimuon Data Selection

3.1 Offline Data Reconstruction

The tapes of digitized detector data must now be reconstructed from raw detector voltage levels into physics objects. This is accomplished using a computer program called PRODUCTION_V5_1 [43], which assembles various physics objects, such as muons, electron, jets, etc. The production program generates these physics objects in several stages. The first stage is take raw detector data along with geometric and calibration database information and to make detector elements. These are single pieces of hit information for a track. The detector elements are then linked together to form segments. For calorimeter detectors, a clustering algorithm runs to link single calorimeter elements into jet clusters. For tracking, a pattern reconstruction and tracking fitting algorithm link individual tracking elements into complete tracks. The muon segment reconstruction follows the same method as the tracking segment reconstruction, that is, the hits in the central muon (CMU) detectors are assembled into a single short track or CMU stub. These various tracking and calorimetry segments are combined to form primitive physics objects like electron and muon candidates.

For this analysis, only central muon objects are of interest. The reconstruction program labels central muon objects as CMUO data banks. In order to make a CMUO data

bank, two detector segments must be present for each possible muon candidate. There must be CMU stub and there must be a central tracking chamber segment (CTCS). The CTCS segment must extrapolate to the CMU stub and match to the stub within 17.0 cm in the $R - \phi$ plane. Each possible muon candidate is put into a separate CMUO data bank. This CMUO bank is now a possible central muon candidate and contains information about the muon track as well as calorimetry energy information around the muon track.

Once physics objects, like CMUO data banks, are made, a general data filter is used to determine to which physics data output stream the event should be written. Figure 3.1 shows a flowchart of events in the PRODUCTION_V5_1 program algorithm and the dividing of reconstructed events into different data output streams. CMUO data bank events go into different data streams depending on the type of physics desired. All events with at least one CMUO data bank go to the inclusive muon output stream. A general muon data filter (GMUFLT) [44] then does a loose selection to try and eliminate background events that look like central muons. The GMUFLT routine makes two loose cuts on all CMUO data banks. The following is a description of the two GMUFLT selection cuts.

- Cut on the match between a CMU stub and a CTC track. The muon must match within 10 cm in the R-ϕ direction.
- A trigger dependent p_T cut on the CMUO track momentum. For the data used in this analysis, the muon track momentum must be at least 2 GeV/c.

Any CMUO data bank passing these two cuts results in the event being written to the inclusive muon output stream. This output stream is called the MUO04 output data stream. Data taken from the 1988-1989 collider run results in ~1000 9-track MUO04 data tapes and ~50 8mm MUO04 data cassettes. Figure 3.2 shows the integrated luminosity supplied by the Tevatron accelerator and the amount written to tape as a function of time. The figure also shows the time at which the Level 2 DIMUON_CENTRAL_3

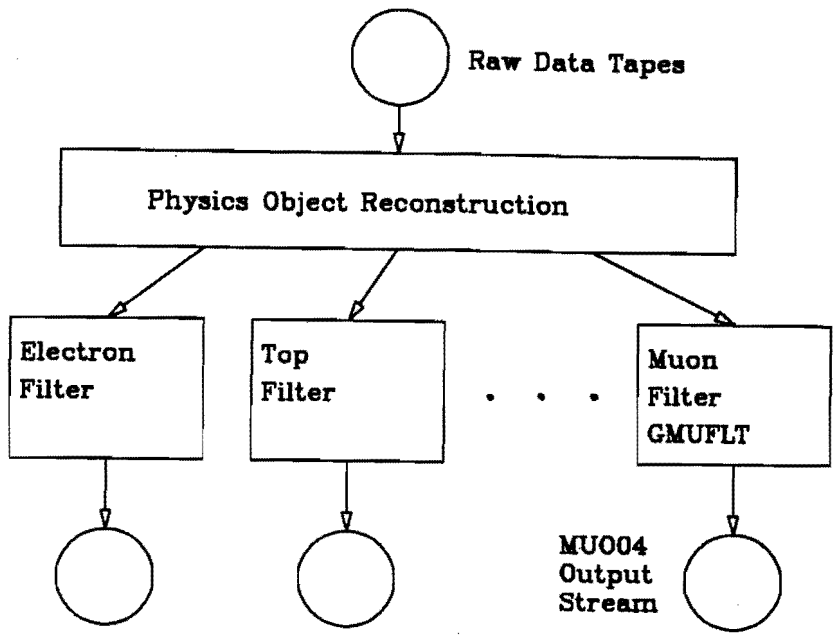

Figure 3.1: V5.1 Production data flowchart.

trigger was installed into the CDF trigger system.

3.2 Extraction of an Inclusive Isolated Dimuon Data Set

A sample of CMUO-CMUO dimuon events, taken during the last run, is selected from the MUO04 V5.1 production stream of the 1988-89 collider run. In order to understand the acceptance of the Drell-Yan events, the Level 2 DIMUON_CENTRAL_3 trigger is used to select events. The CMUO-CMUO data set is therefore required to have at least two CMUO banks and a Level 2 DIMUON_CENTRAL_3 trigger. To insure that a hard $\bar{p}p$ collision occurs, there is also a Level 0 Beam-Beam Counter trigger requirement. This helps to eliminate cosmic-ray triggered events. The integrated luminosity for the data sample passing these trigger requirements is 2.7 $pb^{-1} \pm 7\%$

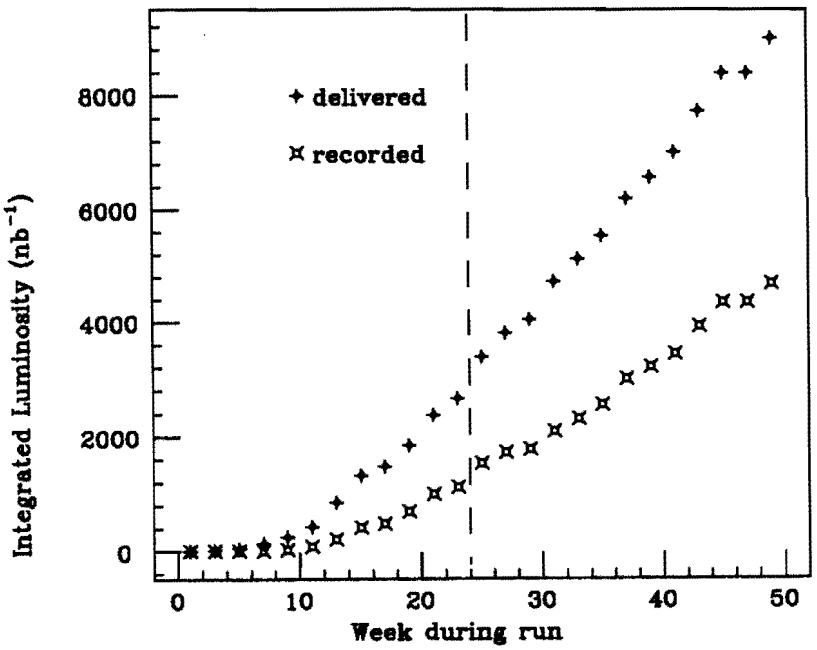

Figure 3.2: Integrated luminosity delivered by the Tevatron and the amount written to tape, for the CDF detector, versus time, for the 1988-89 Fermilab collider run. The dashed line indicates when the Level 2 DIMUON_ CENTRAL_3 trigger was installed.

3.2.1 Sources of Fake Muons

At this point, there have been only very loose cuts imposed on the CMUO-CMUO data set. Many of the events in the sample have CMUO banks that are not muons from a primary $\bar{p}p$ interaction vertex. These can be labeled as fake muons. Other real muons come from non-Drell-Yan sources such as heavy flavor semi-leptonic decays, tau decays, and cosmic rays.

Because of the low number of interaction lengths in the central calorimetry, many QCD jets leak or punch through into the CMU detector chambers, creating a CMU stub. This stub is usually matched to one of the tracks in the jet and forms a CMUO bank that is not due to a real muon. The act of a jet punching through to the muon chamber may take two forms. One is called interactive punch through, in which the particle reaching the muon chambers deposits more energy into the calorimetry than a real muon. This type of false muon is easy to eliminate by requiring that the energy in the calorimetry tower into which the muon candidate traverses has a typical muon minimum ionizing energy. The second type of punch through is called non-interactive punch through. Since there is only five interaction lengths in the central calorimetry, there is approximately a 1 in a 150 chance that a pion or kaon may reach the CMU chamber without interacting with the calorimetry. In this case, a cut on the amount of energy in the calorimetry tower does nothing to remove this fake muon. However, this fake muon is usually in or near a jet and requiring that the muon candidate be isolated removes most of the non-interactive punch through.

A second type of fake muon can occur from a pion or kaon that decays-in-flight into a muon. This produces a real muon but not one from a $\bar{p}p$ interaction vertex. These muons must also be eliminated from the CMUO-CMUO dimuon sample. As with non-interactive punch through, most decay-in-flight muons are near or in a jet. Therefore, isolation of the muon eliminates most decay-in-flight events.

For both non-interactive punch through and decays-in-flight, there are some fake muons that will pass isolation requirements and enter into the isolated dimuon sample.

These remaining fake muons will be accounted for in the chapter on the remaining backgrounds in the Drell-Yan data sample.

3.2.2 Drell-Yan Dimuon Selection Cuts

Drell-Yan events produce fairly well isolated muons, in terms of particles traveling along with the muons. Therefore, very tight isolation cuts are imposed to extract possible Drell-Yan dimuon candidates and eliminate non-Drell-Yan sources of muons. The following set of cuts are imposed on the CMUO-CMUO dimuon sample selected from Level 2 DIMUON_CENTRAL_3 triggers, to generate a data set of highly isolated CMUO-CMUO dimuon pairs with an invariant mass greater than 11 GeV/c^2. These cuts do not remove cosmic ray dimuons from the sample. The cosmic ray background in the dimuon sample in discussed in chapter 5.

a) Global events cuts

- Event has at least two CMUO banks.
- Event has a Level 0 BEAM_BEAM_COUNTER trigger.
- Event has a Level 2 DIMUON_CENTRAL_3 trigger.
- Primary event vertex is between $Z = \pm 60$ cm.

b) Muon track cuts

- Muon ${p^1}_T > 3$ GeV/c and ${p^2}_T > 5$ GeV/c (p_T cut).
- Muon EM tower energy < 2.0 GeV (EM cut).
- Muon HAD tower energy < 6.0 GeV (HAD cut).
- Sum of track p_T in a cone of R=0.5 around the muon, excluding the muon track, < 1.0 GeV/c (Isolation cut).
- Matching between CTC track and muon stub < 10 cm in R-ϕ plane (ΔX cut).
- Muon propagates to good CMU fiducial region defined by FIDCMU [45].

c) Dimuon invariant mass cuts

- Dimuon invariant mass is calculated with non-beam constrained tracks using V5.1 production tracking.
- Invariant mass is greater than 11.0 GeV/c^2.

These cuts produce a set of highly isolated dimuon events that will be used for the Drell-Yan analysis. It is still necessary to account for any remaining background.

3.2.3 Description of Selection Cuts

The set of cuts used to extract the isolated dimuon sample needs to be described. The list of global event cuts are cuts made on the event and not the muons themselves. The Level 0 BEAM_BEAM_COUNTER trigger and the Level 2 DIMUON_CENTRAL_3 trigger have already been described, as well as the definition of a CMUO bank. There is also the requirement that the longitudinal event vertex from which the muons arise must fall within ±60.0 cm of Z=0 in CDF coordinates. Figure 2.2 shows this distribution for J/ψ events. This cut is used to insure that the collision is a good $\bar{p}p$ collision and not a collision with beam gas. The cut also insures that the muons are generated near the center of the detector and pass through good regions of the central tracking chamber and projective calorimetry towers. Figure 3.3 shows the event vertex for events passing the dimuon selection cuts except for the primary vertex cut. The cosmic rays have also been removed from this sample using the cosmic ray removal cuts described in chapter 5. The dashed line indicates the placement of the vertex cut used for this analysis.

The muon track cuts make requirements of each muon to insure isolated dimuon pairs. The requirement that one muon $p_T > 3$ GeV/c while the second muon $p_T > 5$ GeV/c is to follow the same p_T requirements used for the CDF $e - \mu$ data set. This data set is primarily used to study the $B - \bar{B}$ mixing analysis but will be used here to estimate the remaining QCD heavy quark background to the dimuon sample. This is discussed in more detail in chapter 5. Figure 3.4 shows the higher p_T muon versus the

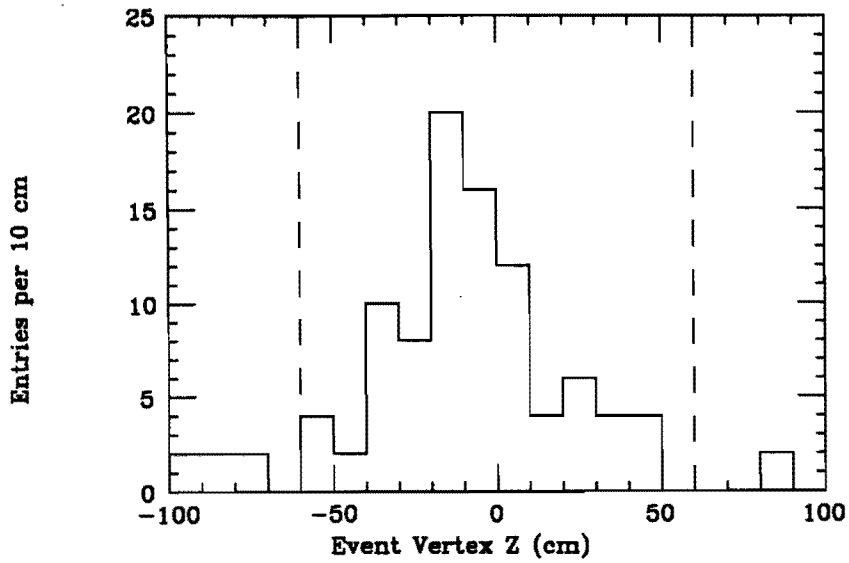

Figure 3.3: Distribution of dimuon event vertex without primary vertex cut. Cosmic rays have been removed.

lower p_T muon for events passing the dimuon selection cuts except for the muon p_T cut. Again, the cosmic rays have been removed from this figure. The dashed line indicates the placement of the p_T cuts used for this analysis.

To insure that the muon track is a minimum ionizing particle, a set of muon tower cuts are imposed. The tower cuts require that the tower electromagnetic calorimetry energy, measured by the CEM, through which the muon passes be < 2.0 GeV while the tower hadronic calorimetry energy, measured by the CHA, be < 6.0 GeV. There is also a matching requirement between the muon CTC track and CMU detector stub be < 10 cm in the R-ϕ plane. As discussed in section 3.1, the GMUFLT production filter already makes this cut on one muon. Requiring it on the second makes the cut symmetric. Figures 3.5, 3.6, and 3.7 show the muon tower electromagnetic energy, hadronic energy, and ΔX matching distributions for events passing the dimuon selection cuts except for the distribution that is plotted. Again, the cosmic rays have been removed from these figures. The dashed lines indicate the placement of the cut used for this analysis.

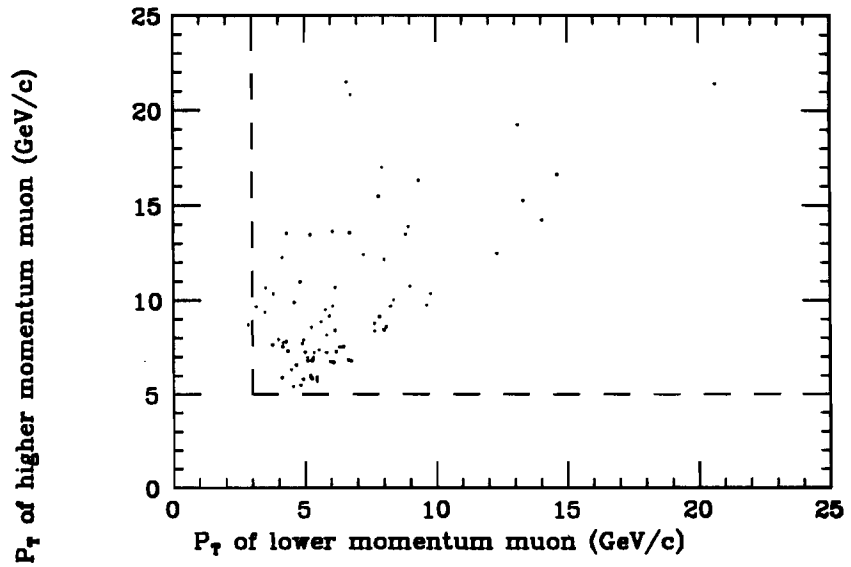

Figure 3.4: Larger muon p_T versus smaller muon p_T passing all dimuon selection cuts except muon p_T cut. Cosmic rays have also been removed.

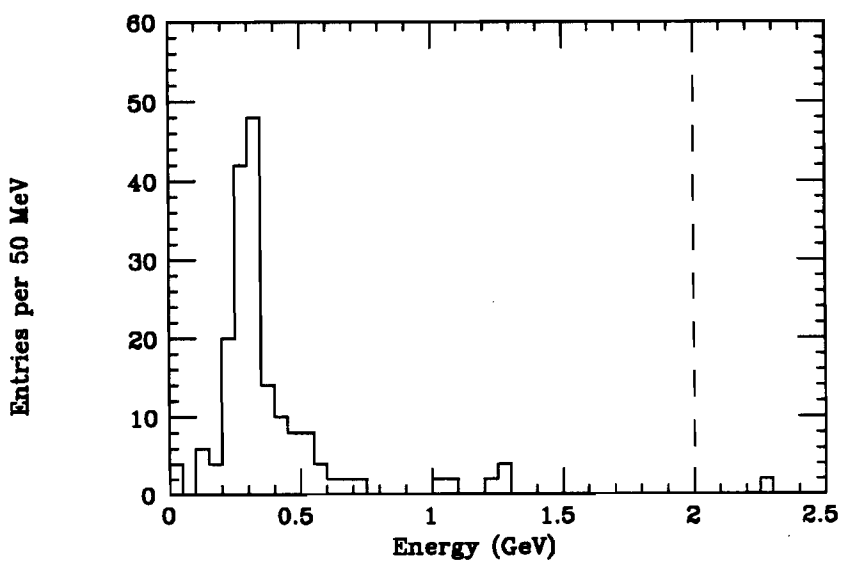

Figure 3.5: Distribution of muon tower electromagnetic energy without electromagnetic energy cut. Cosmic rays have been removed.

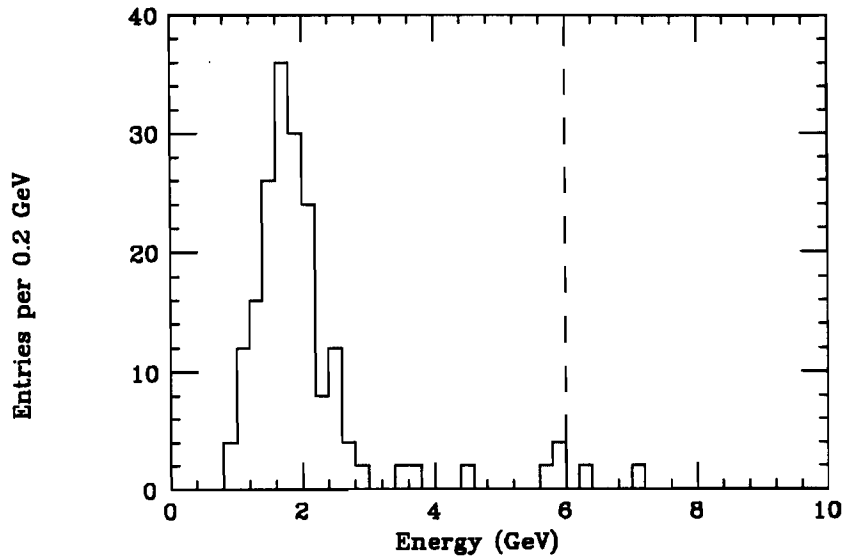

Figure 3.6: Distribution of muon tower hadronic energy without hadronic energy cut. Cosmic rays have been removed.

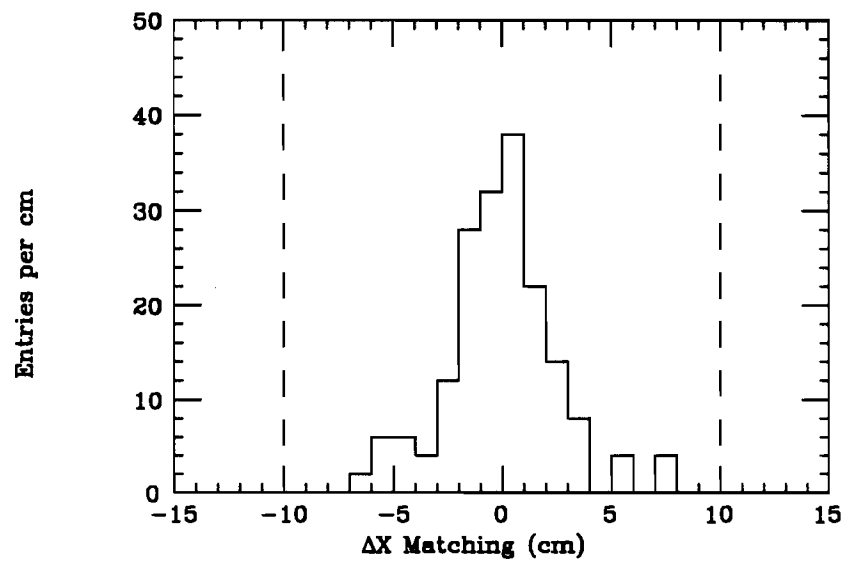

Figure 3.7: Distribution of muon ΔX track matching without ΔX matching cut. Cosmic rays have been removed.

Also, there is a requirement that there be very little energy near the muon tracks, i.e. that they be well isolated. This helps remove fake muons and muons from QCD type activity. This variable Isolation is defined as

$$\text{Isolation} = MAX_{1,2}(\sum_{R=0.5} p_T - p_T^{\mu}) \tag{3.1}$$

where $\sum p_T$ for $R = 0.5$ is the sum of the transverse momentum of tracks in a cone of radius 0.5 in R-ϕ space around the muon, p_T^{μ} is the muon track transverse momentum, and $MAX_{1,2}$ means take the larger of the two muon isolations. Appendix B explains the method used to select the radius in R-ϕ space and the isolation cut of 1.0 GeV/c. Figure 3.8 shows the isolation of opposite-signed events passing the dimuon selection cuts without the isolation cut and having an invariant mass between 11 and 40 GeV/c^2. Cosmic ray events have also been removed. The dashed line indicates the placement of the isolation cut used for this analysis. Figure 5.13 shows the same distribution with same-signed dimuon events.

The response of the CMU detector chambers is not constant over the entire muon chamber. Therefore, good CMU detector fiducial regions need to be defined. Figures A.18 and A.19 show the regions of good fiducial area for a single set of CMU chambers. A subroutine called FIDCMU [45] is used to determine if a CMUO object bank points to a good fiducial region. The routine FIDCMU is discussed in more detail in the following chapter.

The choice of the lower mass limit of 11 GeV/c^2 helps to eliminate two problems of the analysis. First, the mass limit will exclude dimuon events from J/ψ and Υ decays and also to reduce the dimuon background contamination of isolated heavy flavor QCD decays. At lower dimuon invariant masses, the QCD background overwhelms the Drell-Yan signal. Second, the Level 1 central muon trigger efficiency is not fully efficient at lower muon p_T and is also not as well understood as at higher muon p_T. Figure 2.11 shows the Level 1 central muon trigger efficiency versus muon track p_T. A choice of 11 GeV/c^2 mass limit will select higher p_T muons.

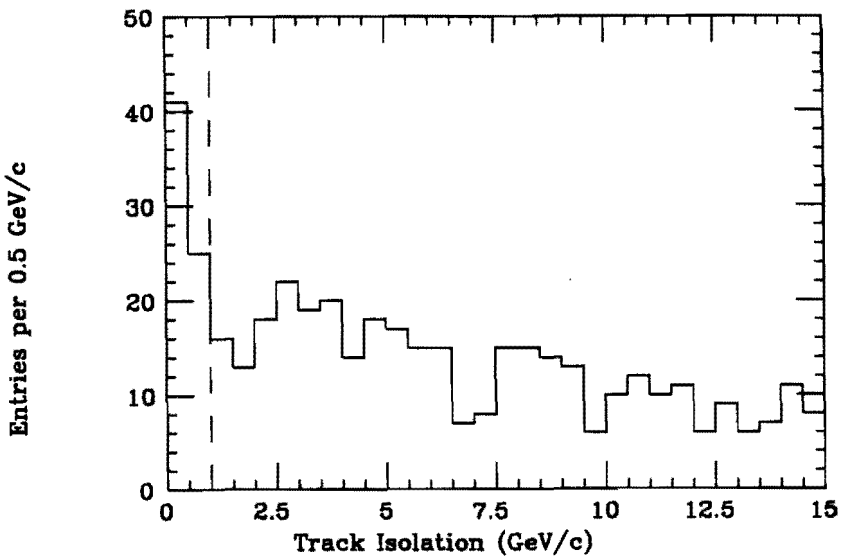

Figure 3.8: Distribution of opposite-signed dimuon isolation without isolation matching cut and having an invariant mass between 11 and 40 GeV/c^2. Cosmic rays have been removed.

Cut	*Efficiency*	*Error*
CMUO Reconstruction	0.97	± 0.02
Primary Vertex Cut	0.95	± 0.01
Track Isolation Cut	0.69	± 0.06
Tower Energy and ΔX Matching Cuts	0.97	± 0.01

Table 3.1: Table of selection cut efficiencies.

3.2.4 Efficiency of Selection Cuts

Table 3.1 list the efficiency of the data selection cuts used to select isolated dimuon events above an invariant mass of 11 GeV/c^2. The Level 2 DIMUON_CENTRAL_3 trigger efficiency is included in the calculation of the acceptance of Drell-Yan events and is discussed in the chapter 4.

The overall cut efficiency $\epsilon_{\text{overall}}$ per event is given by

$$\epsilon_{\text{overall}} = \epsilon^2_{\text{CMUO reconstruction}} * \epsilon_{\text{vertex}} * \epsilon_{\text{isolation}} * \epsilon^2_{\text{tower}} \tag{3.2}$$

The efficiency of the primary $\bar{p}p$ vertex cut is determined from figure 2.2. This shows the primary event vertex for good J/ψ events in the CDF environment.

The efficiency of CMUO reconstruction has two separate components. There is the efficiency of the PRODUCTION_V5_1 central tracking code finding a track that passes through the central tracking chamber. For isolated central rapidity tracks ($-1.0 < \eta < 1.0$), the efficiency for the PRODUCTION_V5_1 tracking code to find the track is 0.99 ± 0.01 [46], independent of the vertex position, polar angle, and event multiplicity. There is also the efficiency for the PRODUCTION_V5_1 central muon code finding a CMU stub. This efficiency is determined by looking at events that fired the Level 2 DIMUON_CENTRAL_3 trigger but did not have any CMUO banks made [47]. Most of

these events are due to cosmic ray that are out of time or else events that are not real muons. A lower bound on the efficiency of CMU stub finding is set at 0.98 ± 0.02 for good muon events.

The efficiency of the CMUO tower cuts is determined from looking at isolated dimuons from J/ψ events. Dimuons from these vector meson decays are not the same mechanism as the Drell-Yan process. Most of the muons coming from J/ψ's are non-isolated. By requiring the muons from these sources be very isolated, one can simulate Drell-Yan muons, at least in terms of the tower into which the muon passes. Appendix A has the description of dimuons from J/ψ events in the CDF environment. Figures A.12 and A.13 show the electromagnetic and hadronic energy deposited in the tower the muon passes. Figure A.15 shows the ΔX matching distance multiplied by the p_T of muon. This shows that

$$< \Delta X >= \frac{15.0\ cm}{p_T} \tag{3.3}$$

From these figures, one can see that the Drell-Yan tower selection cuts are quite loose, for real muons. One finds the tower cut efficiency from the number of isolated J/ψ muons passing these tower selection cuts.

The track isolation cut, for real dimuons from Drell-Yan events, cuts mostly on the energy deposited by the underlying event to the Drell-Yan. The efficiency of the track isolation cut is determined three different ways. First, by taking CMUO-CMUO Z° events, that is, dimuon events that have an invariant mass between 70 and 110 GeV/c^2. and applying the energy tower cuts and the ΔX matching cut, one counts number of events passing the isolation cut. Second, one can take these same Z° events and apply the isolation cuts to both legs to define a good Z° event. One then plots the maximum isolation for two randomly thrown cones of radius 0.5, in $R - \phi$ detector space, taking care that the cones do not overlap the muons in the event. The third method is the same as the second except instead of Z° events one chooses Drell-Yan events. By applying all of the selection cuts (including the cosmic ray removal cuts), one is left with what is assumed to be a sample of good Drell-Yan events. By looking at events with an

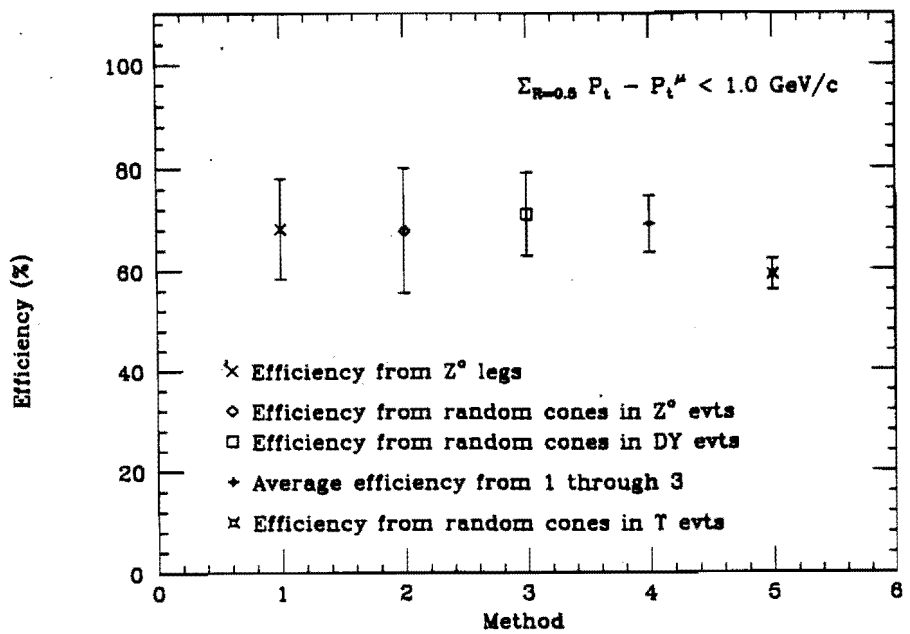

Figure 3.9: Plot of Track Isolation efficiency versus method.

invariant mass greater than 15 GeV/c^2, the contribution from heavy flavor background is removed. Figure 3.9 shows the efficiency of track isolation from these three methods and also shows the combined average.

Figure 3.10 shows the dimuon invariant mass spectrum for events passing the above selection criteria, separated into opposite and same-signed events. The number of same-signed events shows that there is still a non-Drell-Yan contribution to the mass spectrum that needs to be accounted for. There is also a large portion of cosmic-rays present in this sample. Both of these remaining background are discussed in chapter 5.

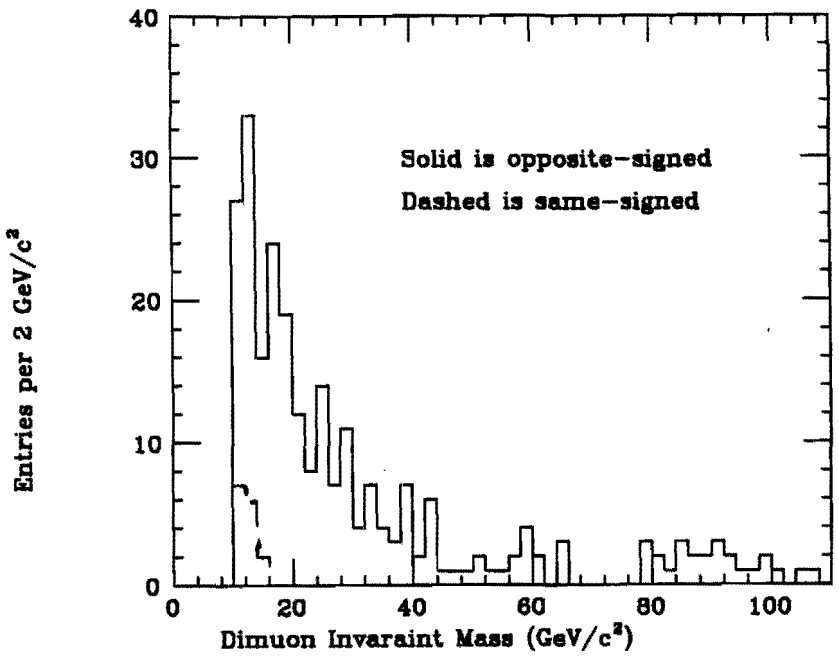

Figure 3.10: Dimuon invariant mass plot for all events passing dimuon selection cuts. Cosmic ray events have not been removed.

Chapter 4

Drell-Yan Monte Carlo Data in the CDF Environment

Monte carlo generation and simulation of Drell-Yan events in the CDF environment satisfies two requirements. First, to determine the Drell-Yan differential cross-section, from CMUO-CMUO dimuon events, requires the calculation of Drell-Yan acceptance for the CDF detector, specifically, the central muon (CMU) chambers. This is determined using monte carlo data and a model of the CMU chambers in the CDF detector environment. Second, the efficiency of various cuts can be measured with monte carlo data. The only requirement is that the monte carlo generation and simulation accurately model the true Drell-Yan physics and correct response of the CDF detector.

4.1 Generaton and Simulation of Monte Carlo Data

The monte carlo generation and simulation are divided into two separate phases. First, a monte carlo is used to generate Drell-Yan dimuon events which closely resembles real $\bar{p}p$ data. The ISAJET monte carlo, V6.25 [48], is used for this purpose. This is called the generation phase and is independent of how one models the CDF detector. Second, the generated monte carlo data is then feed into a model of the CDF detector that simulates

the detector response. A general purpose simulation model of the CDF detector exists [50], but for most of this analysis, it is not necessary to use, since a simple toy detector simulation will suffice.

A modified version of ISAJET V6.25 [49], that incorporates the MRSB parton distribution functions, is used to generate Drell-Yan and Z events . Drell-Yan plus Z^0 events are generated in separate mass regions from 10 GeV/c^2 to 160 GeV/c^2. The allowed p_T range of the virtual photon is set to be 0.1 GeV/c to 100 GeV/c. 50000 events are generated in the mass range of 10 to 15 GeV/c^2, 50000 are generated in the range 15 to 20 GeV/c^2, and then 50000 events are generated for every 10 GeV/c^2 in invariant mass. This is done to generate large numbers of accepted Drell-Yan events over the entire mass range of interest. ISAJET gives a integrated luminosity and total cross-section for each of these mass regions, thus enabling the separate mass regions to be normalized to each other, to give the correct Drell-Yan and Z° mass spectrum.

The generation of ISAJET events does not take into account the CDF detector environment. This is done by simulating all of the necessary components of the CDF detector to make the generated Drell-Yan data look like real $\bar{p}p$ data. The following techniques are used in a toy simulation to accomplish this task.

- Smear the event vertex.
- Smear the muon tracks.
- Model the level 2 DIMUON_CENTRAL_3 trigger and determine if the dimuon event fires the trigger.
- Propagate the muon tracks to the central muon detector and determine if the track points to a good fiducial region.

4.1.1 Vertex Smearing and CDF Detector Simulation

The dimuon events are generated with an event vertex of Z=0.0. To simulate real $\bar{p}p$ data, the generated event vertex is smeared to a gaussian with a mean of 0.0 cm and a

sigma of 30.0 cm. Figure 2.2 shows the smeared gaussian curve, used for monte carlo generated dimuons, compared to real J/ψ data taken from the last run.

For the analysis of CMUO-CMUO data used in the calculation of the differential Drell-Yan cross-section, the tracking code used is the offline production V5.1. The fit to this tracking data is not beam constrained, so therefore the tracking is $\frac{\delta(p_T)}{p_T} = 0.002p_T$. This resolution is used to smear each of the generated Drell-Yan muon tracks.

4.1.2 The Level 2 DIMUON_CENTRAL_3 Trigger Simulation

Since the calculation of Drell-Yan acceptance versus mass integrates over the generated muon momentum and the level 2 DIMUON_CENTRAL_3 trigger is momentum dependent, a model of this trigger must be incorporated into this simulation. Figure 2.11 shows the CMU Level 1 trigger efficiency versus track p_T for a single muon leg, while figure 2.12 shows the CFT bin 0 trigger efficiency versus track p_T for CTC tracks. The convolution of these two plots gives the Level 2 DIMUON_CENTRAL_3 trigger efficiency versus CTC track p_T for each muon leg of the dimuon pair. Figure 4.1 shows this trigger efficiency. The data points are the same in figure 2.11. The band about the data points is the uncertainty of the trigger efficiency for a single muon. The toy simulation of the CDF detector incorporates this trigger efficiency for each muon track.

4.1.3 Central Muon Detector Fiducial Regions

In order to define Drell-Yan muons that simulate real CMUO-CMUO dimuon events, good central muon detector fiducial regions must be defined. After the generation of the Drell-Yan dimuons and smearing of the event vertex, muons are then propagated from the event vertex out to the radius of the central muon detector (CMU) using the analysis routine called FIDCMU [45]. The routine FIDCMU works by taking the muon 3-momentum and smeared event vertex and then bending the muon track through the

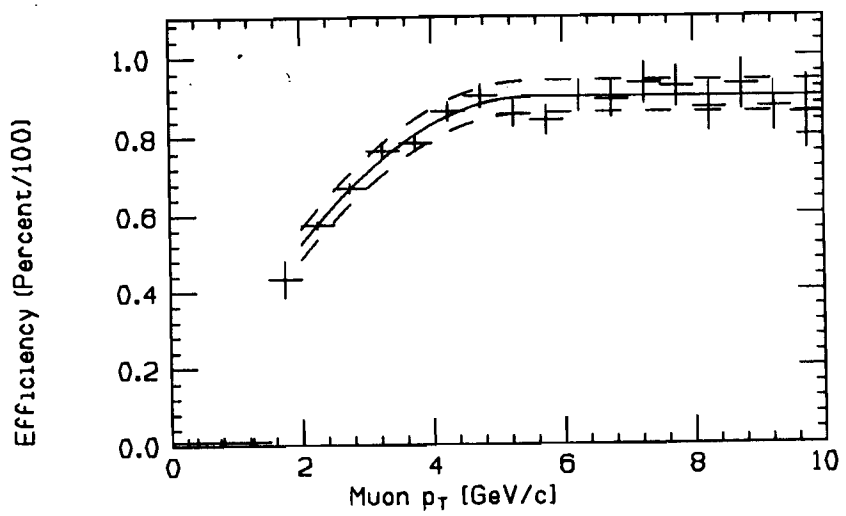

Figure 4.1: Trigger efficiency of one leg of the Level 2 DIMUON_CENTRAL_3 trigger. Curves are upper and lower uncertainty used in monte carlo trigger model.

central magnetic field of the central tracking chamber and return magnetic field present in the central hadronic calorimeter. Once the track reaches the radius of the central muon chambers, it is determined if the muon is within the good fiducial region of the CMU.

Good fiducial regions of the CMU detector are defined by looking at distributions of muons from good J/ψ events. Figures A.18 and A.19 in appendix A show the distribution of η and ϕ for propagated J/ψ muons for all wedges folded into a single wedge coordinate system. The figures also show the actual CMU chamber hits for J/ψ muons. The regions of good fiducial volume are defined by the dashed lines in these figures.

During the data taking run of 1988-89, there was an undetected problem with the central CMU chamber of wedge 2 east. This region is therefore not consisted a good CMU fiducial region and is accounted for in the real data and the monte carlo simulation.

4.2 Comparison of ISAJET Monte Carlo to Real Drell-Yan

In order to use the ISAJET monte carlo along with the toy CDF detector simulation, it must be shown that the generated and simulated Drell-Yan data closely models the real Drell-Yan data. In order to compare monte carlo to real data, an assumption must be made that most of the data passing the selection cuts is Drell-Yan data. Also, the cosmic ray removal cuts discussed in chapter 5 are also used. Figures 4.2 to 4.5 show a comparison of Drell-Yan generated and simulated events, that pass the simulated Level 2 DIMUON_CENTRAL_3 trigger and propagate to good CMU fiducial regions, to real Drell-Yan data. In these plots the solid line is monte carlo and the Drell-Yan dimuon data are the points with statistical error bars. Figure 4.2 shows the generated dimuon parent p_T spectrum normalized to the real data parent p_T spectrum. Figure 4.3 shows the generated dimuon parent rapidity spectrum normalized to the real data parent rapidity spectrum. Figure 4.4 shows the generated muon p_T spectrum normalized to the real data muon p_T spectrum. Figure 4.5 shows the generated muon η distribution normalized to the real data muon η distribution. These figures show that the ISAJET monte carlo models the real Drell-Yan dimuon data in an acceptable manner for calculating the acceptance$\otimes$trigger efficiency.

4.3 Drell-Yan Acceptance and Trigger Efficiency Versus Mass

In order to calculate the Drell-Yan differential cross sections, one must determine the detector acceptance for the physics process of interest. For this analysis, one needs to determine the acceptance of Drell-Yan dimuon events into the CMU portion of the CDF detector versus the dimuon invariant mass. Since the Level 2 DIMUON_CENTRAL_3 trigger is modeled in the detector simulation, the actual measurement is acceptance

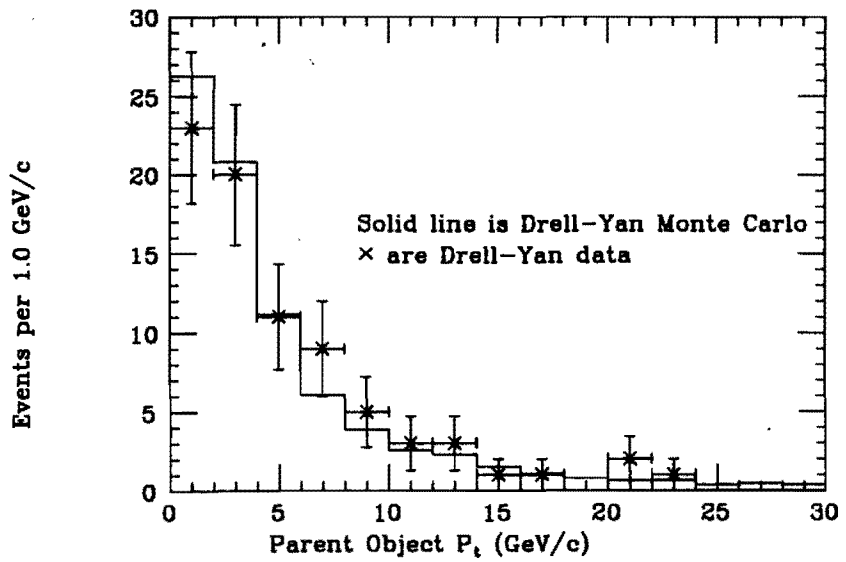

Figure 4.2: Comparison of ISAJET Drell-Yan monte carlo virtual photon transverse momentum distribution normalized to isolated dimuon data.

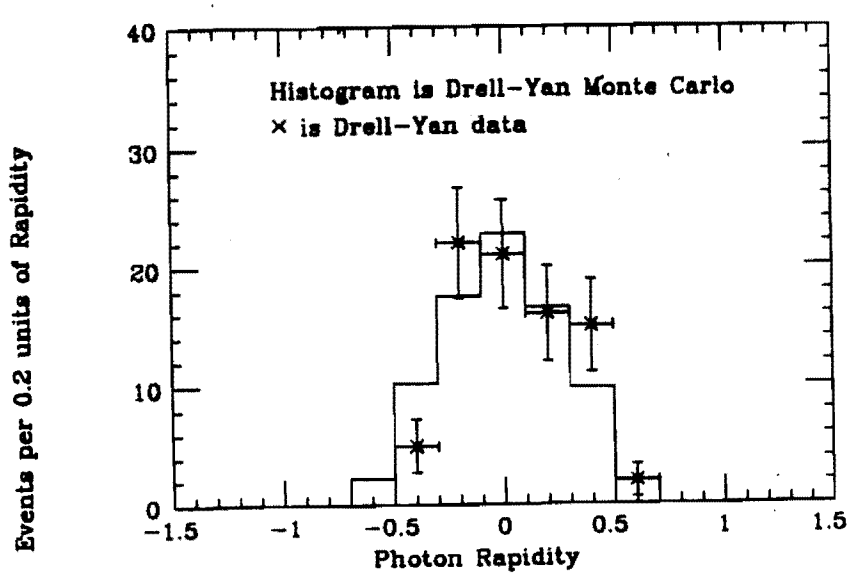

Figure 4.3: Comparison of ISAJET Drell-Yan monte carlo virtual photon rapidity distribution normalized to isolated dimuon data.

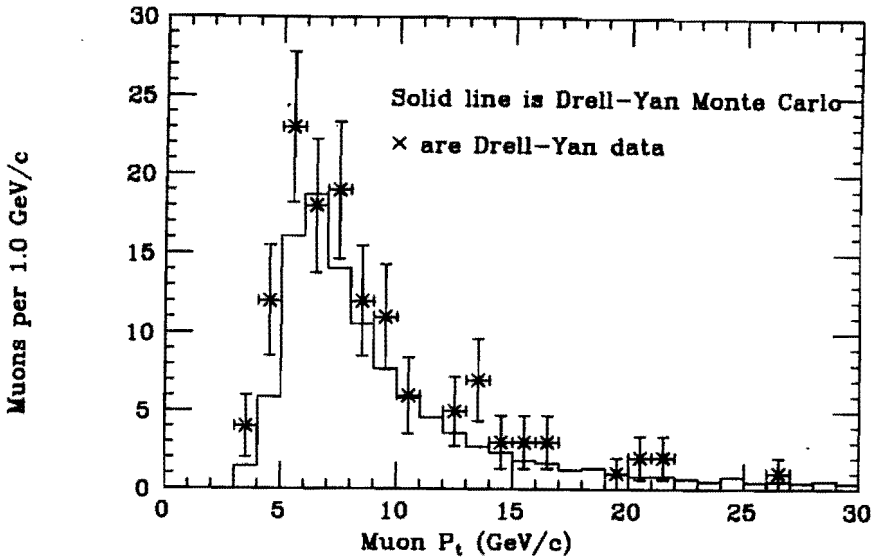

Figure 4.4: Comparison of ISAJET Drell-Yan monte carlo muon transverse momentum distribution normalized to isolated dimuon data.

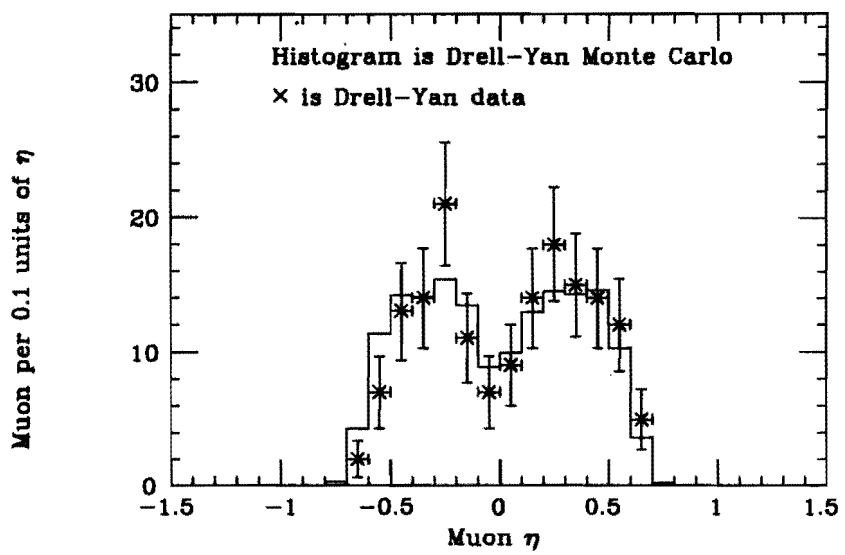

Figure 4.5: Comparison of ISAJET Drell-Yan monte carlo muon track η distribution normalized to isolated dimuon data.

Mass (GeV/c^2)	Accept$\otimes$Trig (Y=0)	Error
11 to 15	0.064	$\pm$0.008
15 to 20	0.069	$\pm$0.007
20 to 30	0.068	$\pm$0.007
30 to 40	0.069	$\pm$0.007
40 to 50	0.065	$\pm$0.007
50 to 60	0.065	$\pm$0.007
60 to 70	0.064	$\pm$0.007
70 to 110	0.068	$\pm$0.007

Table 4.1: Table of Acceptance$\otimes$Trigger efficiency versus Mass for $d^2\sigma/dMdY|_{Y=0}$

convoluted with the trigger efficiency, i.e. acceptance$\otimes$trigger.

For the differential cross section, $d\sigma/dMdY|_{Y=0}$, one defines the acceptance$\otimes$trigger as

$$\text{Acceptance}\bigotimes\text{Trigger(Mass)} = \frac{\text{Number of good fiducial, good trigger events}}{\text{Number of generated events}}\Big|_{Y_\gamma=0} \tag{4.1}$$

where $Y_\gamma = 0$ is defined as the absolute value of the rapidity of the initial virtual photon being less than 1.0. Table 4.1 gives the acceptance$\otimes$trigger, with errors, for each mass region of interest.

4.3.1 Systematic Errors to the Acceptance and Trigger Efficiency

In determining the acceptance*trigger efficiency versus invariant mass, one must account for several systematic uncertainties. Sources of systematic errors occur from the errors on the measurement of the Level 2 DIMUON_CENTRAL_3 trigger, the choice of parton distribution function used in the ISAJET monte carlo, and the uncertainty of the parent

virtual photon transverse momentum. All of these uncertainty have an effect on the acceptance$\otimes$trigger efficiency.

The systematic error due to choice of parton distribution function leads to a 4% uncertainty for the acceptance$\otimes$trigger. This is determined by using different parton distribution functions to calculate the acceptance$\otimes$trigger. The parton distribution functions MRSB, MRSE [12], DO [10], and EHLQ [11] are used for this study. The uncertainty due to the parent virtual photon transverse momentum is determined by perturbing the photon distribution within the data errors in figure 4.2. This gives an uncertainty of 4% for the acceptance$\otimes$trigger. The systematic error due to the trigger is determine by perturbing the model of the trigger used in the simulation within the upper and lower curves of figure 4.1. This results in an 8% error for the acceptance$\otimes$trigger and is independent of mass. The statistical error is determined from the actual number of monte carlo events entering good fiducial regions and passing the trigger model. This is a 2% error for the acceptance$\otimes$trigger. Combining these systematic and statistical errors in quadrature gives an overall error in the acceptance$\otimes$trigger efficiency of 10%.

Chapter 5

Backgrounds in the Drell-Yan Data Sample

The sample of isolated dimuon events, selected with the cuts in chapter 3, still contains a number of events which are not Drell-Yan events. The main sources of the remaining background are from cosmic rays that overlap real physics events and from QCD heavy-quark semi-leptonic decays that appear isolated. This chapter will also discuss the possible background from $\tau \rightarrow \mu\nu$ decays which also appear isolated.

5.1 Cosmic Ray Background

The present sample of CMUO-CMUO dimuon events used to determine the Drell-Yan differential cross-section, has a large background contamination due to cosmic rays. These cosmic ray dimuons have the same calorimetry energy signal as real Drell-Yan events but have different angular distributions. Most of the cosmic ray events have tracks which are back-to-back in 3D in the central tracking chamber (CTC). Drell-Yan dimuon events are generally not back-to-back due to the parent virtual photon p_T and the difference in initial parton p_Z. Also, cosmic rays have no correlation to the beam line in the x-y plane, hence their impact parameter distribution is relatively flat. A

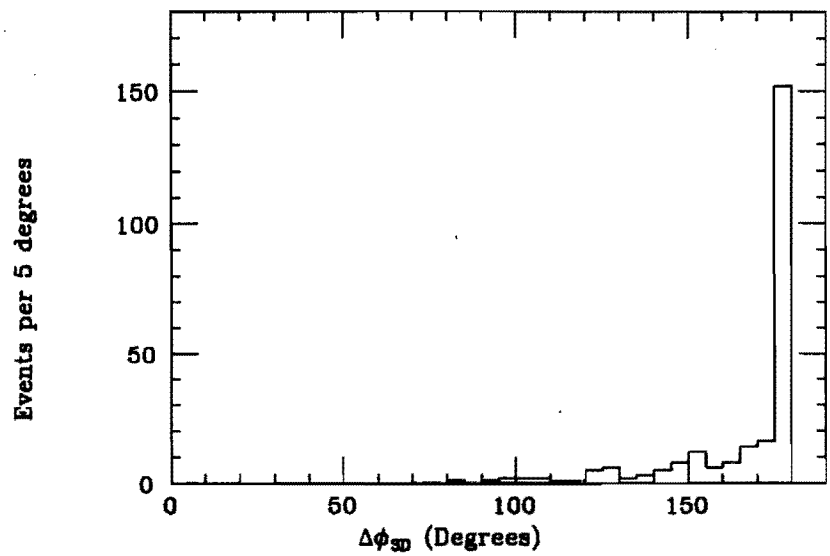

Figure 5.1: Three dimensional opening angle ($\Delta\phi_{3D}$) between opposite-signed dimuons.

combination of a back-to-back opening angle cut and an impact parameter cut is highly efficient in removing cosmic ray dimuon events.

Figure 3.10 shows an invariant mass plot of all CMUO-CMUO events, passing the isolated dimuon selection cuts in chapter 3, for both opposite and same signed dimuons. The three dimensional opening angle ($\Delta\phi_{3D}$), between the opposite-signed dimuons, is shown in figure 5.1. This figure has a pronounced peak at 180° indicating a large cosmic ray background. Figure 5.2 is a plot of $\Delta\phi_{3D}$ versus MAX$|D0|$, for opposite-signed dimuons, where MAX$|D0|$ is the larger of the two CTC track impact parameters ($|D0|$'s). This figure also shows the large number of cosmic rays present in the isolated dimuon data sample. Figure 5.2 also shows the proposed cuts for $\Delta\phi_{3D}$ and $D0$ to remove cosmic ray events.

5.1.1 Impact Parameter Cut Efficiency

Figure 5.2 shows $|\Delta\phi_{3D}|$ versus MAX$|D0|$ for the low mass Drell-Yan sample before cosmic rays are removed. The cut of MAX$|D0| < 0.15$ cm is a good cut for removing many cosmic ray events while keeping Drell-Yan events. The efficiency of this cut can

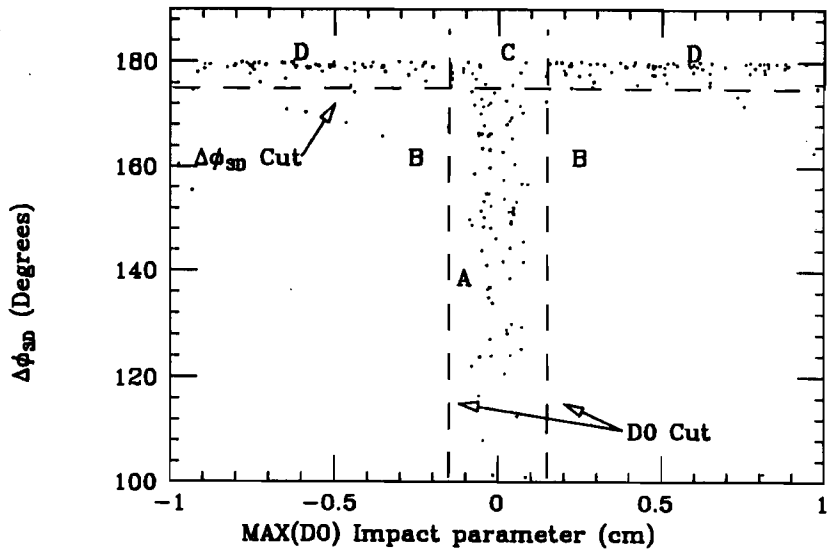

Figure 5.2: $\Delta\phi_{3D}$ versus MAX$|D0|$ for opposite-signed dimuons.

be found by looking at J/ψ and Υ events that pass the global event cuts and muon track cuts described in chapter 3. These cuts insure that the tracks are good muons coming from a good vertex. Appendix A discusses J/ψ and Υ events in the CDF environment. Figure A.16 shows the MAX$|D0|$ for J/ψ events. There are 278 events passing the MAX$|D0| < 0.15$ cm cut out of 281 events, giving an event cut efficiency of 98.9% $\pm$ 0.6. Figure A.17 shows the MAX$|D0|$ for Υ events. There are 240 events passing the MAX$|D0| < 0.15$ cm cut out of 247 events, giving an event cut efficiency of 97.2% $\pm$ 1.1. The combination of J/ψ data and Υ data yields a MAX$|D0| < 0.15$ cm cut efficiency of 98.1% $\pm$ 0.6.

5.1.2 Back-to-Back $\Delta\phi_{3D}$ Cut Description

Figures 5.1 and 5.2 showed the excess of cosmic ray events in the Drell-Yan dimuon sample and their $\Delta\phi_{3D}$ and MAX$|D0|$ distributions. If the MAX$|D0|$ cut is applied to the Drell-Yan dimuon sample, the plot of $\Delta\phi_{3D}$ has its cosmic ray contamination reduced, as is shown in figure 5.3. This can be compared to the plot of $\Delta\phi_{3D}$ in figure 5.1 before MAX$|D0|$ cut. The cosmic ray background still exists, hence the $\Delta\phi_{3D}$ cut is

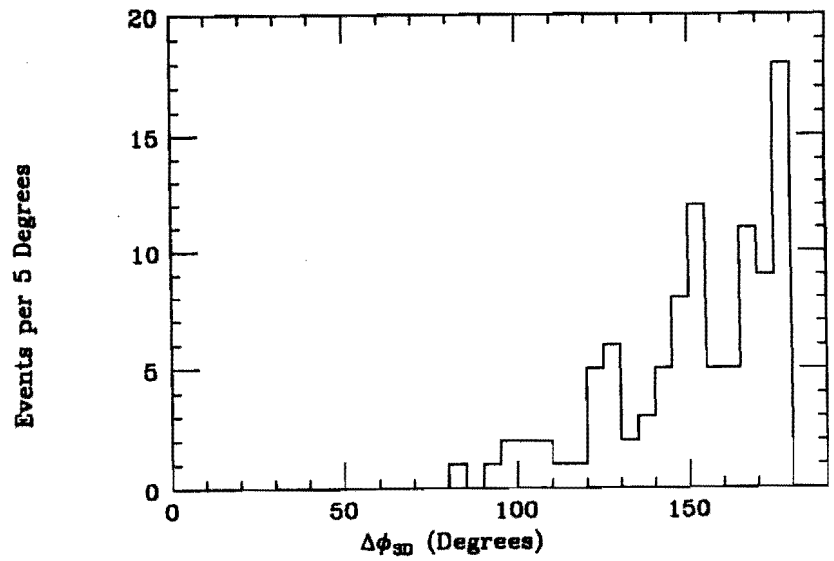

Figure 5.3: Three dimensional opening angle ($\Delta\phi_{3D}$) between opposite-signed dimuons after MAX$|D0|$ cut of 0.15 cm.

still needed. To determine the efficiency of this cut, the Drell-Yan dimuon sample after the MAX$|D0|$ cut is applied will be compared to monte-carlo to determine the number of good Drell-Yan events removed.

Back-to-Back $\Delta\phi_{3D}$ Cut Efficiency

Chapter 4 discussed the generation and simulation of Drell-Yan dimuon events in the CDF environment. Comparisons of monte carlo data to real CDF dimuon data shows that the monte carlo models Drell-Yan dimuon production well. The Drell-Yan monte carlo can now be used to determine the efficiency $\Delta\phi_{3D}$ cut. Figure 5.4 shows the $\Delta\phi_{3D}$ opening angle between the muons taken from monte carlo. It clearly shows that actual Drell-Yan events are almost never back-to-back, so the $\Delta\phi_{3D} < 175°$ should be a very efficient cut.

The $\Delta\phi_{3D}$ cut efficiency can now be determined by comparing the monte carlo $\Delta\phi_{3D}$ opening angle to the Drell-Yan data $\Delta\phi_{3D}$ opening angle. Figure 5.5 show the monte carlo $\Delta\phi_{3D}$ normalized to the Drell-Yan dimuon data with the $\Delta\phi_{3D}$ cut shown. This

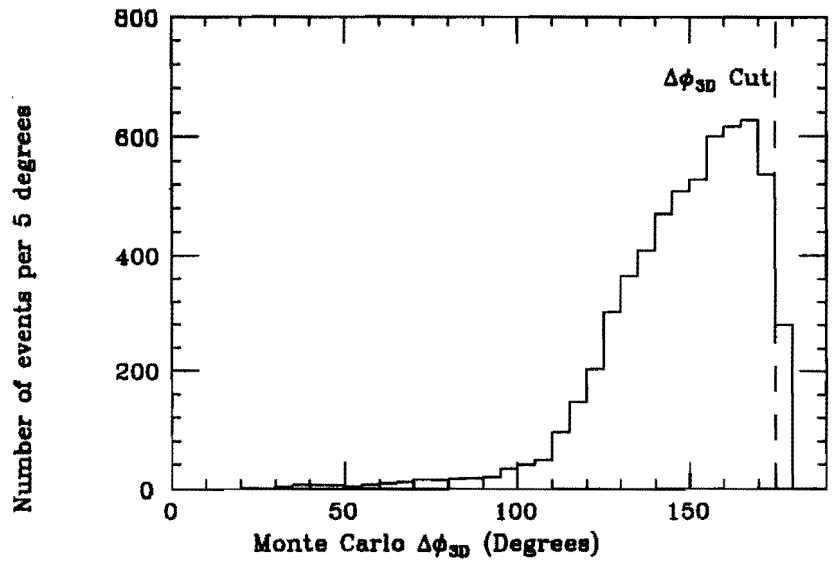

Figure 5.4: Three dimensional opening angle ($\Delta\phi_{3D}$) between opposite-signed dimuons for monte carlo generated Drell-Yan and Z° events.

figure shows that the $\Delta\phi_{3D}$ cut is 97.1% $\pm$ 0.5 efficient.

One can also look at the track impact parameter for events with $\Delta\phi_{3D} > 175°$. From Figure 5.1 and 5.2, a sample of events with $\Delta\phi_{3D} > 175°$ are predominantly cosmic rays and should have a flat MAX$|D0|$ distribution. If there are very many good Drell-Yan events in this sample, they would show up as an excess at max$|D0| \sim 0.0$ cm. Figure 5.6 shows MAX$|D0|$ for $\Delta\phi_{3D} > 175°$ and the plot has no excess at $D0 \sim 0.0$ cm. Therefore, very few Drell-Yan events are cuts by requiring $\Delta\phi_{3D} > 175°$, as concurred by the Drell-Yan Monte Carlo.

5.1.3 Remaining Cosmic Ray Background

Looking at figure 5.2, the remaining background events will have $\Delta\phi_{3D} < 175°$ and MAX$|D0| < 0.15$. This number of events can be found from normalizing this area to the area of $\Delta\phi_{3D} > 175°$ and MAX$|D0| < 0.15$. Referring to the areas marked A,B,C and D on figure 5.2, one can find the remaining number of cosmic in area A from;

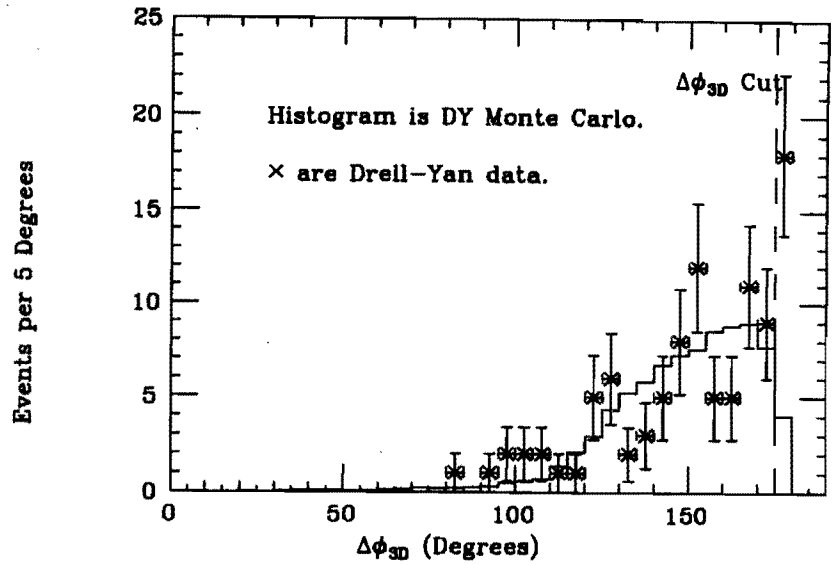

Figure 5.5: Comparison of monte carlo and real data $\Delta\phi_{3D}$ opening angle after impact paramter cut of 0.15 cm.

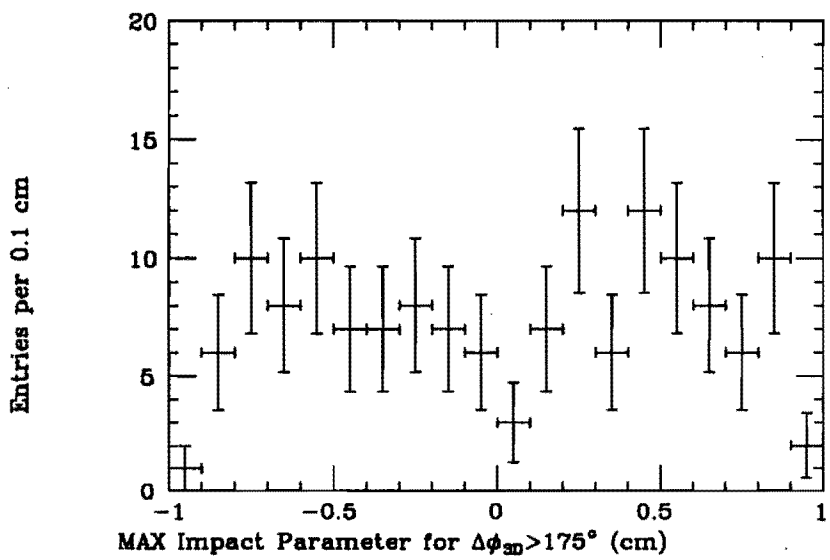

Figure 5.6: Maximum Impact parameter (MAX$|D0|$) for dimuons with $\Delta\phi_{3D} > 175°$.

$$A = B * \frac{C}{D}$$

where

A = number of remaining cosmic rays

B = number of events with $\Delta\phi_{3D} < 175°$ and MAX$|D0| > 0.15$ cm

C = number of events with $\Delta\phi_{3D} > 175°$ and MAX$|D0| < 0.15$ cm

D = number of events with $\Delta\phi_{3D} > 175°$ and MAX$|D0| > 0.15$ cm

Using the numbers from figure 5.2, one gets;

B = 14 events

C = 18 events

D = 134 events

hence,

A = 1.9±0.7 events

This results in 1.9±0.7 remaining cosmic ray events in the 81 remaining events in area A. These remaining events can be distributed over the invariant mass range by using a mass spectrum of known cosmic ray events. Figure 5.7 shows an invariant mass spectrum for cosmic ray dimuon events that appear in the MUO04 data stream. The cosmic events are found by requiring the dimuon pair to fail both cosmic ray cuts, i.e. $|\Delta\phi_{3D}| > 175°$ and MIN$|D0| > 0.15$ cm.

The cuts of $|\Delta\phi_{3D}| < 175°$ and MAX$|D0| < 0.15$ cm remove most of the dimuon cosmic ray background events while retaining almost all of the Drell-Yan signal. Figure 3.10 showed the dimuon Drell-Yan signal before cosmic rays were removed. Figure 5.8 now show the dimuon events from figure 3.10 that pass these two cosmic ray cuts.

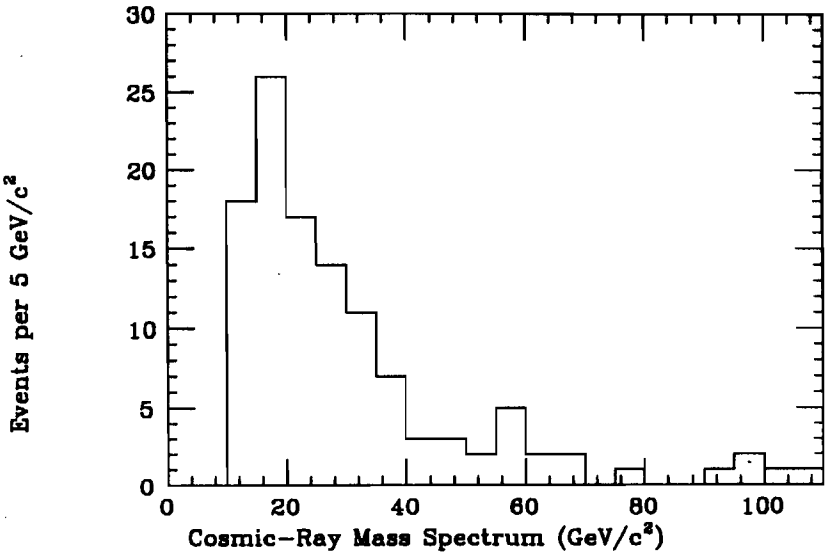

Figure 5.7: Dimuon invariant mass spectrum of real cosmic ray events taken from the MUO04 data stream.

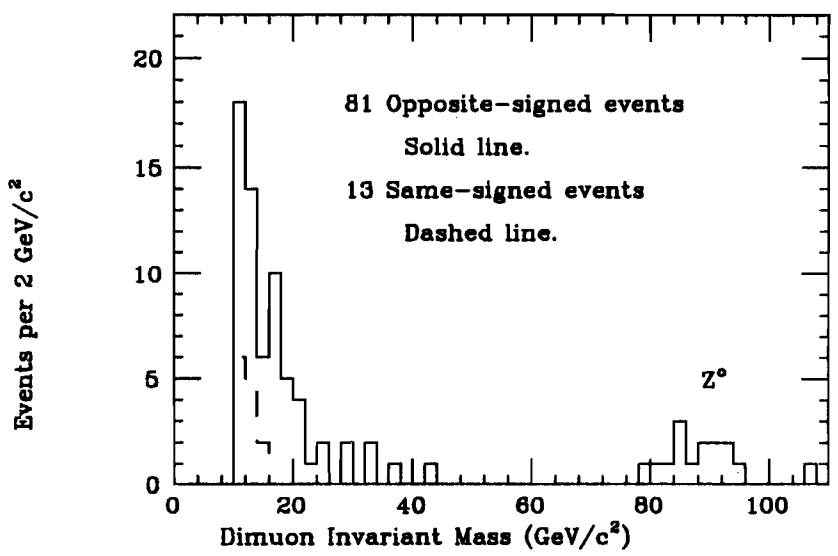

Figure 5.8: Dimuon invariant mass with cosmic rays removed.

5.2 τ Background

The dominant source of τ's into dimuons is from Drell-Yan to $\tau^+\tau^-$ and Z° to $\tau^+\tau^-$ in which the τ's decay into muons. Since both muons would be fairly isolated, the event would look just like a Drell-Yan event. All other combinations of a single $\tau \rightarrow \mu$ plus an isolated muon from some other source are assumed to be very small and are not considered. This $\tau^+\tau^-$ to $\mu^+\mu^-$ background should also be small since the branching ratio is only 3% and the muons must pass all of the fiducial and trigger selection criteria.

An estimate of this background can be made by using ISAJET [48] monte carlo to generate $Z^\circ \rightarrow \tau^+\tau^-$ and $DY \rightarrow \tau^+\tau^-$ events and determine how many pass the selection cuts. Since τ's decay into $\mu\overline{\nu}_\mu\nu_\tau$, for this estimate, it is assumed that these muons would pass all of the isolation and matching selection cuts. It remains to be determined how many dimuons from $\tau^+\tau^-$ would enter good muon fiducial regions and also trigger the level 2 DIMUON_CENTRAL_3 trigger. ISAJET is used to generate 42.0 pb^{-1} of Drell-Yan and Z° to $\tau^+\tau^-$ events having an invariant mass between 9 GeV and 125 GeV. Figure 5.9 shows the di-τ invariant mass generated by ISAJET. Of these di-τ events, 3.2% decay into dimuons. Figure 5.10 shows the dimuon invariant mass of muons coming from τ's while figure 5.11 shows their P_t. As one can see from figure 5.11, most of the muons from τ decays are at low P_t. The dimuons are run through the same acceptance/trigger efficiency program used to determine the Drell-Yan acceptance and trigger efficiency. Because of the low muon P_t spectrum and the small fiducial acceptance of the central muon chambers, few dimuons from di-τ's pass all the Drell-Yan selection criteria. Figure 5.12 shows the dimuon invariant mass spectrum from di-τ's for 42.0 pb^{-1} of ISAJET monte carlo. For 2.7 pb^{-1} of real dimuon data, one would expect 0.8 events from $\tau^+\tau^-$ decays for the mass range of 11 to 110 GeV in invariant mass.

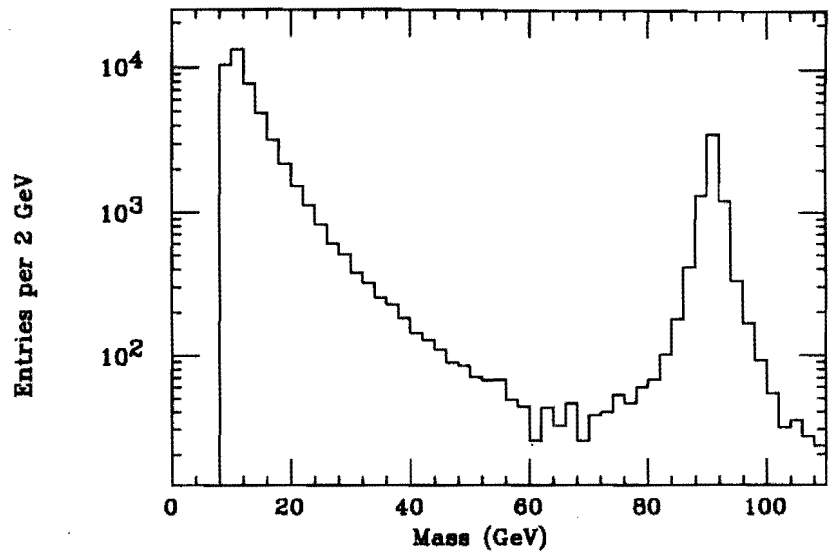

Figure 5.9: Di-τ invariant mass spectrum from 42.0 pb^{-1} of ISAJET monte carlo.

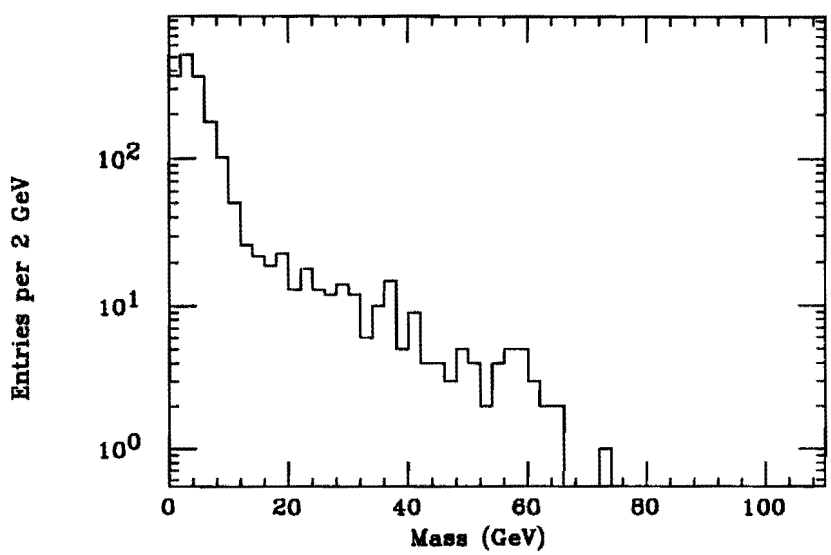

Figure 5.10: Dimuon invariant mass spectrum from τ decays.

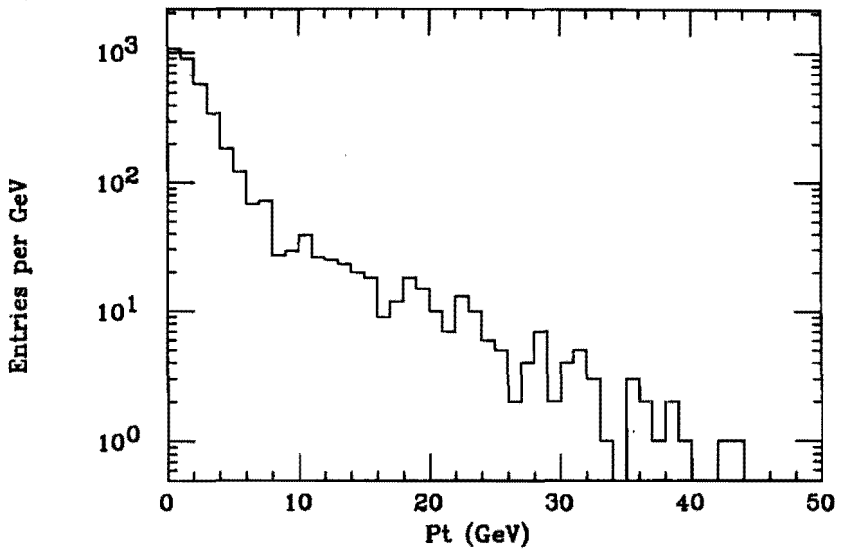

Figure 5.11: Muon p_T spectrum from τ dimuons.

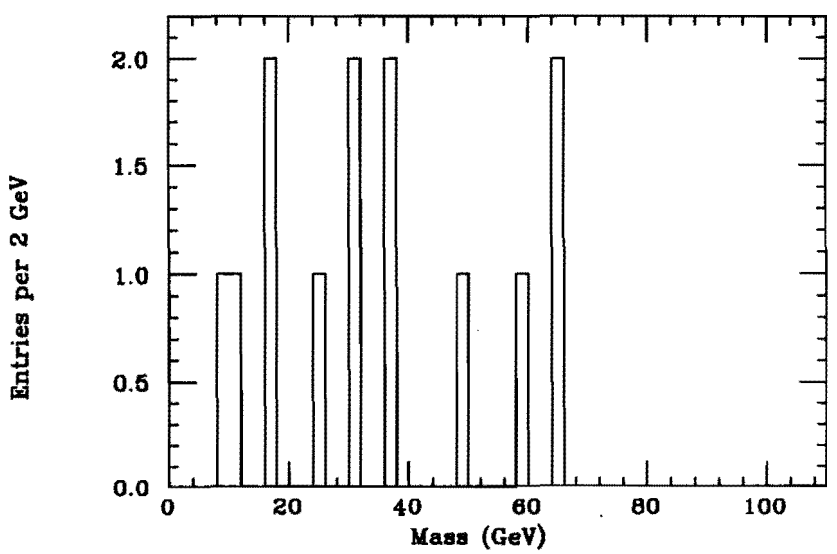

Figure 5.12: Dimuon invariant mass spectrum from τ decays passing fiducial and trigger requirements.

5.3 QCD Background

The background from QCD events that appear isolated falls into two different categories. First, there are the isolated dimuons in which the charge of the individual muon legs are uncorrelated to each other. These are mostly non-interactive punch through events and decays-in-flight. The number of opposite-signed dimuon events to the number of same-signed dimuon events are roughly the same as a function of mass. These type of background dimuon events are labeled as symmetric QCD events.

There are also isolated dimuon events occurring from heavy quark decays, mostly from $B - \bar{B}$. For $B - \bar{B}$ events, the dimuons appear as opposite-signed dimuons, excluding mixing and secondary decays. Even with mixing and secondary decays, there are still more opposite-signed dimuons appearing from $B - \bar{B}$ decays than there are same-signed events.

5.3.1 Symmetric QCD Background

The remaining same-signed events in figure 5.8 show that there is still a non-Drell-Yan background. For non-correlated dimuons, there should be as many same-signed background events as opposite-signed background events. One can account for this symmetric background by subtracting the same-signed mass spectrum from the opposite-signed mass spectrum. Figure 5.13 shows the track isolation for opposite-signed and same-signed dimuons that pass all of the selection cuts of chapter 3, except the track isolation cut, and also pass the cosmic ray cuts presented above. The figure shows the excess of isolated opposite-signed events at low isolation. These are the Drell-Yan events present in the same. The same-signed events appearing at low isolation are due to the remaining symmetric background. Figure 5.14 now shows the dimuon invariant mass spectrum with the same-signed spectrum subtracted.

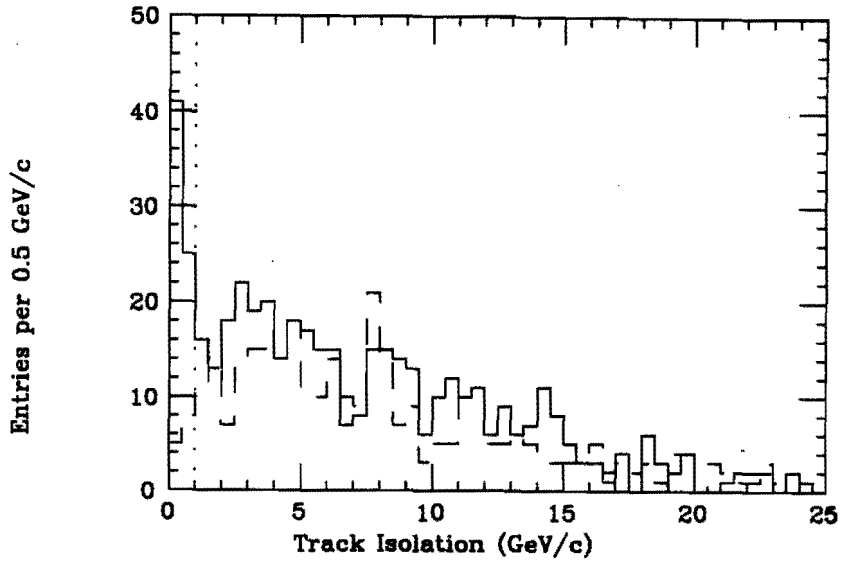

Figure 5.13: Dimuon track isolation for events passing all selection cuts, except track isolation, and also cosmic ray removal cuts.

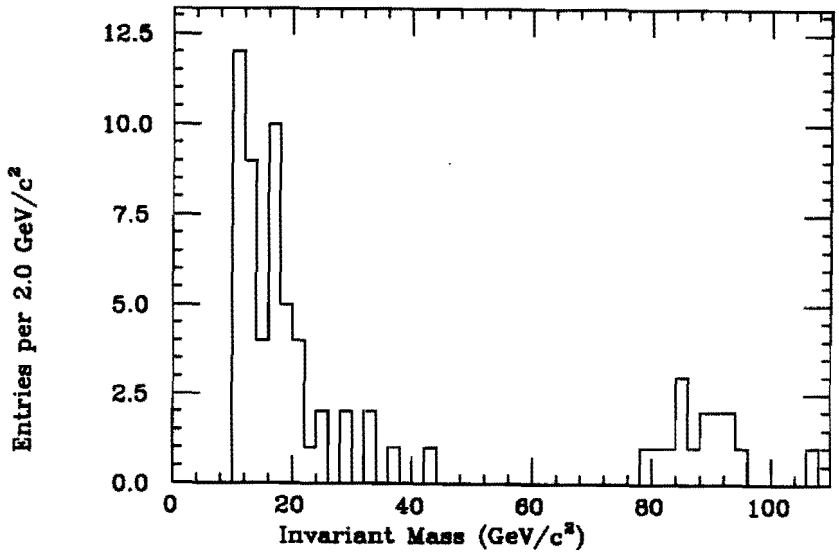

Figure 5.14: Dimuon invariant mass spectrum with same-signed mass spectrum subtracted.

5.3.2 Non-Symmetric QCD Background

The background from isolated $B - \bar{B}$ decays contributes mostly to the opposite-signed dimuon spectrum. These events can not be accounted for by subtracting the same-signed spectrum. The background from isolated $B - \bar{B}$ dimuons is determined by studying electron-muon events found by the CDF detector. These electron-muon events have the unique signature that indicates that they come from heavy flavor decays.

One can use the equations

$$N_< = N_s * \epsilon_{\text{isolation}} + N_b * f \tag{5.1}$$

$$N_> = N_s * (1 - \epsilon_{\text{isolation}}) + N_b * (1 - f) \tag{5.2}$$

where

$$\begin{aligned}
N_< &= \text{Number of events less than isolation cut.} \\
N_> &= \text{Number of events greater than isolation cut.} \\
\epsilon_{\text{isolation}} &= \text{Efficiency of track isolation cut.} \\
f &= \text{Fraction of heavy quark decays passing isolation cuts.} \\
N_s &= \text{Totalnumber of Drell} - \text{Yan events.} \\
N_b &= \text{Total number of Non} - \text{symmetric QCD events.}
\end{aligned}$$

By redefining N_s to be the total number of Drell-Yan events passing the track isolation cut and N_b to be the total number of non-symmetric QCD events passing the track isolation cut, then these equations become

$$N_< = N_s + N_b \tag{5.3}$$

$$N_> = N_s * \frac{1 - \epsilon_{\text{isolation}}}{\epsilon_{\text{isolation}}} + N_b * \frac{1 - f}{f} \tag{5.4}$$

The value for $\epsilon_{\text{isolation}}$ is known from chapter 3. The value of f is determined from the electron-muon data sample.

The electron-muon data sample is taken from the inclusive muon output data steam (MUO04) [51]. This sample can be used to determine what fraction of dimuons from

Sample	Fraction passing cuts (%)
electron-muon data	11.5 ± 3.4
electron-muon monte carlo	10.0 ± 3.4
electron-electron monte carlo	8.8 ± 3.8
muon-muon monte carlo	7.9 ± 4.4

Table 5.1: Fraction of $B - \bar{B}$ lepton pair decays passing all selection cuts.

$B - \bar{B}$ decays pass all of the isolated dimuon selection cuts. From the electron-muon data sample, one finds that $11.5 \pm 3.4\%$ of the events pass all of the selection cuts if one makes the assumption that the electron track is a muon track. Since electrons have reconstruction requirements which are different from muons, one can not blindly take electrons and treat them like a muon. A sample of generated and simulated $B - \bar{B}$ monte carlo events that decay into electron-muon pairs as well as muon-muon and electron-electron pairs is used to determine the fraction of $B - \bar{B}$ events that pass the selection cuts. Table 5.1 [52] gives a list of the fraction of $B - \bar{B}$ events passing the selection cuts for electron-muon, muon-muon, and electron-electron events. Because the real electron-muon data agrees well with the monte carlo electron-muon results, one can believe the monte carlo muon-muon and electron-electron results. For the muon-muon data, a value of f = 8.0±5.0 is chosen.

Equations 5.3 and 5.4 are solved for N_s and N_b. The values of f and $\epsilon_{\text{isolation}}$ are now known. The values for $N_<$ and $N_>$ are taken from figure 5.15. Figure 5.15 is the opposite-signed isolation spectrum minus same-signed isolation spectrum of figure5.13.

$$N_< = 53 \pm 8.9 \text{ events}$$

$$N_> = 83 \pm 27.0 \text{ events}$$

This gives N_b to be

$$N_b = 8.2 \pm 3.8 \text{ events}$$

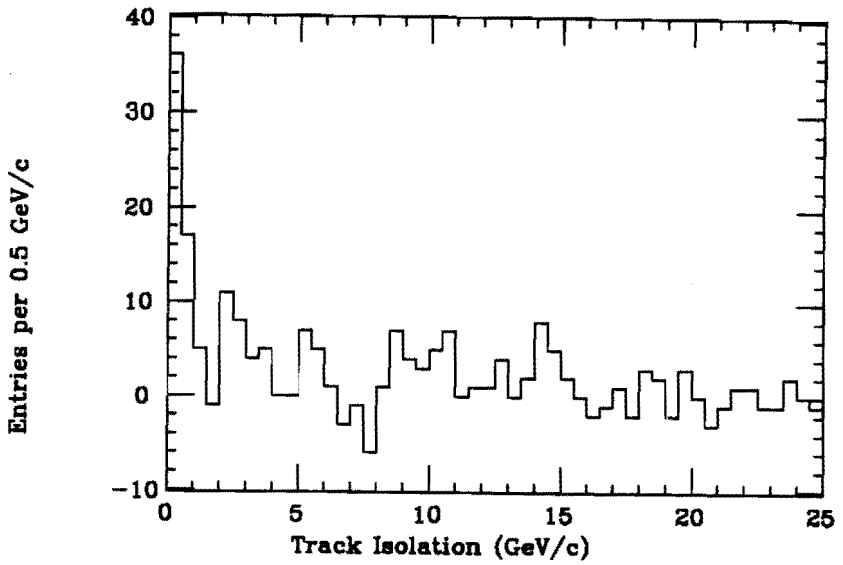

Figure 5.15: Opposite-signed dimuon isolation spectrum minus same-signed dimuon isolation spectrum.

5.4 Total Remaining Background

The total remaining background from cosmic rays, τ decays, and non-symmetric QCD background is divided into the mass bins of interest. The remaining number of cosmic rays are divided into mass bins by using the cosmic ray mass spectrum in figure 5.7. Since there are only 0.8 τ background events predicted to be in the isolated dimuon sample, the background for τ events will be assumed to be zero. The remaining number of non-symmetric background events are divided using a spectrum a non-isolated dimuon spectrum. Figure 5.16 is a invariant mass spectrum of non-isolated dimuon events. This is used to normalize the remaining non-symmetric background into mass bins. Table 5.2 shows the remaining background from each source as a function of mass.

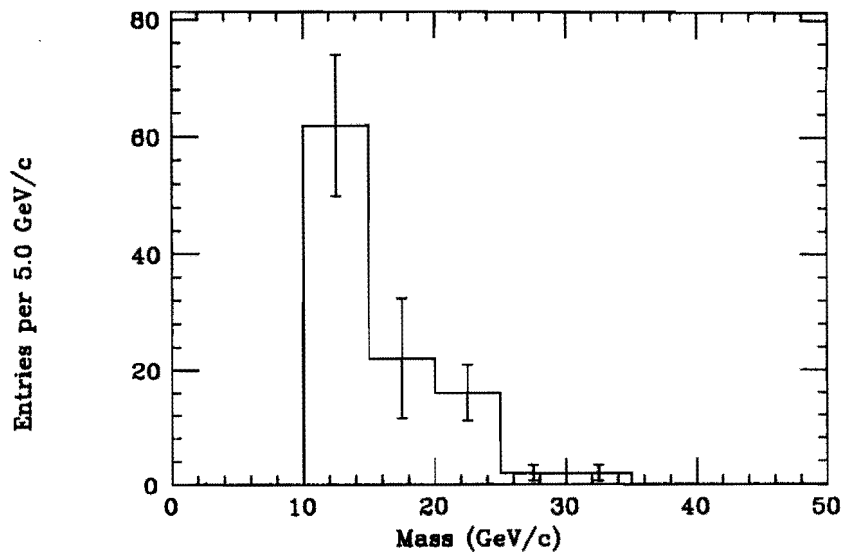

Figure 5.16: Opposite-signed minus same-signed dimuon invariant mass spectrum for non-isolated events.

Mass Bin (GeV/c^2)	Cosmic Rays	Non-Symmetric QCD	Total Background
11-15	0.41±0.17	3.5±1.8	3.9±1.8
15-20	0.31±0.13	2.3±1.1	2.6±1.1
20-30	0.39±0.16	1.9±0.8	2.3±0.8
30-40	0.29±0.13	0.4±0.2	0.7±0.2
40-50	0.10±0.05	0.0	0.10±0.05
50-60	0.10±0.05	0.0	0.10±0.05
60-70	0.03±0.03	0.0	0.03±0.03
70-110	0.10±0.05	0.0	0.10±0.05

Table 5.2: Remaining background from cosmic rays and symmetric QCD heavy quark decays for each mass bin of interest.

Chapter 6

Calculation of Drell-Yan Differential Cross Sections and Conclusion

6.1 Differential Cross Section Calculation

The calculation of $d^2\sigma/dMdY|_{Y=0}$ now can be found from the following.

$$\frac{d\sigma}{dMdY}|_{Y=0} = \frac{\#\text{Events}}{\text{Lum} * \text{Accept} \bigotimes \text{Trig}(\text{M}, \text{Y} = 0) * \epsilon_{\text{overall}} * \Delta\text{M} * \Delta\text{Y}} \tag{6.1}$$

where

Events	=	# opposite-signed dimuons minus same-signed dimuons minus opposite-signed background
Lum	=	Integrated luminosity for the Level 2 DIMUON_CENTRAL_3 trigger
Accept $\bigotimes$ Trig(M, Y = 0)	=	Acceptance convoluted with the Trigger efficiency as a function of mass where the virtual photon has a

Mass range (GeV/c^2)	# Opposite-same signed events
11 to 15	23 ± 6.9
15 to 20	19 ± 4.4
20 to 30	9 ± 3.0
30 to 40	3 ± 1.7
40 to 50	1
50 to 60	0
60 to 70	0
70 to 110	15 ± 3.9

Table 6.1: Table of number of opposite-signed dimuon minus same-signed dimuons for each mass bin.

$$\begin{aligned} & \text{rapidity of } -1.0 < Y < 1.0 \\ \epsilon_{\text{overall}} &= \text{Overall efficiency for all cuts} \\ \Delta M &= \text{Width of mass bin for cross section} \\ \Delta Y &= \text{Width of virtual photon rapidity region} \end{aligned}$$

The luminosity, $\epsilon_{\text{overall}}$, and ΔY are

$$\begin{aligned} \text{luminosity} &= 2.77\text{pb}^{-1} \pm 7\% \\ \epsilon_{\text{overall}} &= 0.56 \pm 0.06 \\ \Delta Y &= 2.0 \end{aligned}$$

Table 6.1 gives the number of raw number of opposite-signed dimuon events minus the number of same-signed dimuon events for each mass bin. The number are taken from figure 5.14. Because of the poor statistics, the differential cross section is calculated for the mass range 11.0 to 40.0 GeV/c^2 and for the Z° mass region 70.0 to 110.0 GeV/c^2.

Table 6.2 gives the number of events with background subtracted, Acceptance*trigger efficiency, ΔM, and Drell-Yan weighted average mass, for the mass bins of interest.

Mass range (GeV/c^2)	# events	Accept*trig	ΔM	$< M >$
11 to 15	19.1±7.1	0.064±0.008	4.0	12.66
15 to 20	16.4±4.5	0.069±0.007	5.0	17.13
20 to 30	6.7±3.1	0.068±0.007	10.0	23.85
30 to 40	2.3±1.7	0.069±0.007	10.0	34.13
70 to 110	14.9±3.9	0.068±0.007	40.0	90.93

Table 6.2: Table of number of events, acceptance*trigger efficiency, ΔM, and Drell-Yan weighted average mass used to calculate the differential cross section.

used to calculate $d^2\sigma/dMdY|_{Y=0}$. Table 6.3 tabulates the differential cross sections $d^2\sigma/dMdY|_{Y=0}$ and $M^3d^2\sigma/dMdY|_{Y=0}$ using equation 6.1. The statistical and systematic errors are separated to show their relative size to the differential cross section. The error for $M^3d^2\sigma/dMdY|_{Y=0}$ is just the combined statistical and systematic error. The width of the virtual photon rapidity (ΔY) is 2.0.

The measured values of $M^3d^2\sigma/dMdY|_{Y=0}$ are averaged to give one number and is plotted with previous experimental values in figure 1.4. The result is labeled CDF in figure 1.4 and shows no significant deviation from the scaling predicted. Figure 6.1 shows the measured values of $M^3d^2\sigma/dMdY|_{Y=0}$ plotted with a next-to-leading order theoretical prediction [54] using several versions of Martin-Roberts-Stirling and Morfin-Tung parton distribution functions. The predicted cross section at small invariant mass shows a strong dependance on the choice of parton distribution functions.

The total cross section for $Z^\circ \rightarrow \mu^+\mu^-$, for the mass region 70 to 110 GeV/c^2. is found to be

$$\sigma(Z^\circ \rightarrow \mu^+\mu^-) \;=\; 246.3 \pm 64.5 \pm 40.0 \text{ pb}$$

This agrees within errors with the $Z^\circ \rightarrow e^+e^-$ cross section measurement made at CDF

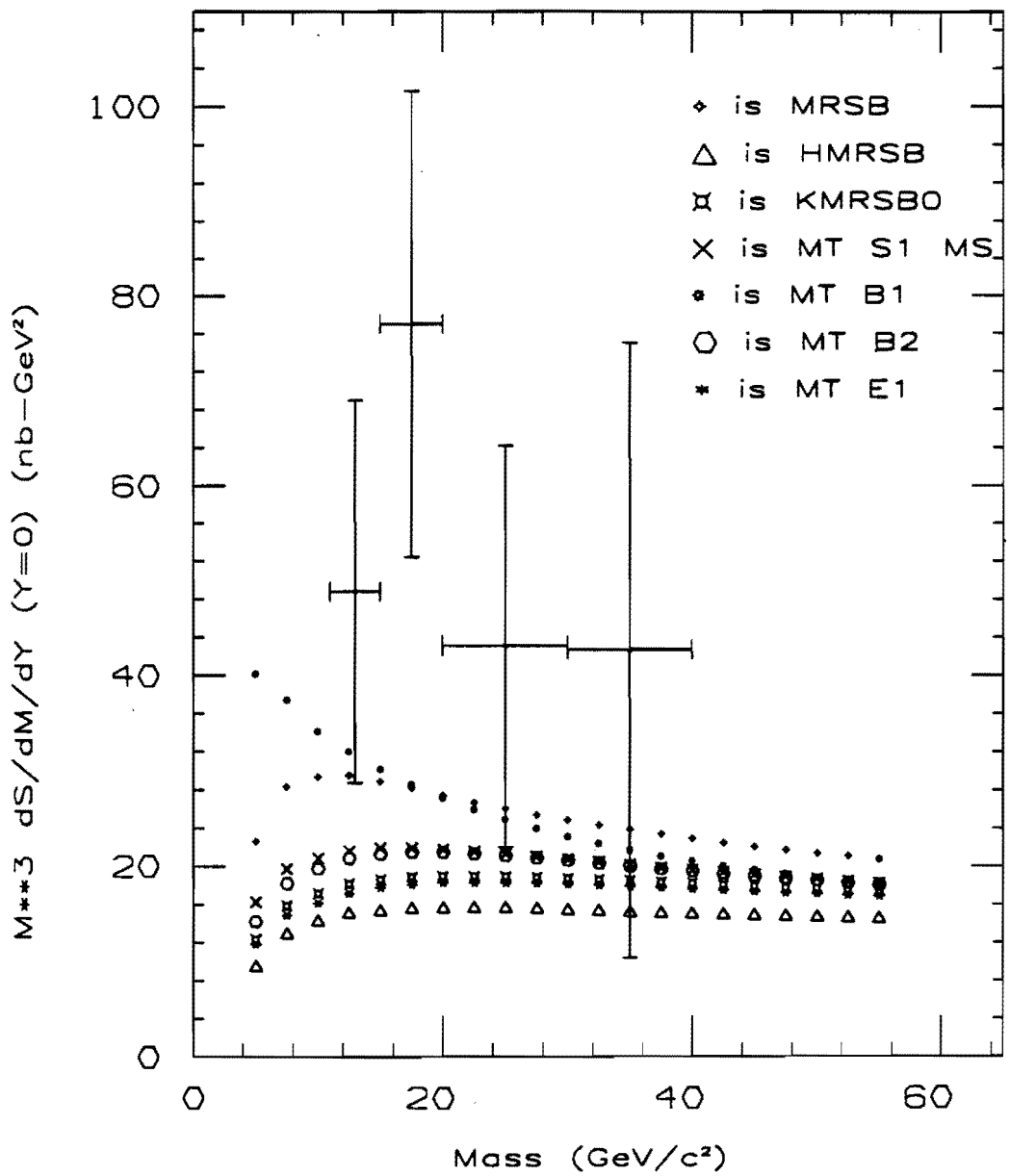

Figure 6.1: Calculated values of $M^3 d^2\sigma/dMdY|_{Y=0}$ compared to next-to-leading order predicted values.

Mass range (GeV/c^2)	$d^2\sigma/dMdY$ (pb/GeV/c^2)	Stat Error	Sys Error	$M^3d^2\sigma/dMdY$ ($(GeV/c^2)^2nb$)	Total Error
11 to 15	24.0	8.9	4.3	48.8	20.1
15 to 20	15.3	4.2	2.5	77.0	24.6
20 to 30	3.2	1.5	0.5	43.1	21.1
30 to 40	1.1	0.8	0.14	42.7	32.3
70 to 110	1.77	0.46	0.29	1328.0	410.2

Table 6.3: Differential cross sections $d^2\sigma/dMdY|_{Y=0}$ and $M^3d^2\sigma/dMdY|_{Y=0}$ from dimuon events.

[53] of

$$\sigma(Z^\circ \rightarrow e^+e^-) \;=\; 209.0 \pm 13.0 \pm 17.0 \text{ pb}$$

6.2 Drell-Yan Analysis for Future Collider Runs

During the years 1992 through 1993, the Fermilab Tevatron will have another collider run. For the CDF collaboration, there will be two major improvements from the 1988-89 collider run.

First, the integrated luminosity delivered by the accelerator will be approximately 25 pb^{-1}. During the last run, the accelerator delivered approximately 10 pb^{-1}, of which less than half was written to tape. This gives an overall data taking efficiency of less than 50%. For this upcoming run, it is CDF's goal to run at least 80% efficient. This would mean a factor of of about 8 increase of data to written to tape.

Second, there is a upgrade to the present central muon detector system that will extend central muon coverage out to an η of ± 1.0 but will cover only about 70% in ϕ. This will increase the muon fiducial region by approximately 45%.

These two improvements for the next collider run will increase the present dimuon

data set by a factor of about 12.

6.3 Conclusion

The differential cross section $d^2\sigma/dMdY|_{Y=0}$, along with $M^3d^2\sigma/dMdY|_{Y=0}$, are calculated for the dimuon invariant mass range from 11 to 40 GeV/c^2 and 70 to 110 GeV/c^2. Comparison is made to a next-to-leading order theoretical prediction and to previous experimental results. The cross section $\sigma(Z^\circ \rightarrow \mu^+\mu^-)$ agrees with the CDF measured cross section $\sigma(Z^\circ \rightarrow e + e-)$ within errors.

The measured values of $M^3d^2\sigma/dMdY|_{Y=0}$, plotted in figure 6.1, appear systematically larger than the predicted values using the latest parton distribution functions (PDF's). This would seem to indicate that there are more quark-antiquark pairs at small values of $sqrt\tau$ than are predicted by present PDF's. The systematic discrepancy may be due to lack of understanding of the gluon distribution at small x, which is directly related to number of avaliable sea quarks at small x. The results here seem to indicate that the gluon distribution at small x is much softer, i.e. many more gluons at small x, than is the predicted. Another possibility is that high order effects beyond next-to-leading order may have a large impact on the theoretically predict cross section. At present, there are no calculations of the Drell-Yan cross section beyond next-to-leading order but work is underway to provide them.

One of the goals of this analysis is to try and determine which, if any, of the present PDF's are favored by the measurement of $M^3d^2\sigma/dMdY|_{Y=0}$. Figure 6.2 shows $M^3d^2\sigma/dMdY|_{Y=0}$ compared to the largest and smallest predicted values from figure 6.1. This figure indicates that the PDF HMRSB generates the lowest predicted cross section while PDF MT-B1 generates the highest. It is interesting to note that these two recent PDF differ by as much as a factor of 4 at small invariant mass. From this figure, it appears the the PDF MT-B1 is the most favored of all of the presently accepted PDF's, but because it is unclear if the systematic offset of the data is due to parameterization

of PDF functions or higher-order effects, it is difficult to favor any of the present PDF's. It is hoped that future experimental measurements of the Drell-Yan cross section at CDF and improvements in theoretical predictions will allow one to determine the best parameterization of PDF's at small values of x.

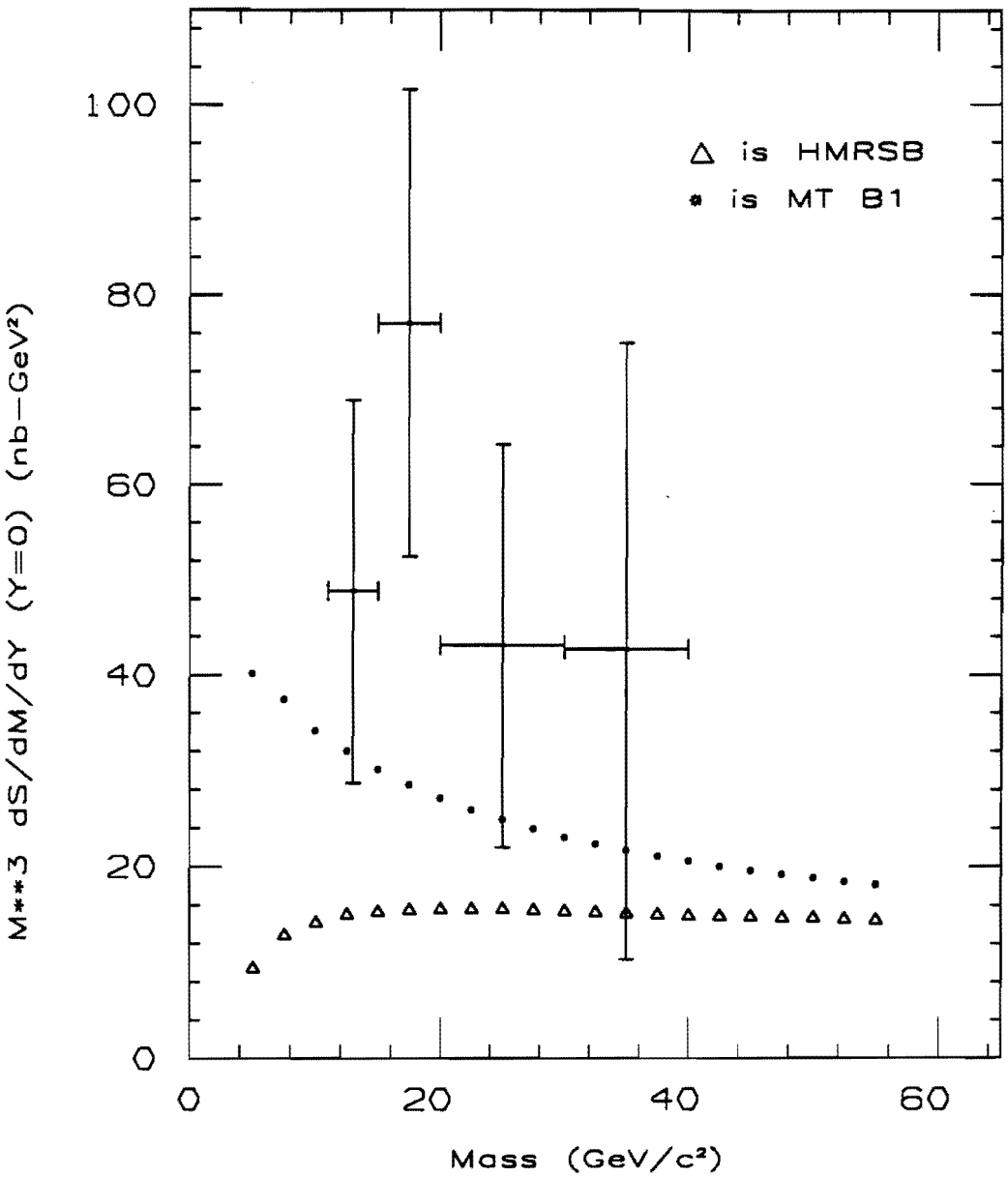

Figure 6.2: Calculated values of $M^3 d^2\sigma/dMdY|_{Y=0}$ compared to largest and smallest next-to-leading order predicted values.

Appendix A

J/ψ's and Υ's: Dimuons in the CDF Environment

During the Fermilab collider run of 1988-89, CDF recorded large a number of dimuon events from J/ψ's and Υ's. These dimuon events appear as large resonances in the dimuon invariant mass spectrum. Since the dimuon signal from these particles is much larger than the background, these dimuons provide a source of real muons measured by the CDF detector. This appendix will show general properties of these muons in the CDF environment.

Figures A.1 and A.2 show the dimuon invariant mass of the J/ψ and Υ into CMUO-CMUO dimuons where the only selection requirement is that the event have a Level 2 DIMUON_CENTRAL_3 trigger. The figures show the opposite-signed dimuon invariant mass spectrum versus the same-signed dimuon invariant mass spectrum. The J/ψ 1S and Υ 1S and 2S states are clearly visible over the same-signed background. One can now make mass cuts around the mass peaks and have a sample of real muons in the CDF environment.

The following plots are for events in the invariant mass windows around the J/ψ 1S state and around the Υ 1S state. Only the opposite-signed events are plotted. Figures A.3, A.4, A.5, and A.6 show the parent object p_T spectrum, the muon p_T spectrum, the

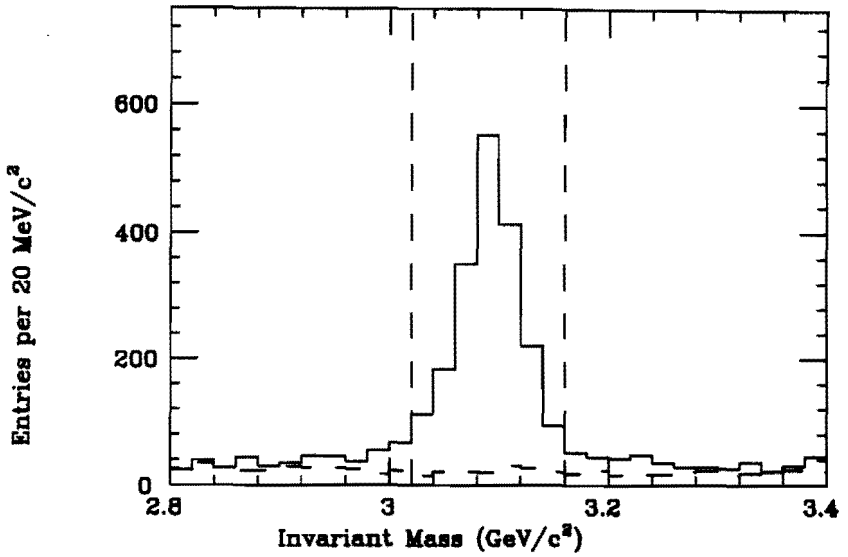

Figure A.1: Dimuon invariant mass of CMUO-CMUO events at the J/ψ mass. The solid line represent opposite-signed events while the dashed line represent same-signed events.

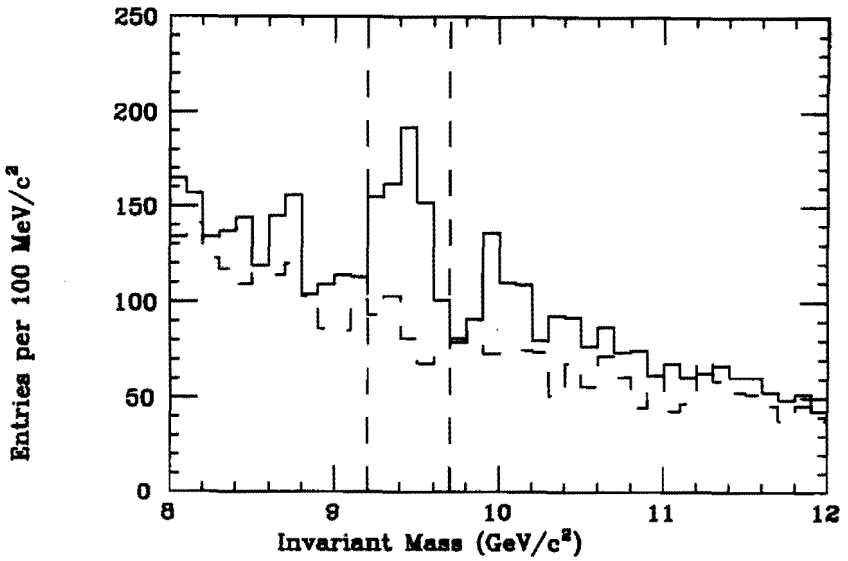

Figure A.2: Dimuon invariant mass of CMUO-CMUO events at the Υ mass. The solid line represent opposite-signed events while the dashed line represent same-signed events.

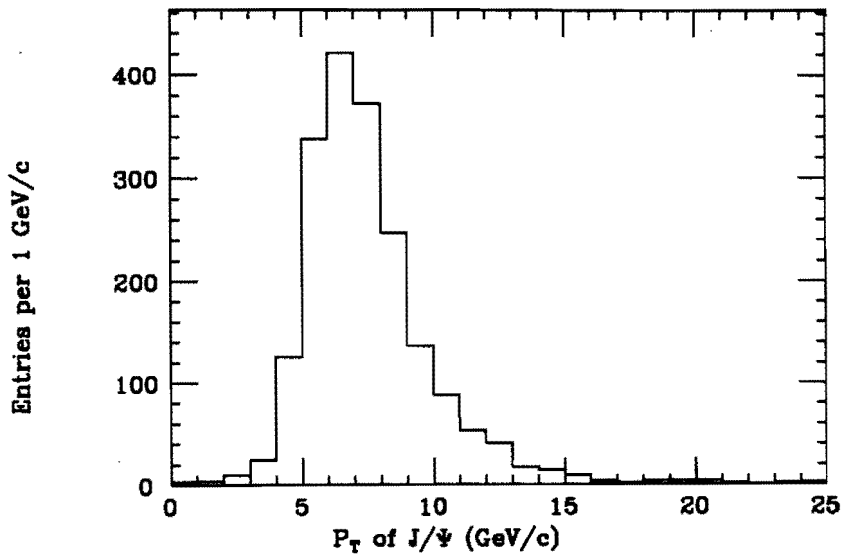

Figure A.3: J/ψ parent p_T spectrum.

three dimensional opening angle between the muons, and the maximum track isolation of both muons for J/ψ 1S state events. Figures A.7, A.8, A.9, and A.10 show the same information for the Υ 1S state events.

Because of the inefficiency of the Level 2 DIMUON_CENTRAL_3 trigger at low muon p_T (see figure 2.11), only high p_T J/ψ events pass the trigger requirement. The decay muons from Υ events at rest have enough p_T to pass the trigger requirements. This is the reason for the lack of low p_T J/ψ events in figure A.3.

Figure A.11 shows the distribution of muons from J/ψ events versus CDF ϕ in units of 15° equivalent to one central wedge per ϕ bin. The flatness of this distribution shows that there is no detector inefficiency as a function of ϕ.

As one can see from figures A.6 and A.10, J/ψ and Υ events are not well isolated. To use muons from J/ψ and Υ events to study various Drell-Yan analysis cuts, a tight isolation cut is imposed. This makes these muons appear more like muons from Drell-Yan events. A maximum track isolation cut of 1.5 GeV/c is imposed on each leg of the J/ψ and Υ dimuons. One can now use these muons to find the tower efficiency cuts of chapter 3. Figures A.12, A.13, and A.14 show the muon tower electromagnetic

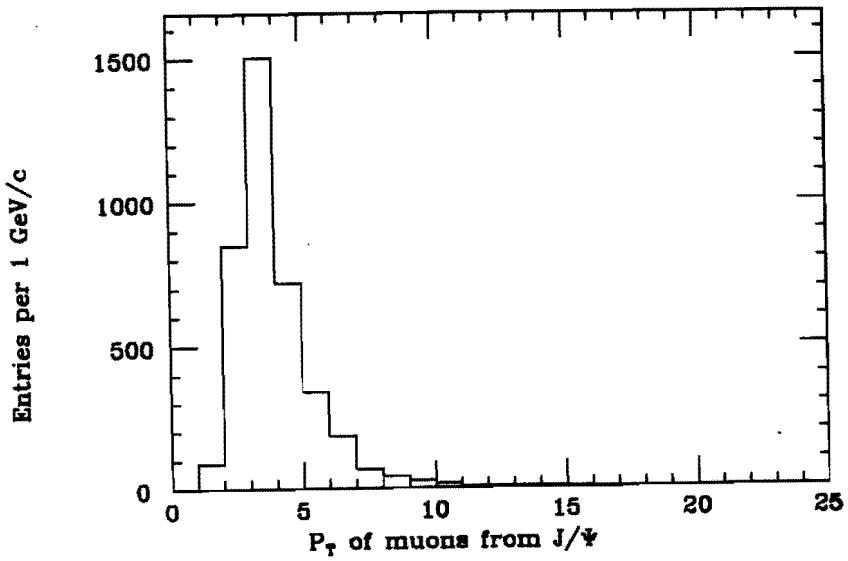

Figure A.4: J/ψ muon p_T spectrum.

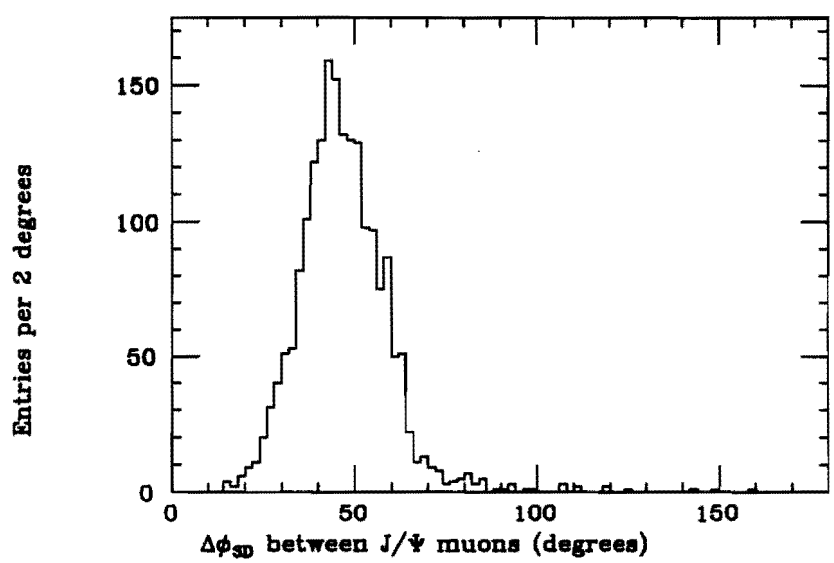

Figure A.5: Three dimensional opening angle between muons from J/ψ.

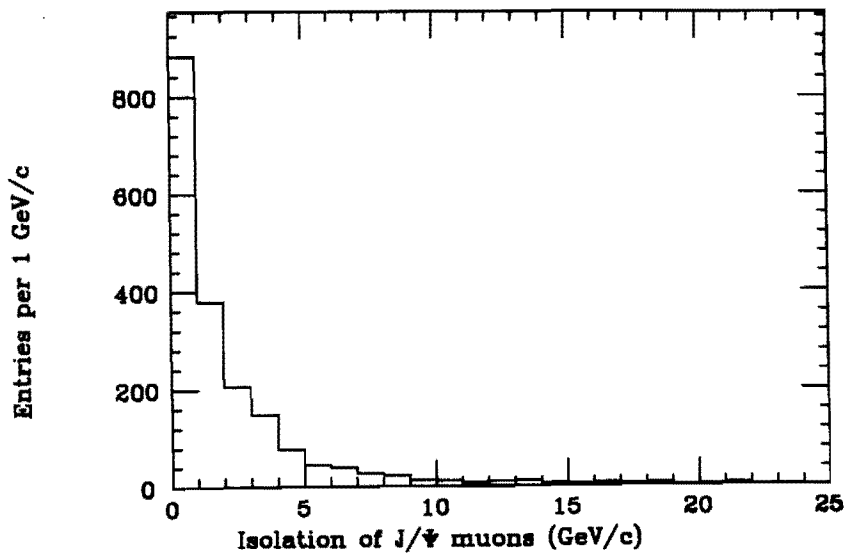

Figure A.6: Maximum track isolation of J/ψ muons.

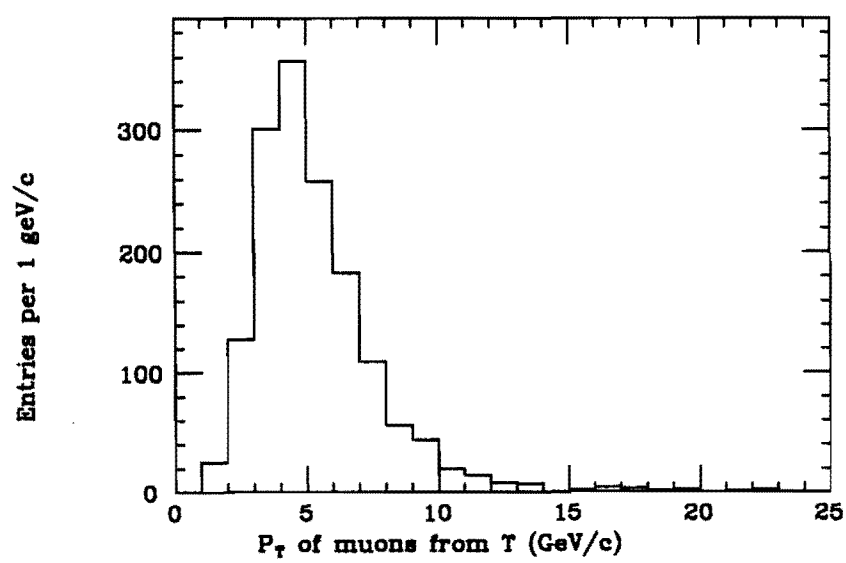

Figure A.7: Υ parent p_T spectrum.

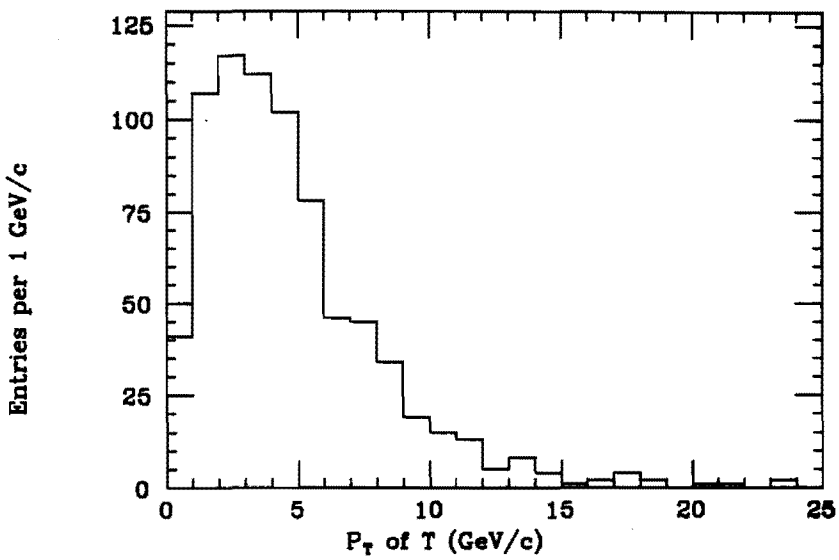

Figure A.8: Υ muon p_T spectrum.

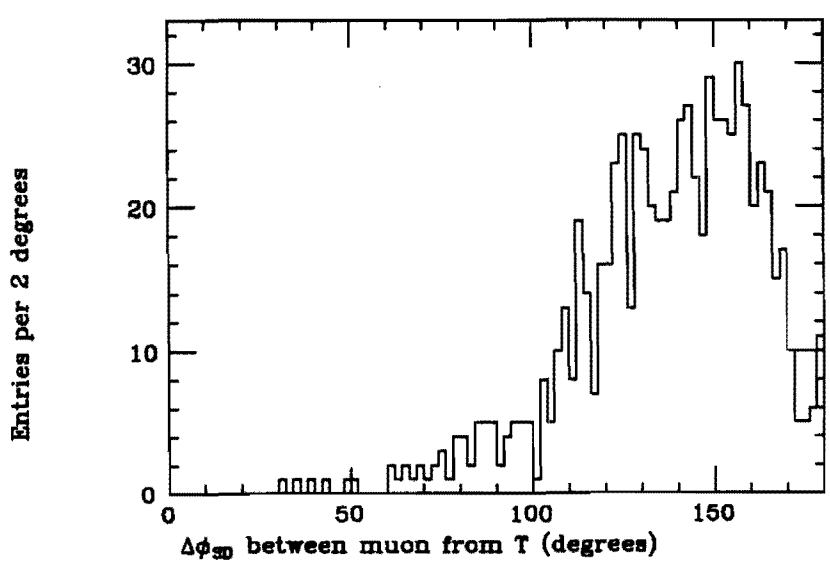

Figure A.9: Three dimensional opening angle between muons from Υ.

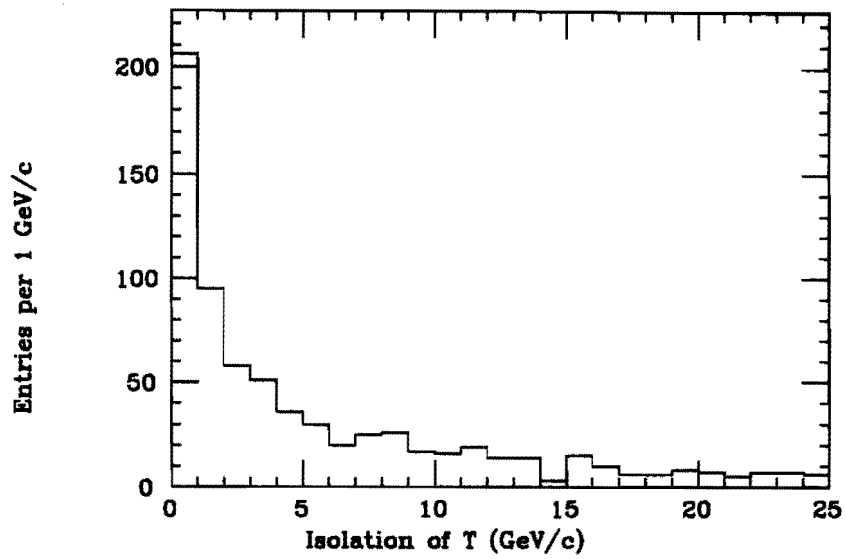

Figure A.10: Maximum track isolation of Υ muons.

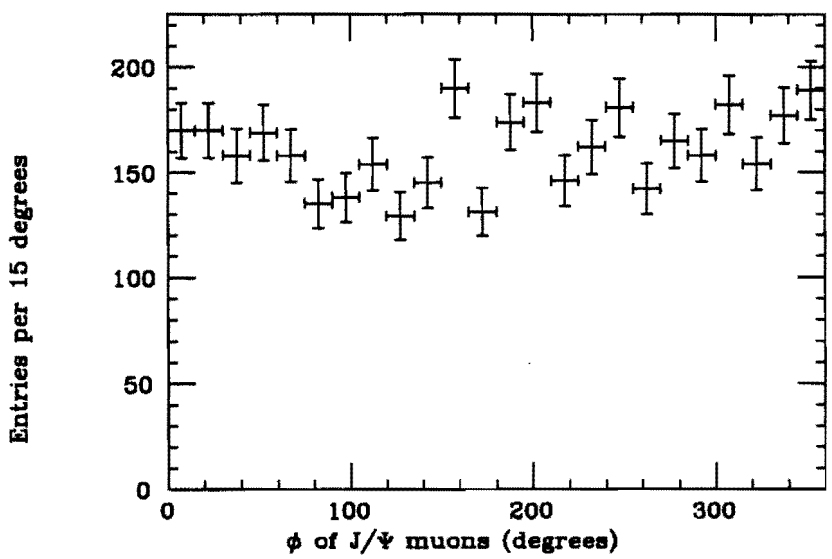

Figure A.11: Distribution of muons from J/ψ and Υ events versus CDF ϕ. The bins are in units of 15° equivalent to one central wedge per ϕ bin.

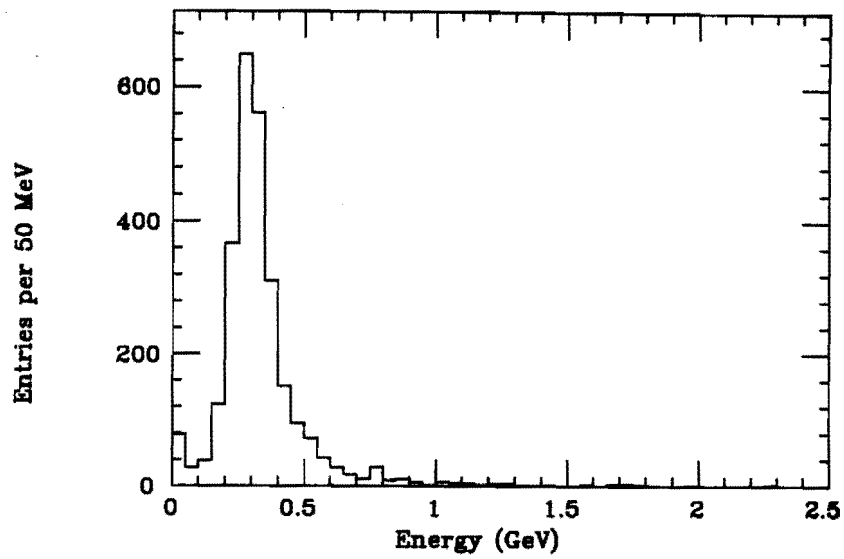

Figure A.12: Electromagnetic calorimetry tower energy for isolated J/ψ muons.

calorimetry energy, the muon tower hadronic calorimetry energy, and the ΔX matching for these isolated J/ψ muons. Figure A.15 shows the ΔX matching times the track p_T for isolated J/ψ muons. A gaussian fit to the plot shows that the average muon multiple scattering is 15 cm divided by muon p_T. This is indicated in equation 3.3. Figures A.16 and A.17 show the maximum impact parameter ($MAX|D0|$) for these isolated J/ψ and Υ events. These figures give the efficiency of the $MAX|D0|$ cut used to remove cosmic rays from the dimuon sample, defined in chapter 5.

The isolated muons from J/ψ events can also be used to define the good fiducial regions of the central muon (CMU) chambers. Figures A.18 show the distribution of CMU track stubs, for J/ψ muons, versus ϕ for all central wedges folded into one wedge. The wedge ϕ coordinates are in degrees. The dashed lines in these figures define the good fiducial region of the CMU chambers in the ϕ direction. Figures A.19 show the distribution of CMU track stubs versus CMU detector η, again where all central wedges are folded into one wedge. The dashed lines in these figures define the good fiducial region of the CMU chambers in the η direction.

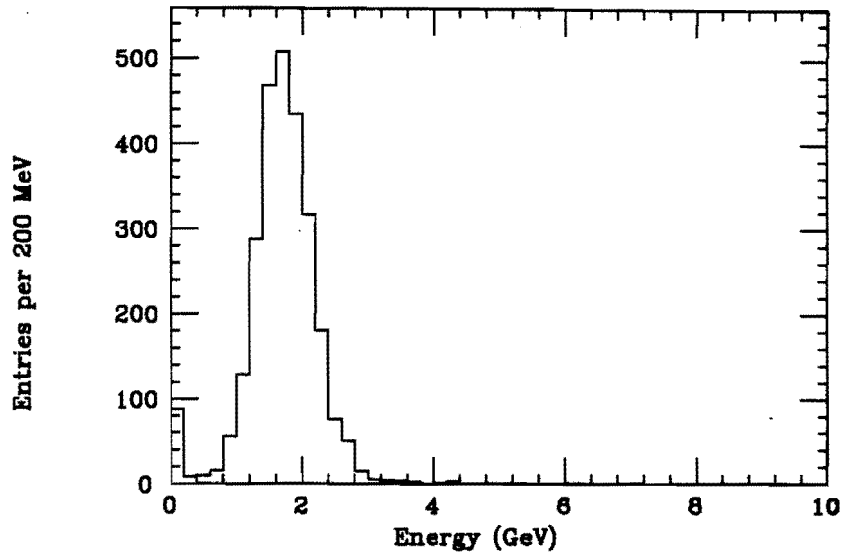

Figure A.13: Hadronic calorimetry tower energy for isolated J/ψ muons.

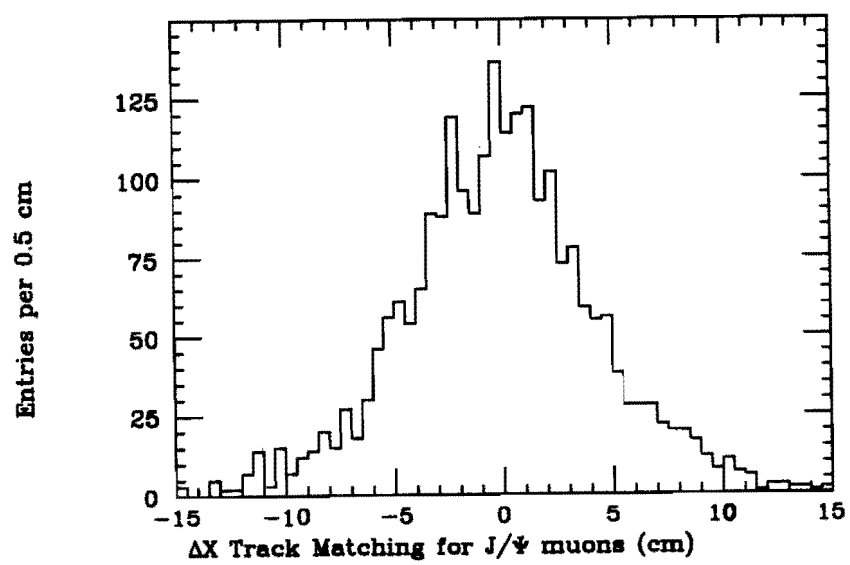

Figure A.14: ΔX track matching for isolated J/ψ muons.

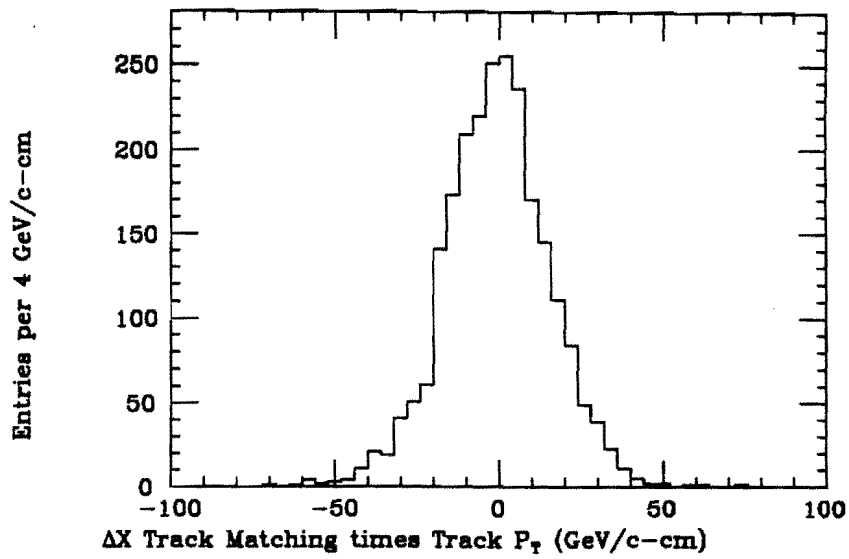

Figure A.15: ΔX track matching times track p_T for isolated J/ψ muons.

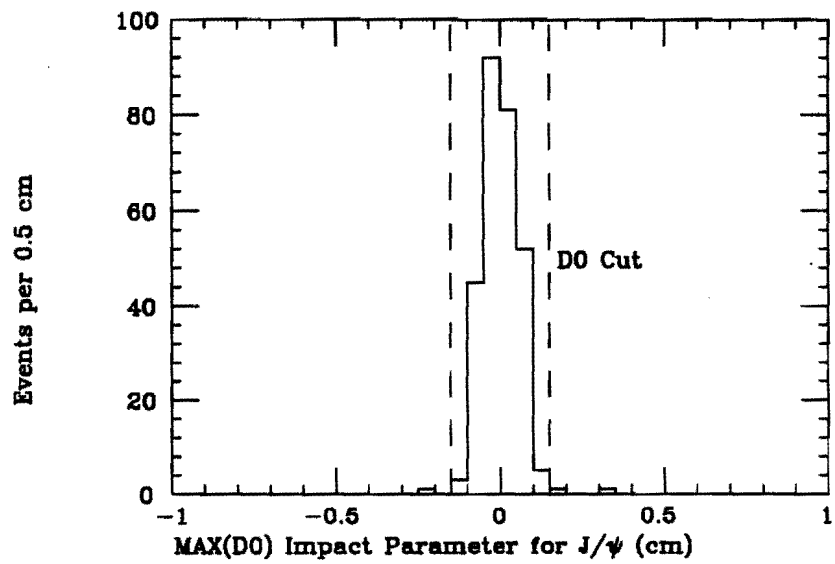

Figure A.16: Maximum track impact parameter ($MAX|D0|$) for isolated J/ψ muons.

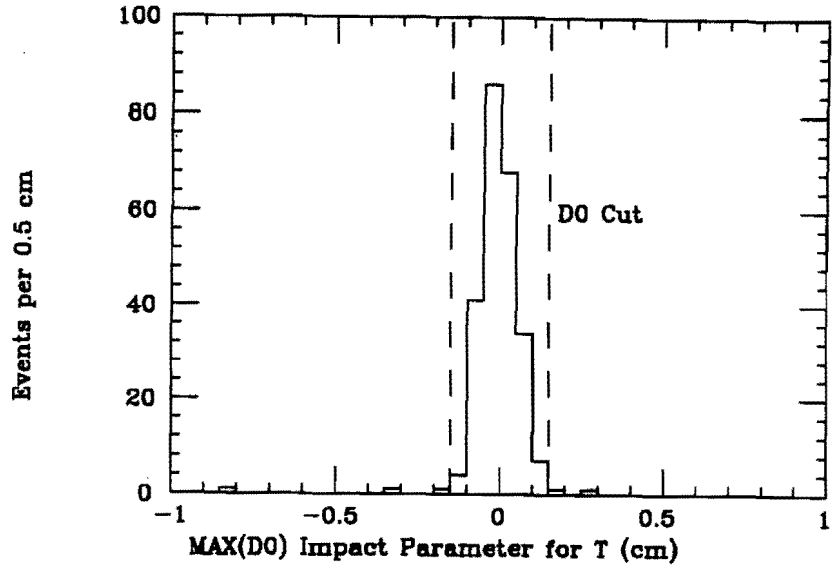

Figure A.17: Maximum track impact parameter ($MAX|D0|$) for isolated Υ muons.

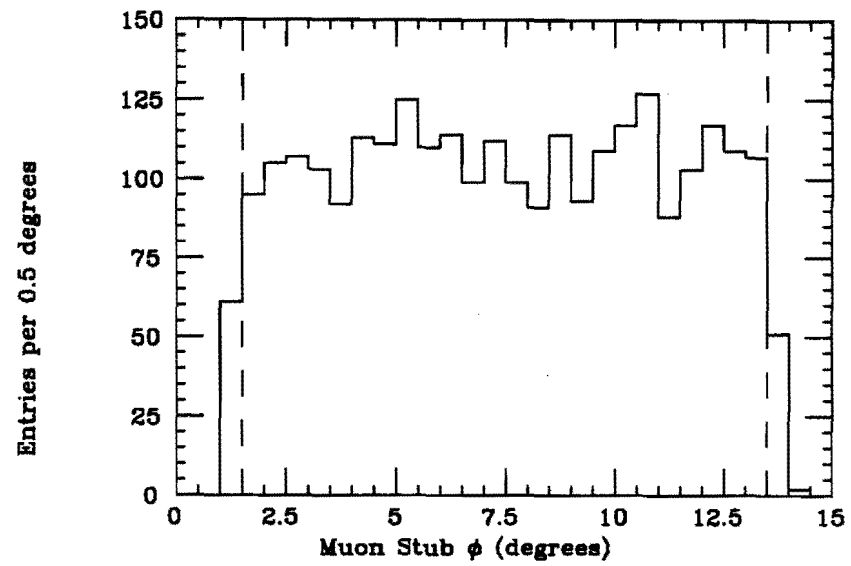

Figure A.18: CMU track stub ϕ position for all isolated J/ψ muons. Dashed lines indicate good CMU chamber fiducial region.

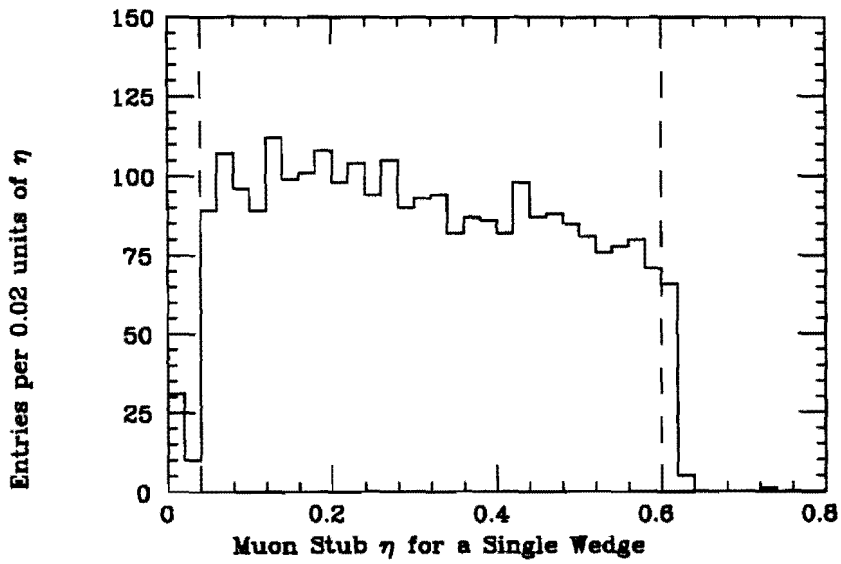

Figure A.19: CMU track stub η position for all isolated J/ψ muons. Dashed lines indicate good CMU chamber fiducial region.

Appendix B

Determination of the Isolation Cut

The main use of the isolation cut is to remove background events while still selecting Drell-Yan events. This appendix describes a study of different types of isolation versus the isolation cut value. The isolation cut, defined by equation 3.1, is generalized to include calorimetry isolation as well as tracking isolation for various cone sizes. The isolation variable for tracking is defined as

$$\text{Isolation}_{\text{tracking}} = MAX_{1,2}(\sum_{R=R'} p_T - p_T^{\mu}) \tag{B.1}$$

while for calorimetry

$$\text{Isolation}_{\text{calorimetry}} = MAX_{1,2}(\sum_{R=R'} E_T - p_T^{\mu}) \tag{B.2}$$

where

$$\begin{aligned}
\sum_{R=R'} p_T &= \text{Sum of the transverse momentum of tracks} \\
&\quad \text{in a cone of radius R}' \text{ around the muon.} \\
\sum_{R=R'} E_T &= \text{Sum of calorimetry transverse energy} \\
&\quad \text{in a cone of radius R}' \text{ around the muon.} \\
p_T^{\mu} &= \text{Transverse momentum of the muon.} \\
MAX_{1,2} &= \text{Take the larger of values of the dimuons.}
\end{aligned} \tag{B.3}$$

In determining the type of isolation used and the value of the isolation cut, the following three guidelines are studied.

1. Maximize the efficiency of the isolation cut.
2. Maximize the ratio of opposite-signed (OS) dimuon events to same-signed (SS) dimuon events, as a function of isolation type and isolation cut value.
3. Minimize the fraction of QCD background passing the isolation cut.

Guideline 1 is studied by looking at the efficiency of different types of isolation versus the isolation cut for dimuon Z° candidates. There are 22 Z° candidates that pass all of the dimuon selection cuts in chapter 3 except the isolation cut. Table B.1 shows the number of Z° passing the isolation cut and the efficiency of the cut.

Guideline 2 is studied by observing the number of opposite-signed and same-signed dimuon events selected for different types of isolation versus the isolation cut value. The dimuons pass all of the selection requirements of chapter 3, except the isolation cut. The invariant mass range is restricted to be between 11 and 40 GeV/c^2. Table B.2 shows the number of opposite-signed and same-signed events for different types of isolation versus cut value.

Guideline 3 is studied by using electron-muon ($e-\mu$) data from real and monte carlo $B-\bar{B}$ events. events and from monte carlo events. Table B.3 shows the fraction (f) of $e-\mu$, $e-e$, and $\mu-\mu$ events from $B-\bar{B}$ decays for an isolation cut value of 1.0 GeV and 1.5 GeV.

Using these three guidelines, the choice of the variable isolation is made to be

$$\text{Isolation} = MAX_{1,2}(\sum_{R=R'} p_T - p_T^{\mu}) < 1.0\ GeV/c. \tag{B.4}$$

which is used in chapter 3. This has the main advantage of having a low fraction of background $B-\bar{B}$ events while still having a large ratio of opposite-signed events to same-signed events. It is also the same definition used by the Drell-Yan dielectron analysis. This last point makes it easier to combine the dielectron and dimuon Drell-Yan differential cross sections.

Cut Description	Cut Value (GeV)				
	<1.0	<1.5	<2.0	<2.5	<3.0
$\sum_{R=0.4} E_T$ (calorimetry)	# Z°=20 ϵ=0.91	# Z°=21 ϵ=0.91	# Z°=21 ϵ=0.95	# Z°=21 ϵ=0.95	# Z°=21 ϵ=0.95
$\sum_{R=0.7} E_T$ (calorimetry)	# Z°=9 ϵ=0.41	# Z°=13 ϵ=0.59	# Z°=18 ϵ=0.82	# Z°=19 ϵ=0.86	# Z°=19 ϵ=0.86
$\sum_{R=0.4} p_T$ (tracking)	# Z°=18 ϵ=0.82	# Z°=22 ϵ=1.0	# Z°=22 ϵ=1.0	# Z°=22 ϵ=1.0	# Z°=22 ϵ=1.0
$\sum_{R=0.5} p_T$ (tracking)	# Z°=15 ϵ=0.68	# Z°=19 ϵ=0.86	# Z°=20 ϵ=0.91	# Z°=21 ϵ=0.95	# Z°=22 ϵ=1.0
$\sum_{R=0.6} p_T$ (tracking)	# Z°=13 ϵ=0.59	# Z°=16 ϵ=0.73	# Z°=20 ϵ=0.91	# Z°=21 ϵ=0.95	# Z°=22 ϵ=1.0
$\sum_{R=0.7} p_T$ (tracking)	# Z°=9 ϵ=0.41	# Z°=14 ϵ=0.64	# Z°=18 ϵ=0.82	# Z°=18 ϵ=0.82	# Z°=20 ϵ=0.91
$\sum_{R=1.0} p_T$ (tracking)	# Z°=2 ϵ=0.10	# Z°=3 ϵ=0.14	# Z°=9 ϵ=0.41	# Z°=11 ϵ=0.50	# Z°=14 ϵ=0.64

Table B.1: Number of Z° dimuon candidates and efficiency (ϵ) of isolation cut for various types of isolation cuts and different cut values. All selection cuts in have been made and there are 22 possible dimuon Z° candidates.

Cut Description	Cut Value (GeV)				
	<1.0	<1.5	<2.0	<2.5	<3.0
$\sum E_T$ R=0.4 (calorimetry)	# OS=59 # SS=17 OS/SS=3.5	# OS= 84 # SS=28 OS/SS=3.0	# OS=99 # SS=40 OS/SS=2.5	# OS=125 # SS=56 OS/SS=2.2	# OS=144 # SS=73 OS/SS=2.0
$\sum E_T$ R=0.7 (calorimetry)	# OS=20 # SS=1 OS/SS=20.0	# OS= 33 # SS=4 OS/SS=8.3	# OS=46 # SS=4 OS/SS=11.5	# OS=54 # SS=11 OS/SS=4.9	# OS=61 # SS=15 OS/SS=4.1
$\sum p_T$ R=0.4 (tracking)	# OS=88 # SS=28 OS/SS=3.1	# OS= 105 # SS= 46 OS/SS=2.3	# OS=121 # SS=56 OS/SS=2.2	# OS=144 # SS=69 OS/SS=2.1	# OS=161 # SS=94 OS/SS=1.7
$\sum p_T$ R=0.5 (tracking)	# OS=65 # SS=13 OS/SS=5.0	# OS= 81 # SS=24 OS/SS=3.4	# OS=94 # SS=38 OS/SS=2.5	# OS=112 # SS=45 OS/SS=2.5	# OS=134 # SS=59 OS/SS=2.3
$\sum p_T$ R=0.6 (tracking)	# OS=47 # SS=5 OS/SS=9.4	# OS= 61 # SS=14 OS/SS=4.4	# OS=75 # SS=27 OS/SS=2.8	# OS=95 # SS=33 OS/SS=2.9	# OS=108 # SS=48 OS/SS=2.3
$\sum p_T$ R=0.7 (tracking)	# OS=35 # SS=1 OS/SS=35.0	# OS= 50 # SS=5 OS/SS=10.0	# OS=60 # SS=17 OS/SS=3.5	# OS=75 # SS=25 OS/SS=3.0	# OS=91 # SS=35 OS/SS=2.6
$\sum p_T$ R=1.0 (tracking)	# OS=20 # SS=0 OS/SS=∞	# OS= 27 # SS= 1 OS/SS=27.0	# OS=35 # SS=2 OS/SS=17.5	# OS=50 # SS=5 OS/SS=10.0	# OS=56 # SS=10 OS/SS=5.6

Table B.2: Number of opposite-signed (OS) and same-signed (SS) dimuons present in dimuon sample for various types of isolation cuts and different cut values. All selection cuts in chapter 3 have been made.

Sample	f, Isolation<1.0	f, Isolation<1.5
$e-\mu$ data	0.115±0.034	0.218±0.044
$e-\mu$ monte carlo	0.100±0.034	0.225±0.042
$e-e$ monte carlo	0.088±0.038	0.175±0.050
$\mu-\mu$ monte carlo	0.079±0.044	0.184±0.063

Table B.3: Fraction (f) of $B-\bar{B}$ events passing dimuon selection cuts.

Bibliography

[1] H. Yukawa,*Proc. Phys. Math. Soc. Japan* **17**, 48 (1935).

[2] J. E. Augustin, *et al*, *Phys. Rev. Lett.* **33**, 1406 (1974).

[3] J. J. Aubert, *et al*, *Phys. Rev. Lett.* **33**, 1404 (1974).

[4] G. Kane, *Modern Elementary Particle Physics*, 9 (1987).

[5] G. Kane, *Modern Elementary Particle Physics*, 261 (1987).

[6] R. P. Feynman, *Phys. Rev. Lett.* **23**, 1415 (1969).

[7] C. Quigg, *Gauge Theories of the Strong, Weak, and Electromagnetic Interactions*, 201 (1983).

[8] I. Hinchliffe, *LBL-25820* (1988).

[9] G. Altarelli and. G. Parisi, *Nucl. Phys.* **B126**, 298 (1977).

[10] W. Tung, *Proceedings of the Workshop on Hadron structure Functions and Parton Distributions*, 18 (1990).

[11] M. Glueck *et al*, *Z. Phys.* **C13**, 119 (1982); D. Duke and J. Owens, *Phys. Rev.* **D30**, 49 (1984).

[12] E. Eichten *et al*, *Rev. Mod. Phys.* **56**, 579 (1984) and Erratum **58**, 1065 (1986).

[13] A. D. Martin, R. G. Roberts, and W. J. Stirling, *Phys. Rev.* **D37**, 1161 (1988), *Mod. Phys. Lett.* **A4**, 1135 (1989) .

[14] M. Diemoz *et al*, *Z. Phys.* **C39**, 21 (1988).

[15] J. G. Morfin and Wu-Ki Tung, Preprint Fermilab-Pub-90/24, IIT-90-11.

[16] H. Plothow-Besch, *PDFLIB: Structure Functions and α_s Calculation User's Manual*, CDF Note 1573.

[17] S. Drell and T. M. Yan, *Phys. Rev. Lett.* **25**, 316 (1970).

[18] J. H. Christenson, *et al*, *Phys. Rev. Lett.* **25**, 1523 (1970).

[19] I. R. Kenyon, *Rep. Prog. Phys.* **45**, 1261 (1982).

[20] C. Grosso-Pilcher and M. J. Shochet, *Ann. Rev. Nucl. Part. Sci.* **36**, 1 (1986).

[21] J. P. Rutherfoord, *1985 International Symposium on Lepton and Photon Interactions at High Energies*, 661 (1985).

[22] C. Albajar, *et al*, *Phys. Lett.* **186B**, 237 (1987).

[23] A. S. Ito *et al*, *Phys. Rev.* **D23**, 604 (1981).

[24] V. D. Barger and R. J. N. Phillips, *Collider Physics*, 233 (1987).

[25] V. D. Barger and R. J. N. Phillips, *Collider Physics*, 221 (1987).

[26] J. Badier *et al*, *Phys. Lett.* **96B**, 422 (1980).

[27] E. Anassontzis *et al*, *Phys. Rev. Lett.* **54**, 2572 (1985).

[28] S. R. Smith *et al*, *Phys. Rev. Lett.* **46**, 1607 (1981).

[29] J. Badier *et al*, *Z. Phys.* **C26**, 489 (1985).

[30] D. Antreasyan *et al*, *Phys. Rev. Lett.* **48**, 302 (1982).

[31] C. Kourkoumelis *et al*, *Phys. Lett.* **91B**, 475 (1980).

[32] M. Corden *et al*, *Phys. Lett.* **96B**, 417 (1980).

[33] J. Badier *et al*, *Z. Phys.* **C18**, 281 (1983).

[34] B. Betev *et al*, *Z. Phys.* **C28**, 15 (1985).

[35] H. B. Greenlee *et al*, *Phys. Rev. Lett.* **55**, 1555 (1985).

[36] K. M. Ankoviak, *8th Topical Workshop on Proton-Antiproton Collider Physics*, 537 (1989).

[37] *Elementary Stochastic Cooling*, Fermilab-TM-1227, Dec 1983.

[38] F. Abe *et al*, *Nuclear Instruments and Methods in Physics Research* **A271**, 387 (1988).

[39] G. Drake *et al*, *Nuclear Instruments and Methods in Physics Research* **A269**, 68 (1988).

[40] E. Barsotti *et al*, *Nuclear Instruments and Methods in Physics Research* **A269**, 82 (1988).

[41] F. Dejongh, private communication.

[42] G. W. Foster *et al*, *Nuclear Instruments and Methods in Physics Research* **A269**, 93 (1988).

[43] R. Hughes, private communication.

[44] D. Baden *et al*, *The V5.1 CDF Production Package*, CDF Note 955.

[45] T. Liss, *GMUFLT: The Muon Filter In Production*, CDF Note 1080.

[46] R. Swartz, *The Fiducial Volume of the Central Muon Chambers*, CDF Note 1259.

[47] F. Abe *et al*, *Phys. Rev. Lett.* **61**, 1819 (1988).

[48] A. Gauthier, *Reconstruction Efficiency of Dimuon Triggers*, CDF Note 1443.

[49] ISAJET monte carlo by Frank Paige.

[50] E. Kearns, private communication.

[51] J. Freeman, *CDF Detector Simulation.* Fermilab document FERMILAB-Conf-87/230.

[52] L. Song, G. P. Yeh, R. Hollebeek, and J, Yoh, *Measurement of $B^0\bar{B}^0$ Mixing Using Electron-Muon Events*, CDF Note 1355.

[53] K. Bloom, M. Contreras, C. Grosso-Pilcher, and H. Frisch, *Low Mass Drell-Yan in the Electron Channel*, CDF Note 1622.

[54] F. Abe *et al*, *Phys. Rev* **44D**, 29 (1991).

[55] J. Stirling, private communication.

Vita

Victor Emanuel Scarpine was born in the fall of 1957 in the steel town of Youngstown, Ohio. He graduated from Austintown Fitch High School in 1975 after spending three years trying to break par with the school golf team. He attended Youngstown State University in the fall of 1975 and couldn't decide whether to major in physics, engineering, or golf. Since he couldn't putt to save his life and wanted a job after graduation, he chose electrical engineering and four years later graduated with a Bachelor of Engineering degree. He then worked four years with the Goodyear Aerospace Corporation trying to tame that putter while also spending part of his time developing computer systems for the U.S. Navy. In the fall of 1983 he decided to try putting on the flattest surface he could find, so he entered graduate school at the University of Illinois in the electrical engineering department and played golf in the corn fields. Over the winter of 1985 he determined that he needed a more fundamental understanding of the theory of putting and switched to the physics department at the beginning of the spring semester of 1986. He did research in experimental particle physics figuring those darn quarks were at the heart of his putting woes. Finally in the spring of 1992 he received his Ph.D. and still couldn't putt. So now it's off to Fermilab and Texas A&M University to further tackle the art of putting. After all, tomorrow *is* another day...